Ministry of Higher Education and Scientific Research

Monastir University

THESIS

Presented to fulfill the doctor degree requirements from the

National Engineering School of Monastir

In ENERGY ENGINEERING

By Asma Naouar

<div style="border:1px solid black">

Performance study of a Solid Oxide Fuel Cell SOFC

</div>

Publicly defended on September 26, 2024

Jury Member

Mr. Abdelmajid Jemni	Professor	ENIM, Monastir	Chair
Mr. Walid Hassen	Associate-Professor	ENIM, Monastir	Reviewer
Mr. Fraj Echouchene	Associate-Professor	ISSAT, Sousse	Reviewer
Mr. Hacen Dhahri	Professor	ENIM, Monastir	Examinator
Mr.Abdallah Mhimid	Professor	ENIM , Monastir	Supervisor

Laboratory for the Study of Thermal and Energy Systems (LESTE) LR99ES31

I wish to express deep gratitude to my supervisor **Dr. Abdallah Mhimid**, Professor at ENIM University of Monastir, Tunisia, for his invaluable supervision and insight throughout the research process and for all the patience and support you gave me since the first day of my thesis completion. His consistent trust during my thesis work is greatly appreciated.

I would like to thank **Dr. Massimo Santarelli**, Professor at Department of Energy (DENERG), Politecnico di Torino, for accepting me as a visitor scholar and researcher in his Laboratory and the useful advice and support, and for the patience and encouragement you provided.

I would like to thank also **Dr. Domenico Ferrero**, Associate professor at Politecnico di Torino, for co-supervising, generously providing guidance and for all the patience and support you gave me. He was always there to lend a helping hand in this thesis.

I would like to thank **Dr. Abdelmajid Jemni**, Professor at ENIM, University of Monastir, who has kindly accepted to be the president of the jury evaluating my thesis work.

I would thank also my committee members **Dr. Walid Hassen** Associate-Professor at ENIM, University of Monastir, and **Dr. Fraj Echouchene** Associate-Professor at ISSAT, University of Sousse, for accepting to review my thesis. Their critical reviews and evaluations of my work resulted in the success of this PhD thesis.

Many thanks are also addressed to **Dr. Hacen Dhahri** Professor at ENIM, University of Monastir, for accepting to examinate this work, for co-supervising, generously providing guidance and for all the patience and support you gave me since the first day of my thesis completion.

Special thanks to my family, words cannot express how grateful I am to my Mother **Hajer,** and my Father **Mustapha,** for unconditional support, prayers for me all the time and encouragement to pursue my interests. This thesis is dedicated to them. No dedication can express the love, esteem, dedication and respect that I have always had for you. Nothing in the world is worth the efforts provided day and night for my education and my well-being. This work is the fruit of your sacrifices that you have made for my education and training.

I am deeply thankful to my sister **Rabeb** and my brothers **Ghanem** and **Ward** for their supports, sacrifices and help throughout my life. You have always been a major source of support when things would get a discouraging.

Table of contents

List of figures

List of tables

NOMENCLATURE

Symbols

C_p	Specific heat capacity [J kg^{-1}K^{-1})]
D_{ij}	Molecular diffusivity [m² s^{-1}]
d_j	Driving force for diffusion [m^{-1}]
$D_{k,ij}$	Knudsen diffusivity of species [m² s^{-1}]
E	Voltage [V]
F	Faraday's constant [C mol^{-1}]
i_0	Exchange current density [A m^{-2}]
i_v	Volumetric current density [A m^{-3}]
j_i	Mass flux [kg m^{-2} s^{-1}]
K	Permeability tensor of the porous medium [m²]
M_i	Molecular mass [kg mol^{-1}]
n	Number of participating electrons
N_i	Molar flux [mol m^{-2} s^{-1}]
P	Pressure [Pa]
Q_h	Source term (heat) [W m^{-2}]
Q_m	Source term (mass) [kg m^{-3} s^{-1}]
R	Universal gas constant [J mol^{-1} K^{-1})]
T	Temperature [K]
u	Velocity [m s^{-1}]
V	Volume fraction
v_i	Stoichiometric coefficient of components i
ΔS_r	Entropy change [J mol^{-1} K^{-1})]
ΔG	Gibbs free energy [J mol^{-1}]

Abbreviation

act	Activation
AFC	Alcaline fuel cell
AFL	Anode active layer

ASL	Anode support layer
CDL	Cathode diffusion layer
CFL	Cathode active layer
CFD	Computational fluid dynamics
DMFC	Direct methanol fuel cell
eff	Effective
IAE	Interface anode-electrolyte
MCFC	Molten carbonate fuel cell
PAFC	Phosphoric acid fuel cell
PEMFC	Proton exchange membrane fuel cell
ref	Reference
TPB	Triple phase boundary
SOFC	Solid oxide fuel cell

Greek symbols

α	Charge transfer coefficient
ε	Porosity
η	Over potential [V]
μ	Dynamic viscosity [kg m^{-1} s^{-1})]
ρ	Density [kg m^{-3}]
σ	Charged-species conductivity [S m^{-1}]
τ	Tortuosity factor
φ	Electric potential [V]
ω_i	Mass fraction

Subscripts

a	Anode
b	Bulk
c	Cathode

e	Electrode
el	Electrolyte
i,j	Specie index
l	Ion transfer material
m	Reaction m
ox	Oxidant
s	Electron transfer material
red	Reducer

General introduction

Researchers have examined the effects of human activities on the environment extensively over the last fifty years, particularly with regard to climate change, which has been a global issue since the first world summit.

Because of worries about climate change, most countries are looking for alternatives to generate energy in a clean, efficient, and environmentally friendly way. But over many years, nevertheless, this has proven to be a significant obstacle for researchers in both academia and business.

In fewer than 30 years, the global consumption of energy has climbed by more than 70%, (accounting for a 120% increase in the consumption of electricity throughout the world) [1,2]. Figure 1.1. displays the global energy consumption from 1970 to 2020 as well as estimations to 2030.
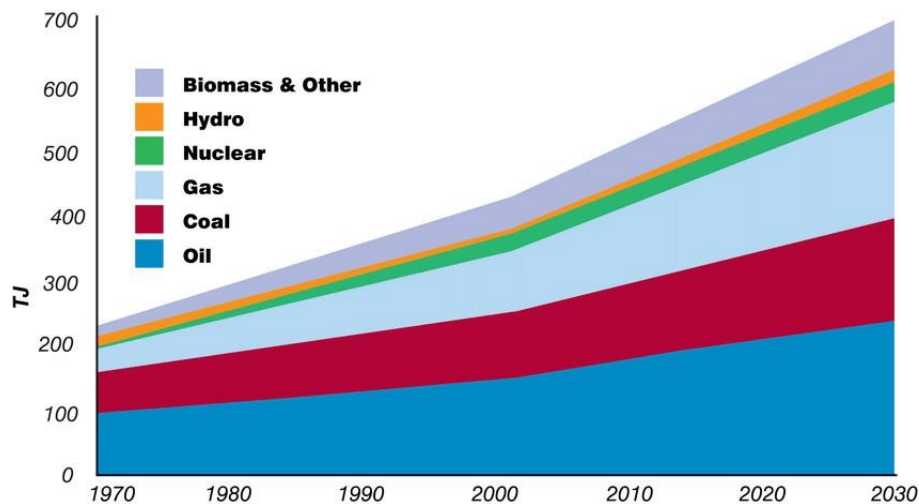
Figure I . World primary energy demand by fuel (in Terajoule) [3]

Globally, the amount and composition of energy demand are influenced by demography. According to the most recent predictions, the global human population is rising by 1.1 % annually, from approximately 6.6 billion in 2007 to 8.2 billion in 2030.

During this period, worldwide primary demand of energy is increasing by 1.5% per year, reaching a total of 40%. Energy mix still heavily depends on fossil fuels like oil, coal, gas, and uranium for nuclear energy, even with efforts to reduce carbon dioxide and other emissions. From an environmental perspective, global energy-related carbon dioxide emissions will continue to rise by a 1.3% annually between 2010 and 2040 [4].

Considering the effects of a temperature increase, a rise over 1.5°C would have harmful impacts on the entire world, thus, among the currently documented phenomena are desertification, ice melting, and the extinction of species.

Because of their unequal distribution, reliance on fossil fuels or uranium also raises the possibility of geopolitical instability and drives up fuel costs.

Interest in alternative sources of energy has evolved as a result of growing public concern about environmental damage, as well as the necessity of clean, efficient, and sustainable energy generation.

Therefore, the European Union established the framework for a new European Energy Policy in 2007 with the following goals [5]:

a) Facing the effects of climate change

b) Reducing the vulnerability of the EU to hydrocarbon imports;

c) fostering economic growth by offering customers safe, reasonably priced energy

By 2020, the goals of new policy are:

a) 20% less emissions of greenhouse gases

b) A 20% rise in the proportion of renewable energy

c) A 20% improvement in the efficiency of energy.

In order to reach these goals, the EU is spearheading the development of energy systems that are cleaner, more efficient, and hydrocarbon-independent; an example of green power source is fuel cell.

A fuel cell is a device that transforms the chemical energy from a fuel into electrical energy, through a chemical reaction with oxygen or another oxidizing agent. There are many types, including Solid Oxide Fuel Cell, Molten Carbonate Fuel Cell, Proton Exchange Membrane Fuel Cell. Since these fuel cells are considered to be almost clean, they are quite promising as energy sources.

Global government and industry funding has been providing substantial support for the development of fuel cell and electrolyzer technology in order to develop hydrogen-powered vehicles and renewable energy storage.

Indeed, fuel cells have been incorporated into many different fields in the twenty-first century, particularly in stationary applications (schools, hospitals, homes, etc.) and transportation (buses, trains, ships, cars and tractors).

The alkaline fuel cells that Bacon introduced in 1958 caught the interest of Pratt and Whitney, a company that deployed them on the Apollo spacecraft because of their dependability.

Concurrently, GE was working on fuel cell technology for McDonnell Aircraft and NASA as part of the GEMINI campaign.

Air Liquide has initiated their Blue Hydrogen program in 2016 "whose objective is to progressively decarbonize its generation of Hydrogen for energy usage".

Although the international financial crisis brought on by the Covid19 epidemic, companies such McPhy have experienced their stock price doubled in a few months in 2020 and have drawn numerous contracts for hydrogen transportation and green hydrogen generation [1].

Over the course of the 1960s, various fuel cell variants have emerged, including solid oxide fuel cells (SOFC), which alter the fuel, component materials, and operating temperature. Since then, advancements have been made while accounting for decreased prices and increased power density [1].

Actually, the SOFC system promises to be a practical and affordable alternative for a sustainable energy source, providing a long-term, efficient, and reliable means of generating power. Since the 1990s, many scientists have investigated and reported the potential of SOFC.

The principle objective of this thesis is to develop a comprehensive multiphysics model for the numerical simulation of a single planar SOFC in steady state, including momentum, species, heat, electron and ion transport as well as electrochemical reactions in order to improve the current performance. The computational model will be able to investigate the operational behavior of a SOFC at high temperature, and ameliorate the comprehending of complex physical phenomena within the cell and the couplings between them, promoting the commercialization of fuel cells.

This thesis is laid out as follows:

Chapter 1 Basics of Fuel Cells and Solid Oxide Fuel Cell History
The first chapter provides a general overview on fuel cells in a first section, involving history, various kinds, benefits, drawbacks and applications of fuel cells. A second section presents background information on the operating principle, components and classifications of SOFCs.

Chapter 2 Model development
The developed mathematical models are discussed with a detailed description of the fundamental principles, gas-phase species, momentum, heat, ion and electron transport and electrochemical reactions for different components of the SOFC

Chapter 3 Numerical study of electrode permeability influence on planar SOFC performance

In this chapter, a three dimensional numerical model has been developed in order to analyse the role of some thermophysical and morphological parameters on the performance of the SOFC cell. This study permits to comprehend the relationship between the performance and microstructure of SOFCs. Concurrently, it furnishes theoretical guidance for an optimum design of the electrode permeability. The effect of the variation of electrode permeability is studied; fuel distribution, ionic and electric current density, pressure and diffusion flux are analyzed and compared.

Chapter 4 Numerical study on performance enhancement of a solid oxide fuel cell using gas flow field with obstacles and metal foam

A 3D computational fluid dynamics model is developed to investigate the impact of using a metal foam as flow distributor with the presence of obstacles in the gas flow channels of SOFC. This chapter analyses how the altered flow field affects the distribution of species along the cell active layers, for cases exploiting the metal foam and obstacles, compared to straight channel structure. It is found that, even if the pressure drops are affected, the reactant gases are more uniformly distributed and penetrated throughout the catalyst area of the cell, the mass transport losses are minimized and, especially, the current density is enhanced for the case of new electrode channel design.

The validity of mathematical model has been demonstrated by comparing the numerical results with experimental data retrieved from literature.

References

[1] Tchakalov, R. Engineering and optimization of electrode/electrolyte interfaces to increase solid oxide fuel cell (SOFC) performances (Doctoral dissertation, Université Paris sciences et lettres), 2021.

 [2] https://yearbook.enerdata.net/

[3] Alghamdi, Y. A., & Almutairi, Z. Photovoltaic Cells Soiling Prevention with Engineered Surface Patterns Phase one: 1st Progress Report.

[4] Birol, F. (2009). World energy outlook 2006. International Energy Agency, 2009.

[5] Nassar, A. A. H., & Abu Saleh, O. (2015). Analysis of Fuel Cells Using COMSOL Multiphysics and Comparison Between Major Types of Fuel Cells SOFC and PEMFC, 2015.

Chapter 1: Basics of Fuel Cells and Solid Oxide Fuel Cell History

1 Introduction

A fuel cell is an electrochemical system, consisting of two electrodes and an electrolyte, that converts the chemical energy of a redox reaction into electrical energy accompanied by the release of heat. It is one of these technologies that has been evolved and aims to be more efficient, reliable, profitable and non-polluting.

Fuel cells belong to the battery family, but they differ from other batteries in that their lifetime does not depend on the amount of chemical reactants stored within the cell, and they operate continuously on a fuel supply.

Different types of fuel cells have been invented, operating at temperatures ranging from a few tens of degrees Celsius to over 1000°C, depending on the electrolyte used. A fuel cell is made up of a stack of cells (electrolyte, anode, cathode) connected via interconnectors (or bipolar plates) [1].

2 Fuel cell

2.1 Fuel cells History

Fuel cells are often referred to as a new technology. However, its invention dates back to the 19th century. In 1802, Sir Humphry Davy discovered the principle of electrochemistry by constructing a carbon cell operating at high temperature with nitric acid as the electrolyte. By carrying out this same experiment, Christian Friedrich Schoenbein discovered, in 1838, that during a power cut a current in the opposite direction to the first one is produced.

The first hydrogen-oxygen cell was built in 1839 by Sir William Grove, who carried out the reverse reaction of water electrolysis using porous platinum electrodes and sulfuric acid as the electrolyte [2,3].
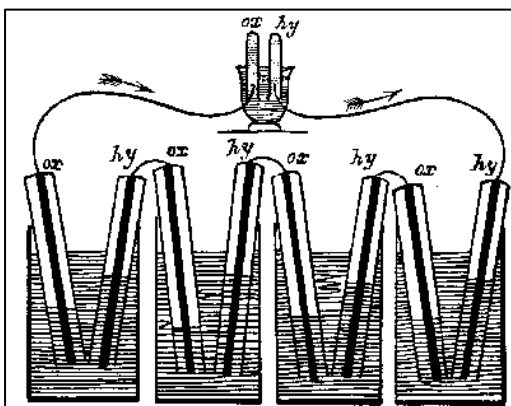
Figure 1. 1. Sir William Grove experience 1839 [4]

Figure 1. 2. Sir William Grove (1811 – 1896) [5]

After some improvements made to this experiment, in 1889, L. Mond and C. Langer made refinements to the fuel cell, notably with the introduction of catalysts (platinum black) or electrolytes that could be contained in porous matrices of plaster or asbestos.

In 1921, E. Baur highlighted the importance of kinetics. He developed a cell operating at high temperature (1000°C), with a carbon anode, a cathode based on iron oxide and alkaline carbonates as electrolytes.

The most important progress was then made by Francis T. Bacon who replaced the acidic electrolyte with an alkaline electrolyte. The advantage of the latter is that it is less corrosive to the electrodes.

Around 1935, he created the first hydrogen-oxygen fuel cell, which led to the manufacture of a first 1 kW electric generator [5].

This achievement highlighted the various advantages of this fuel cell: silent operation, very high efficiency compared to other thermal generators, and the possibility of stationary or traction use. We are therefore looking for a high energy density in a confined atmosphere.

In the 1960s, prototypes of 1 kW methanol and hydrazine fuel cells (N_2H_4) and hydrogen /air alkaline fuel cells (AFC) were produced. In 1970, the Nafion membrane was used to revive acid fuel cells (proton exchange membrane fuel cells (PEMFC)). This type of fuel cell is reliable but limited because it only works with Hydrogen and Oxygen.

One of the key moments in the development of fuel cell research was the first oil crisis of 1973. For the first time, the need for energy independence has emerged. This has accelerated research in the United States, Europe and Japan.

The research carried out during this period will be essentially fundamental and will aim to develop and improve the various components of the cell as well as all the peripherals: compressors, exchangers, storage systems, distribution and production of hydrogen ...

In 1977, a 1 MW stationary installation, has been followed by a 4.5 MW installation in 1983. These units use phosphoric acid hydrogen/air fuel cells (PAFC) operating at nearly 200°C under 8 atmospheres. At the same time, innovative methods of reforming using fossil fuels such as coal or light hydrocarbons are being sought for stationary applications [4].

Later on, the Canadian company Ballard, which had started researching fuel cells, emerged as a key participant in the production of stacks and systems for both stationary and transport applications. Government support for the development of SOFC and PEMFC technologies for residential micro-CHP applications started to increase significantly in Germany, Japan, and the UK.

The Zero Emission Vehicle (ZEV) Mandate was first presented by the California Air Resources Board (CARB) in 1990. Moreover, automakers with significant US sales, including Toyota, General Motors, and the then-DaimlerChrysler, made investments in PEMFC research.

The past several years have seen an enormous rise in fuel cell shipments as more applications have become commercially viable. For example, the quantity of portable fuel cell teaching kits sold to consumers resulted in the fastest growth rate for the product Since 2009. Many important participants received much-needed cash from this legitimate commercial sector, which enabled them to fund research into more extensive stationary and transportation applications [6].

2.2 Fuel cells operating principle (and thermodynamics)

A fuel cell is an electricity generator that directly transforms the chemical energy of a fuel into electrical energy.

The fuel cell operates in the reverse mode of water electrolysis. It comprises two electrodes (anode and cathode) separated by an electrolyte, a substance that permits ions to circulate but prevents the passage of electrons [7].
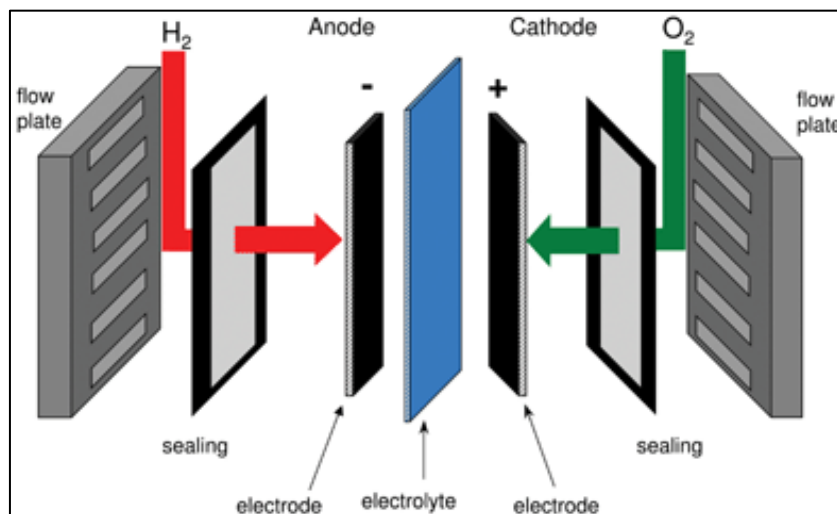
Figure 1. 3. Fuel cell components of a single cell [8]

2.3 Components of the fuel cell core

2.3.1 Electrolyte

The electrolyte (or the membrane) is a key component of the fuel cell system. This needs to guarantee various functions: electrically isolate the two electrodes, ensure ionic conductivity by allowing the transfer of ions from one electrode to the other and properly separate the gases to prohibit direct contact of the fuel and the oxidizing gas [9-11].

2.3.2 Electrodes

The role of the electrode is to insure the evacuation of the water generated by the reactions. Improper removal of this hinders the access of the gas and interrupts the reaction (cathode flooding). It necessitates to function as a reliable conductor of electrons. Its constituents require to be fairly chemically inert in the acidic and corrosive environment of the fuel cell. For this reason, the main element in this layer is typically carbon.

It is the seat of the electrochemical reaction. The most suitable reducer is the hydrogen (H_2), and the oxidant is the atmospheric oxygen (O_2).

At the anode (negative pole), the hydrogen will transform into ions H^+ by releasing electrons according to the reaction:

$$H_2 \rightarrow 2H^+ + 2e^-$$
(1.1)

At the cathode (positive pole), the H^+ ions associate with the O^{2-} ions derived from oxygen in the air to form water according to the reaction:

$$\frac{1}{2}O_2 + 2H^+ + 2e^- \rightarrow H_2O$$
(1.2)

It is the transfer of H^+ ions and electrons towards the cathode that will produce a direct electric current and water from hydrogen and oxygen.

The overall reaction is therefore written:

$$H_2 + \frac{1}{2}O_2 \rightarrow H_2O \quad + \quad \text{electric energy}$$
(1.3)
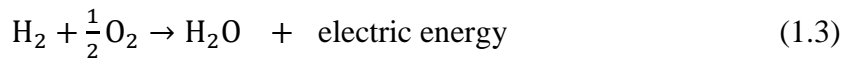
Triple contact zone (gas / electrolyte / electrode) (TPB): It consists of platinum carbon blended with a proton-conducting polymer electrolyte and a hydrophobic (water-repellent) polymer including PTFE. The transfer of reactive gases and ions is ensured by the electrolyte. Carbon assures electronic conduction. Because of its porosity, hydrophobic polymers can be present, reactive gases can be supplied, and inactive gases can be released [12].
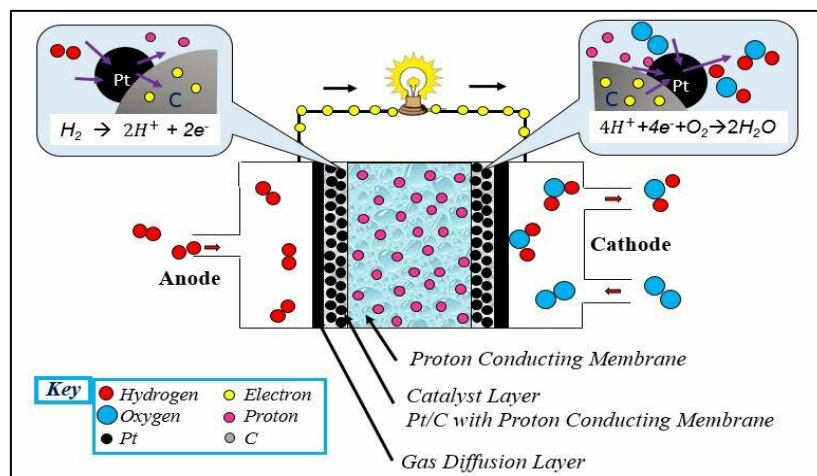
Figure 1. 4. Schematic representation of Triple contact zone [13]

2.3.3 Interconnector (Bipolar plate)

In a fuel cell, the interconnector is a physical boundary separating two elementary cells. It affects their mechanical rigidity and the electrical connection between the external circuit and the two monopolar plates.

Therefore, it performs as an electronic conductor linking the anode which produces electrons and the cathode which consumes electron of the neighboring cell. It carries gas supply channels on the two sides. The first side supplies hydrogen to a cell's anode, and the other side delivers oxygen to the adjacent cell. Distribution should be as even as feasible to avoid the hot-spot phenomenon caused by the exothermic nature of the electrochemical reaction.

Interconnectors bonded to the electrodes enable gases to diffuse towards the electrodes and electrons to be collected (evacuation and wetting of the membrane). They also need to be gas-tight and chemically inert to withstand aggressive environments. These plates are most often made of graphite [14].
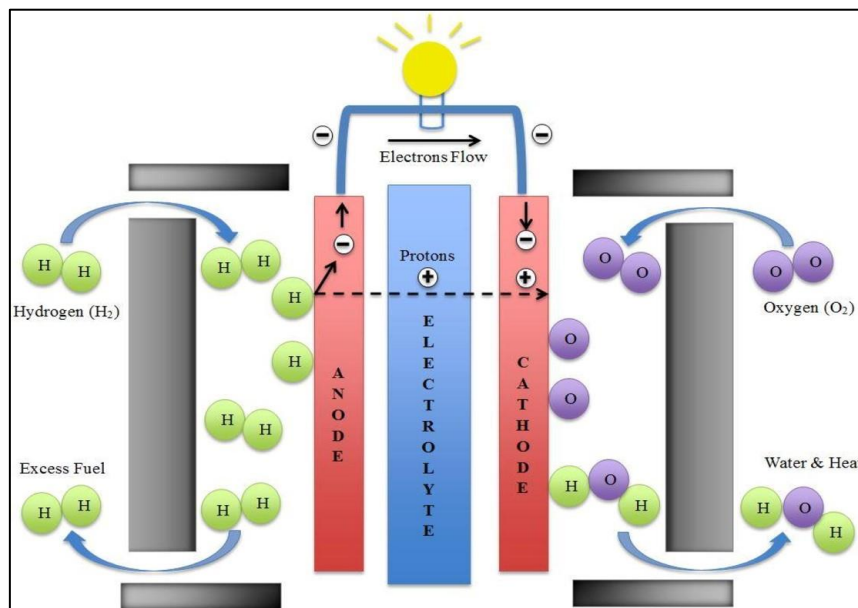
Figure 1. 5. Representation of the electrochemical reaction in fuel cell [15]

2.4 Fuel cell types

Fuel cells are present in a variety of forms, each with special material characteristics and operations. They are appropriate for a variety of applications, and can be classed according to the nature of the electrolyte, fuel required, operating temperature, and conducting ions that move through the electrolyte [16-19].
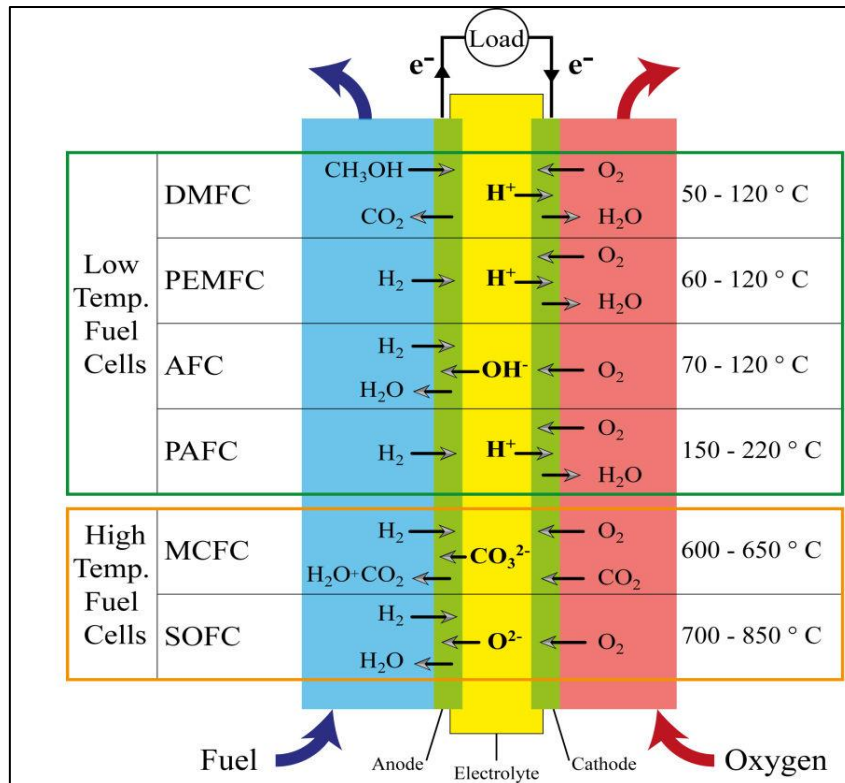
Figure 1. 6. Different types of fuel cell and their operation [20]

The first four fuel cells in the illustration operate at low and medium temperatures, whereas the bottom two cells function at high temperatures. In addition, they vary from one another in a broad scale of other fields, including basic materials, operational settings, and the kind of ion carried throughout the electrolyte.

A brief discussion of common fuel cell types is provided as follows.

2.4.1 Direct methanol fuel cell (DMFC):

DMFC is a kind of fuel cell that utilizes liquid methanol (CH_3OH) as fuel, it is a recent technology that has been under development since the 1990s. Its electrolyte is a strong polymer-based solid acid and its operating temperature is between 50 to 90°C. The catalysts used contain excessive quantities of platinum, the dispersion of catalytic metals (Pt and platinum alloys) within suitable conductive structures and the increase in temperature lead to improved performance. To use it, a mixture of water and methanol is brought to the anode. This mixture reacts to produce hydrogen cations, electrons and carbon dioxide.

$$CH_3OH + H_2O \rightarrow 6H^+ + 6e^- + CO_2 \qquad (1.4)$$
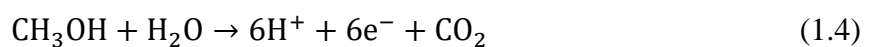
Hydrogen ions move through the membrane, and the electrons flow in an external circuit towards the cathode, the CO2 is released from the cell.

Anode $\qquad$ $CH_3OH + 7H_2O \rightarrow 6H_3O^+ + 6e^- + CO_2$ $\qquad$ (1.5)

Cathode $\qquad$ $O_2 + 4H_3O^+ + 4e^- \rightarrow 6H_2O$ $\qquad$ (1.6)

Reaction Balance $\qquad$ $CH_3OH + \frac{3}{2}O_2 \rightarrow 2H_2O + CO_2$ $\qquad$ (1.7)
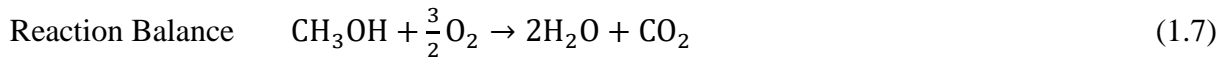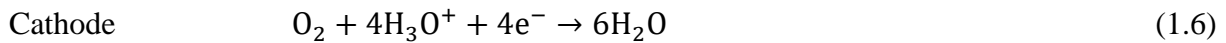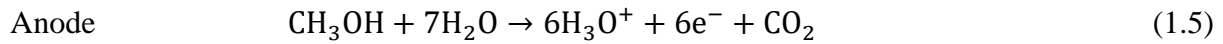
Its standard voltage = 1.21 V.

The effective electrical efficiency of approximately 20 to 25% due to overvoltages at the electrodes and incomplete reactions (formation of formic acid HCOOH or formic aldehyde HCOH). Methanol is very abundant fuel that is in a liquid state at ambient temperature, which facilitates its storage; its reforming is not necessary so it reduces the total volume.

2.4.2 Proton exchange membrane cell (PEMFC)

It is also called a "polymer electrolyte membrane cell". The PEMFC was initially developed by NASA in the 1960s, it is the most studied type of fuel cell currently and its main fuel is hydrogen. Its solid acid electrolyte based on polymers is NafionR ($C_7HF_{13}O_5S.C_2F_4$). There are others: FlemionR, AciplexR, DowR. The perfluorinated polymer membrane onto which SO^{3-} or COOH sulfonate groups are grafted (Close to Teflon). Its operating temperature is between 60 and 120°C. Electrodes are made by depositing a mixture of platinum-plated carbon powder, PTFE particles and liquid polymer electrolyte on a conductive carbon fabric. In the anode, the hydrogen ions cross the polymer membrane to the cathode while the electrons enter the electrical circuit then join the cathode.

Anode $\qquad$ $H_2 + 2H_2O \rightarrow 2H_3O^+ + 2e^-$ $\qquad$ ou $\qquad$ $H_2 \rightarrow 2H^+ + 2e^-$ $\qquad$ (1.8)

Cathode $\qquad$ $^1/_2\,O_2 + 2H_3O^+ + 2e^- \rightarrow 3H_2O$ ou $\qquad$ $O_2 + 4H^+ + 4e^- \rightarrow 2H_2O$ $\qquad$ (1.9)

Reaction Balance $\qquad$ $^1/_2\,O_2 + H_2 \rightarrow H_2O$ $\qquad$ (1.10)

$O_2 + 4H^+ \rightarrow 2H_2O$ (2nd form) $\qquad$ (1.11)
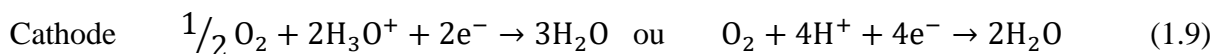
Standard voltage = 1.23 V.

The acid electrolyte is insensitive to CO_2, it therefore accepts all types of fuels (pure or from reforming); the Platinum catalyst is very sensitive to CO and its manufacturing cost is very high.

Fuel cell efficiency is limited (40%), as well as startup time is reduced. It has a wide power spectrum.

2.4.3 Alkaline fuel cell (AFC)

The AFC is a hydrogen fuel cell, and among the first cells developed (the 1950s). It is characterized by a basic (or alkaline) liquid electrolyte (KOH) and its electrodes consisting of a film of PTFE/carbon powder mixture pressed on a nickel grid (current collector) and covered with a hydrophobic porous layer (PTFE) on the gas side. Its operating temperature is 70 to 90°C. It may increase if the fuel cell is supplied under pressure or if the electrolyte is very concentrated.

Dihydrogen (H_2) is brought to the anode, it then reacts with hydroxide (HO^-). This reaction creates water (H_2O) and electrons (e^-).

Anode

$$H_2 + 2HO^- \rightarrow 2H_2O + 2e^- \tag{1.12}$$

Electrons circulate through an external circuit towards the cathode, where they react with water (H_2O) and dioxygen (O_2). This process creates hydroxide (OH^-) which recharges the electrolyte.

Cathode

$$O_2 + 2H_2O + 4e^- \rightarrow 4\,OH^- \tag{1.13}$$

Reaction Balance $\qquad\qquad O_2 + 2H_2 \rightarrow 2H_2O \qquad\qquad$ (1.14)

Standard voltage = 1.23 V.

The advantages of basic electrolyte are that, the maximum current density is a few amps per cm², it has very good efficiency at the operating point: 65%.

The catalysts are Nickel type for the anode and activated carbon for the cathode (no rare metal) therefore the manufacturing cost is reduced.

AFCs are the cheapest fuel cells, they work at low temperatures, their start-up time is reduced and their lifespan is long (> 15,000 h).

But, this electrolyte capable of reacting with the CO_2 present in combustible gases by the reaction:

$$CO_2 + 2OH^- \rightarrow CO_3^{2-} + H_2O \tag{1.15}$$

We fear the deterioration of the conductivity of the electrolyte so it is crucial to operate only with pure fuels (H_2 and O_2).

2.4.4 Phosphoric Acid Fuel Cell (PAFC)

The phosphoric acid fuel cell is currently at an advanced stage of development; research began in the 1970s. This type of cell has a liquid phosphoric acid electrolyte and its electrodes are made of carbon covered with a fine layer of platinum.

At the anode, hydrogen decomposes into positive ions and electrons.

$$H_2 \rightarrow 2H^+ + 2e^- \tag{1.16}$$

At the cathode, hydrogen is oxidized, which produces water.

$$O_2 + 4H^+ + 4e^- \rightarrow 2H_2O \tag{1.17}$$

The operating temperature of the system is between 150 and 220°C, the water produced therefore comes out in the form of steam. The PAFC is a cell specially designed for stationary use. In fact, the fuel cell is not designed to stop because the temperature of the electrolyte must not fall below 42.35°C, the melting temperature point of phosphoric acid; it would solidify.

The electrolyte being insensitive to CO_2, PAFCs can use reformed hydrogen without it being purified.

2.4.5 Molten Carbonate Fuel Cell (MCFC)

Molten carbonate fuel cells are part of the second generation. They are in fact fuel cells which operate at high temperatures (600 to 660°C).

The electrolyte is made up of a blend of lithium carbonate (Li_2CO_3) and potassium carbonate (K_2CO_3) at concentrations of 62 and 38% respectively, while the electrodes are mainly made of nickel. Nickel added to magnesium oxide or lithium aluminate has sufficient catalytic activity to ensure reforming on the anode at 650°C with a yield close to 100%, at the cathode, the catalyst is NiO$^+$Li. The ions which pass through the electrolyte are CO_3^{2-} molecules. At the anode, there is oxidation of hydrogen by CO_3^{2-}.

$$2CO_3^{2-} + 2H_2 \rightarrow 2CO_2 + 2H_2O + 4e^- \tag{1.18}$$
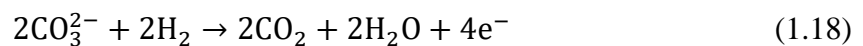
The electrons move via the external circuit and at the cathode, oxygen and carbon dioxide react, CO_2 comes from the anode reaction.

$$O_2 + CO_2 + 4e^- \rightarrow CO_3^{2-} \tag{1.19}$$

The electrolyte is then recharged; reformed hydrogen can also be used with MCFC batteries. In this case, the reaction at the anode will be.

$$2CO_3^{2-} + H_2 + CO \rightarrow 3CO_2 + H_2O + 4e^- \tag{1.20}$$
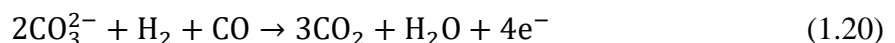
For the same reason as for DMFCs, similar results can be obtained by directly using methane, ethanol and gasified coal. Thanks to the elevated operating temperature of the cell, it is possible to have internal reforming. However, the high temperature of this battery increases the corrosion of the electrodes by the electrolyte. Battery efficiency can reach up to 60%. MCFC type fuel cells do not use expensive metals, so they are relatively inexpensive.

2.4.6 Solid oxide fuel cell (SOFC)

Solid oxide fuel cells are one of the high temperature fuel cells. They operate from 700 to 1000°C. As with MCFCs, they therefore have stationary use. Their electrolyte is a nonporous metal oxide, made of ceramic. It is most often yttrium-stabilized zirconia with the formula $(ZrO_2)_{1-x}(Y_2O_3)_x$. The electrodes are also ceramic: the anode is very often a cermet (metallic ceramic) based on nickel dispersed on stabilized zirconia (Ni-ZrO_2) or a cobalt doped zirconia (Co-ZrO_2). At the cathode, the catalyst is a system of oxides with a perovskite structure based on rare earth and a transition metal. Most often, lanthanum manganite is used, often doped with strontium: $(LaSr) MnO_3$. Thus, a reaction of oxidation of hydrogen by oxygen ions takes place at the anode.

$$H_2 + O^{2-} \rightarrow H_2O + 2e^- \qquad (1.21)$$

Electrons migrate to the cathode through the external circuit while simultaneously, four electrons react with a dioxygen molecule at the cathode:

$$O_2 + 4e^- \rightarrow 2O^{2-} \qquad (1.22)$$

The electrolyte is again charged with oxygen ions. In this type of cell, there are only two phases, the solid and the gas, thus eliminating all the problems linked to the poisoning of the electrodes by the electrolyte or by gases. In addition, the high operating temperature allows good efficiency of up to 70%. Research is being done to develop a SOFC operating at a lower temperature: 700°C, which would reduce stress on materials.

2.5 Advantages and disadvantages of fuel cells [21,22]

Fuel cells are considered an emerging technology and the energy source of the future. Contrary to common opinion, there are advantages and disadvantages to using and producing fuel cells.

2.5.1 Advantages

Renewable and clean energy: Though removing it from water presents certain obstacles, hydrogen is the most widespread component in the universe and a particularly renewable and

abundant source of energy that will be suitable for meeting our future zero-carbon requirements for heat supply and combined power.

Greater Efficiency Compared to Other Energy Sources: Compared with various conventional power sources, including several green power alternatives, hydrogen fuel cells are significantly more effective in generating electricity. More production can be achieved per kilogram of fuel due to this fuel efficiency. For instance, an ignition power plant typically produces energy at a 33–35 percent efficiency rate; whereas, a hydrogen fuel cell has the ability to produce electricity at a 65 percent efficiency rate.

Reliability: As water and heat are the fundamental byproducts of hydrogen fuel cells, they produce a source of energy that is intrinsically pure and has no detrimental effects on the environment while operating. Hydrogen can provide electricity without the requirement for huge fields, contrary to hydropower or biofuel. Because fuel cells don't have any moving parts, there is a lower possibility of a mechanical failure, making them extremely dependable. They are therefore an excellent option for situations where downtime is unacceptable.

Ability to adapt: As technology develops, hydrogen fuel cells will be capable to supply electricity for a range of consumer electronics and stationery. Applications for fuel cells are numerous, ranging from providing electricity for big buildings or even entire cities to powering tiny gadgets. They can also be utilized to power vehicles like buses and cars.

Longevity: Because of its extended lifespan and low maintenance requirements, fuel cells can function well for many years with little care. Because of this, they are an affordable long-term solution for producing power.

2.5.2   Disadvantages

Extraction of Hydrogen: Even though it's the most plentiful component in the universe, Hydrogen is not a standalone substance. Therefore, it must be separated from carbon-based fossil fuels or removed from the water by electrolysis. It takes a significant amount of energy to succeed in one of these techniques. This energy may be expensive and greater than that which is gained from the hydrogen itself. Furthermore, the removal process typically requires the use of fossil fuels, which compromises the environmental effectiveness of hydrogen due to its obvious lack of stored and captured Carbone.

Collection of hydrogen: The process of moving and storing hydrogen is far more difficult than that of moving and storing coal and natural gas. Consequently, utilizing hydrogen fuel cells as an energy supply requires extra costs.

Extremely Ignitable: There are obvious safety concerns with hydrogen as it is a very flammable fuel. Hydrogen is a gas that burns in the surrounding air at quantities between 4 and 75%.

2.6   Application of fuel cells [12]

Fuel cell technology is developed for very broad application areas which extend to:

* Decentralized electricity production (up to a hundred megawatts).

* Industrial or centralized cogeneration (up to 50 MW): Fuel cells are utilized for primary or supplemental electricity in commercial and industrial buildings, frequently in cogeneration applications.

* Cogeneration of individual homes (1 to 10 kW): In some areas, household combined heat and power (CHP) systems that provide heat and electricity to homes are powered by fuel cells.

* Power supply for isolated sites (10 to 200 kW): Fuel cells can provide power to equipment in hard-to-reach locations.

* Electric vehicles (around 50 kW): In comparison to battery-electric vehicles, hydrogen-powered vehicles use fuel cells, which provide larger ranges and faster refueling times.

* Buses (around 200 kW): Many cities are using fuel cell buses and trucks to lessen their reliance on fossil fuels and pollutants.

* Ships and submarines (in modules of 200 to 500 kW): Ships and submarines employ fuel cells because of their great efficiency and low emissions.

 * Portable applications (1 to 100 W): fuel cells are being produced for laptops, cellphones, and different portable devices to increase battery life.

* Spacecraft (10 to 50 kW): In space missions such the Apollo program, fuel cells have been utilized to supply astronauts with water and power.

3   Solid Oxide Fuel Cell

A solid oxide fuel cell is a system for producing electricity from a fuel (hydrogen) and an oxidant (oxygen). The SOFC elementary cell is composed of two electrodes (anode and cathode) separated by a solid electrolyte. The fuel, generally hydrogen, is introduced into the anode compartment where it undergoes an oxidation reaction. The electrons produced pass through the external electrical circuit. Oxygen is introduced into the cathodic compartment where it is reduced to oxide ions (O^{2-}) by electrons derived from oxidation. These O^{2-} ions

diffuse through the ionic conducting electrolyte up to the anode where they react with H^+ ions releasing electrons to generate electricity. The reaction produces H_2O, which exits the anode through its pores [23] (Figure 1.7).

A solid oxide fuel cell is entirely fabricated from semiconductor materials. This ceramic construction of all-solid-state minimizes material corrosion. The composition of each element must be chemically and thermally consistent with each element of the SOFC, and must have similar coefficients of thermal expansion in order to preserve good mechanical strength of the interfaces during variations in fuel cell temperature. A variety of complex metal oxides including rare earth elements are used as SOFC materials due to their significant chemical stability.
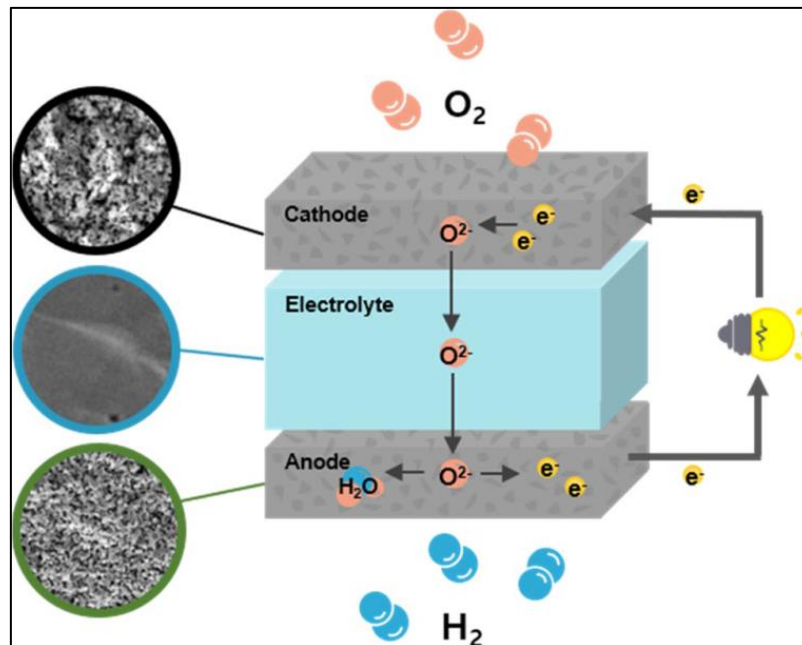
Figure 1. 7. Schematic of a SOFC fuel cell [24]

Why Solid Oxide Fuel Cell?

Solid oxide fuel cells have lately become more popular than other fuel cell types due to:

* Flexible fuel choice and internal reforming: Numerous fuels, including hydrogen, diesel fuel, methanol, and carbon based fuels like natural gas, can be used in SOFC [25,26].

* Efficiency: SOFC integration into a hybrid system greatly enhances its potential for significant electrical energy efficiency. Its highly stable and simple architecture makes it suitable to basic manufacturing processes [27].

* Good reactive activity: Because of their high operating temperature, SOFCs have fast electrochemical reactions, which increases electrode kinetics processes and lowers activation losses.

* Energy stability: Decreases both the amount of oil utilized and imported. In addition, because SOFCs operate at an elevated temperature, the heat they release can be used for CHP and other power-generating processes.

* Application: Vehicle transportation, stationary power generation, decentralized generating units, and military uses are among the applications for SOFCs.

* Cell control: Because SOFCs are solid ceramic cells, they do not experience many of the problems that other fuel cells do, like catalyst wetting, electrode flooding, and electrolyte migration.

3.1   Anode

The anode of the SOFC is the site of the reaction between the hydrogen gas and the O^{2-} ions coming from the electrolyte.

$$H_2 + O^{2-} \rightarrow H_2O + 2e^- \tag{1.24}$$
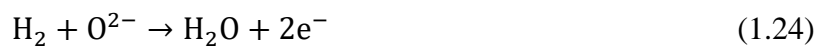
The area where this reaction occurs are the regions of coexistence of electrons, O^{2-} ions and hydrogen gas called "triple point" or "triple phase boundary TPB". The porous anode transport the fuel to the anode-electrolyte interface, additionally, it is employed to remove water vapor that has generated.

Hence, the anode material must satisfy various conditions:

* Present high electronic conductivity, from 10 to 100 S.cm-1.

* Be chemically stable up to partial pressures of oxygen (10-25 Pa).

* Present good catalytic activity towards the reaction.

* Have an expansion coefficient compatible with that of the other constituents of the cell.

For SOFC, a large range of materials have been regarded as anode materials depending on microstructure, cell manufacturing and electrochemical effectiveness.

The most popular SOFC anode is made from cermets of nickel and yttrium oxide stabilized zirconia (Ni–YSZ).

Particle size, porosity, contact angle between particles, and active triple phase boundary (TPB) are among the microstructural properties of these ceramics that are crucial for regulating cell performance and guaranteeing anode stability [28].

Other commonly used anode materials include Ni-ScSZ (scandia-stabilised zirconia), Ni-Ceria, etc... [24]
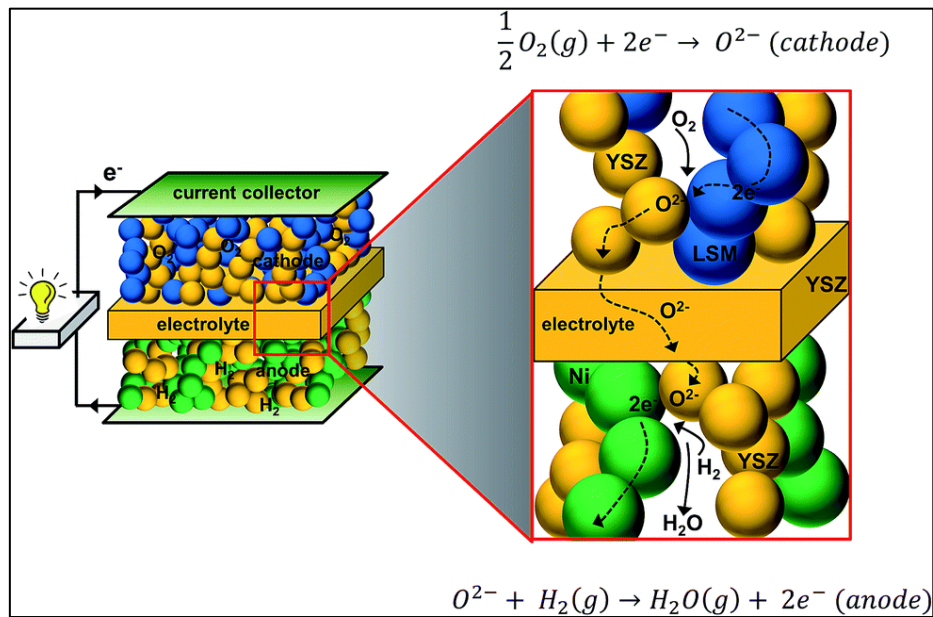
**Figure 1. 8. TPB reduction reaction of a LSM-YSZ cathode;
and the oxidation reaction on the TPB of a Ni-YSZ anode [29]**

3.2   Cathode

The cathode is the site of the oxygen reduction reaction:

$$O_2 + 4e^- \rightarrow 2O^{2-} \tag{1.23}$$

It is porous to enable the oxygen gas to flow to the reaction point. The gas is adsorbed then dissociated and reduced to O^{2-} ions thanks to the existence of oxygen vacancies.

As in the case of the anode, the place where this reaction occurs and where the electrons of the cathode, the oxygen vacancies of the electrolyte and the oxygen gas are simultaneously present is called Triple Phase Boundary (Figure 1.8).

The generally accepted specifications for the cathode material are as follows:

* Have high electro-catalytic activity to reduce oxygen and high electrical conductivity (>100 S.cm-1).

* Have good chemical, morphological and dimensional stability in the oxidizing environment.

* Have good electrochemical properties towards oxygen reduction.

* Have high mechanical and chemical compatibility with other cell components, chemical interactions or elementary inter-diffusions between the cathode and the adjacent parts should

be limited to prevent the appearance of non-conductive secondary phases, changes in expansion coefficient and the induction of electronic conductivity in the electrolyte.

Yet for SOFC applications, the variety of cathode materials is now well-established.

The most widely utilized cathode material available at this moment is p-type lanthanum manganite ($LaMnO_3$). Its conductivity will be enhanced by doping with rare earth elements (for example Sr, Ce, and Pr).

The most popular and well-researched for such application is synthetic LSM, or lanthanum manganite doped strontium ($La_{1-x}Sr_xMnO_3$); LSM exhibits superior electrical conductivity, remarkable chemical stability in an oxidizing environment at elevated temperatures (~1000 °C), and corresponds with YSZ in terms of thermal expansion.

The electrolyte materials are especially important because extra care must be made to coordinate the thermal expansion coefficients and prevent undesirable reactions at the interface [24].

3.3 Electrolyte

The electrolyte supports the oxide ion migration from one electrode to another, to round out the electrical circuit. Electrolyte materials should to be highly ionic conductive while insulating electronic conductivity to prevent short circuits between the electrodes.

The commonly accepted specifications for the electrolyte material are as follows:

* Have purely ionic conductivity by oxide ions O^{2-}.

* Be stable throughout a wide range of oxygen partial pressures.

* Have good thermal and mechanical properties, such as good mechanical resistance to thermal gradients.

* Be thermo-mechanically and chemically consistent with all other constituents of the cell at its operating temperature. as well as at the temperatures reached during cell manufacture.

Metal oxides that conduct oxide ion are often used as SOFC electrolytes. Indeed, to improve the ionic and mechanical conductivity properties while being solid, ZrO_2 zirconias are doped with Y_{3+} ions, or even Ca_{3+}, Sc_{3+}, Ln_{3+}, thus creating electronic vacancies and allowing the mobility of oxygen ions. YSZ (Yttrium Oxide 3,8 or 10%) are typical materials presently used as electrolyte for SOFCs.

At temperatures beyond 700°C, it exhibits moderate conductivity, although at these temperatures, its electrical conductivity is insignificant.

Other materials also incriminated such as Scandia-stabilized zirconia (ScSZ), (La, Sr) (Ga, Mg, Co) O_3 (LSGMC), (La, Sr) (Ga, Mg) O_3 (LSGM), etc. However, certain materials (e.g. ScSZ) are not economically viable [24].

3.4   Interconnectors

The interconnectors have several roles: they make it possible to assemble the elementary cells and their geometry must allow the distribution of gases. They require to be stable in oxidizing and reducing environments, and have an excellent electronic conductivity. They must also have a high thermal conductivity coefficient in order to evacuate heat. The materials conventionally used at high temperatures are lanthanum chromites $MaCrO_3$ [30].

Currently, SOFC operates at a relatively elevated temperature of around 1000°C, so high reaction rates allow efficient power conversion without the need for expensive catalysts.

3.5   Configuration and fabrication of SOFC

SOFCs may be classified based on their geometric design, the most popular of these geometries are succinctly presented below:

Planar design: Planar SOFCs are made up of flat layers of electrodes, electrolytes, and current collectors arranged on top of one another, as depicted in Figure 1.9. The arrangement is easy and inexpensive to build.

The planar geometry offers high attractive power densities, reaching 1.4 W/cm² in single-cell tests and 0.7 W/cm² for stacked system (at U=0.7V and T=800° C). Furthermore, the assembly of cells and interconnection plates in flat layers makes it possible to obtain good compactness of the system. However, in general, planar geometry has the disadvantage of low robustness both during thermal or redox cycles and in stationary operation.

Tubular design: The main advantage of the tubular configuration lies in a simplification of the sealing system leading to great robustness of the system (Figure 1.10). Thus this type of configuration could be cycled 100 times from room temperature to 1000°C without loss of electrochemical performance.

Stationary aging tests over several thousand hours were also carried out with performance degradation rates of less than 0.1% per 1000 hours. Unfortunately, a large available volume is necessary to ensure the stacking of the tubes.

In addition, the electrochemical performances achieved by this type of system are low due to the high ohmic drops induced by current collection (of the order of 0.15-0.2 W/cm² at U=0.7V and T =950-1000°C) [31].

Integrated planar design: Integrated planar SOFC is a combination of the planar and tubular shapes that aims to maintain the particular features of the both configuration arrangements, borrowing the low cost fabrication, short current pathway of the planar design and the thermal compliance characteristic from the tubular design (Figure 1.11).
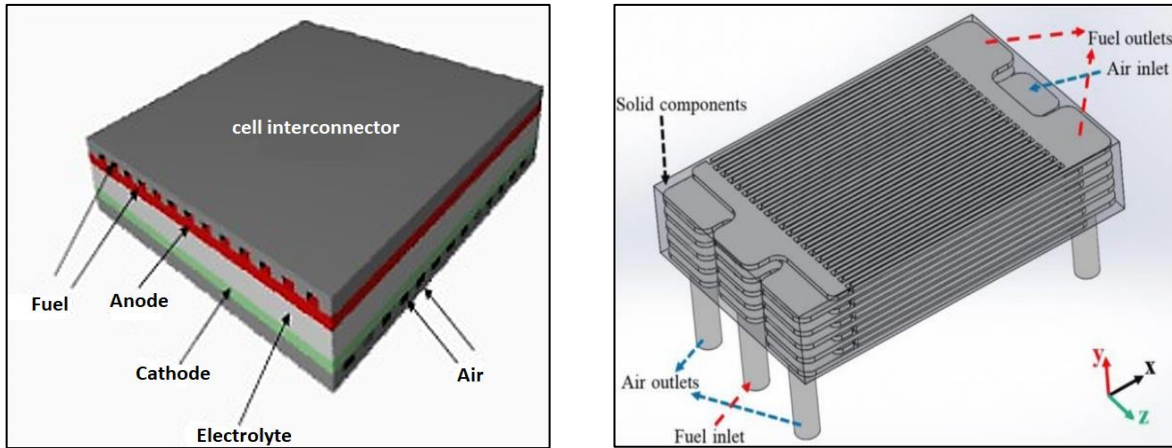
Figure 1. 9. Schematic of a SOFC in planar configuration. [32,33]
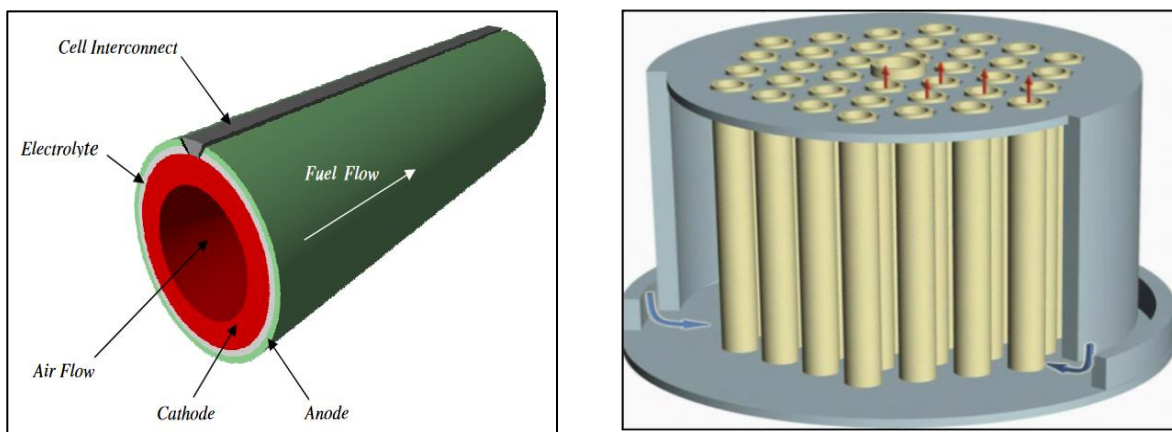
Figure 1. 10. Diagram of a SOFC in tubular configuration. [32,34]
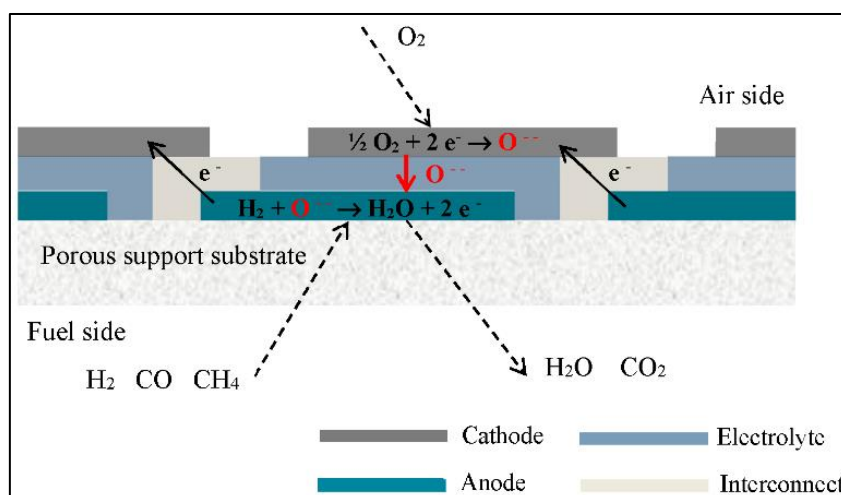
Figure 1. 11. Diagram of a SOFC in integrated configuration [35]

In a system like that shown in Figure 1.12, vaporized fuel and air are converted in a CPOX reactor to produce a syngas mixture (i.e., a mixture of H_2, H_2O, CO, CO_2 and N_2). The syngas enters the anode side of the SOFC cell. The preheated air enters the cathode side of the SOFC cell. Unspent air and fuel leaving the stack are blended and burned in a catalytic tail-gas incinerator. Hot gases exiting the tail-gas burner are used in a heat exchanger to preheat the air flowing into the SOFC stack. The raw power from the SOFC is processed by the power electronics before being delivered to the application load [36].
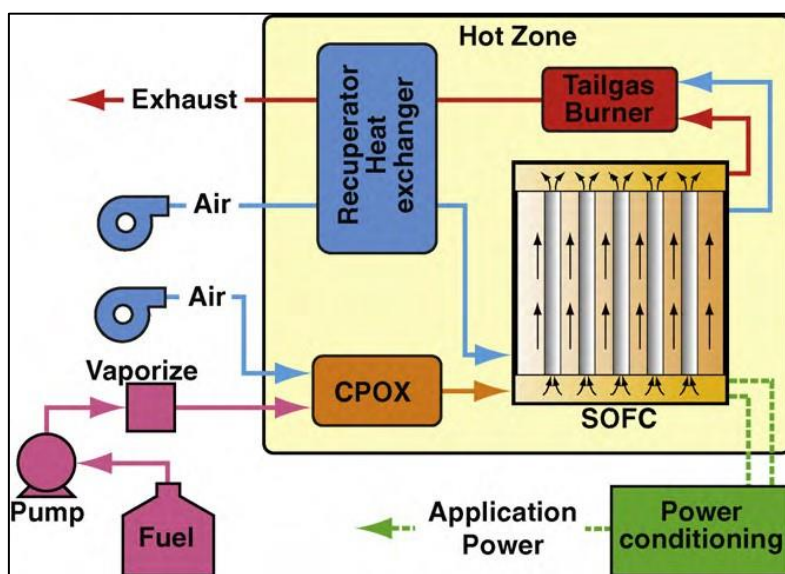
Figure 1. 12. Schematic diagram of the SOFC system [36]

4   Conclusion

One of the most promising technologies to help fulfilling the growing demand for energy production and the requirement to lessen its environmental impact is fuel cell systems. The many kinds of fuel cells and their uses are outlined in this chapter. It describes the solid oxide fuel cell, including its components, operating principle, and many classifications.

References

[1] Singhal, S. C., & Kendall, K. (Eds.). High-temperature solid oxide fuel cells: fundamentals, design and applications. 2003; Elsevier.

[2] Grove, W. R. XXIV. On voltaic series and the combination of gases by platinum. The London, Edinburgh, and Dublin Philosophical Magazine and Journal of Science, 1839; 14(86-87), 127-130.

[3] Grove, W. R. On a Gaseous Voltaic Battery. Philos. Mag. J. Sci., 1842; 21, 417-420

[4] Larminie, J., Dicks, A., & McDonald, M. S. Fuel cell systems explained, 2003; (Vol. 2, pp. 207-225). Chichester, UK: J. Wiley.

[5] Andújar, J. M., & Segura, F. Fuel cells: History and updating. A walk along two centuries. Renewable and sustainable energy reviews, 2009; 13(9), 2309-2322.

[6] Giorgi, L., & Leccese, F. Fuel cells: Technologies and applications. The Open Fuel Cells Journal, 2013; 6(1).

[7] Milewski, J., Świrski, K., Santarelli, M., Leone, P., & Milewski, J. Advanced Methods of Solid Oxide Fuel Cell Modeling. Springer London. 2011; (pp. 91-200).

[8] De Bruijn, F. The current status of fuel cell technology for mobile and stationary applications. Green chemistry, 2005; 7(3), 132-150.

[9] Tsampas, M. N., Pikos, A., Brosda, S., Katsaounis, A., & Vayenas, C. G. The effect of membrane thickness on the conductivity of Nafion. Electrochimica Acta, 2006, 51(13), 2743-2755.

[10] Affoune, A. M., Yamada, A., & Umeda, M. Conductivity and surface morphology of Nafion membrane in water and alcohol environments. Journal of power sources, 2005; 148, 9-17.

[11] Vayenas, C. G., Tsampas, M. N., & Katsaounis, A. First principles analytical prediction of the conductivity of Nafion membranes. Electrochimica acta,2007; 52(6), 2244-2256.

[12] Mabrouk, W. Synthèse et caractérisation de nouvelles membranes protoniques: Applications en pile à combustible à membrane échangeuse de protons (Doctoral dissertation, Conservatoire national des arts et metiers-CNAM; Université Tunis El Manar. Faculté des Sciences Mathématiques, Physiques et Naturelles de Tunis (Tunisie)), 2012.

[13] Derbeli, M., Barambones, O., Silaa, M. Y., & Napole, C. Real-time implementation of a new MPPT control method for a DC-DC boost converter used in a PEM fuel cell power system. In Actuators, 2020; (Vol. 9, No. 4, p. 105). MDPI.

[14] Quadakkers, W. J., Piron-Abellan, J., Shemet, V., & Singheiser, L. Metallic interconnectors for solid oxide fuel cells–a review. Materials at high temperatures, 20(2), 2003; 115-127.

[15] Zhu, Y. n-Hexadecane, Petroleum Diesel and Biodiesel Fuels for a Direct Hydrocarbon Phosphoric Acid Fuel Cell (Doctoral dissertation, Université d'Ottawa/University of Ottawa), 2015.

[16] Dicks, A. L. The role of carbon in fuel cells. Journal of Power Sources, 2006; 156(2), 128-141.

[17] Fuel Cell Handbook (seventh edition), Department of Energy Office of Fossil Energy, 2004; 26507-0880.

[18] Danilov, V. A., & Tade, M. O. An alternative way of estimating anodic and cathodic transfer coefficients from PEMFC polarization curves. Chemical Engineering Journal, 2010; 156(2), 496-499.

[19] Litster, S., & McLean, G. J. J. O. P. S. PEM fuel cell electrodes. Journal of power sources, 2004; 130(1-2), 61-76.

[20] Melendez-Ceballos, A. Adequacy of new electrolyte compositions and nanostructured protective layers for the cathode of molten carbonate fuel cells (Doctoral dissertation, Université Pierre et Marie Curie-Paris VI; Instituto Nacional de Investigaciones Nucleares (ININ)), 2017.

[21] https://techetch.com/blog/advantages-and-disadvantages-to-fuel-cells/

[22]https://www.twi-global.com/technical-knowledge/faqs/what-are-the-pros-and-cons-of-hydrogen-fuel-cells

[23] Jo, S., Sharma, B., Park, D. H., & Myung, J. H. Materials and nano-structural processes for use in solid oxide fuel cells: A review. Journal of the Korean Ceramic Society, 2020; 57(2), 135-151.

[24] Patabendige, C. N. K. Material characterisation, phase transitions, electrochemical properties and possible fuel cell applications of $Nd_{2-x}Pr_xCuO_4$ and Nd [subscript (2-xy)] La [subscript (y)] Pr_xCuO_4 systems (Doctoral dissertation, University of St Andrews), 2012.

[25] Viswanathan, B. and M.A. Scibioh, Fuel cells : principles and applications. 2007, Hyderabad Boca Raton, FL: Universities Press ; Distributed by CRC Press. x,2012; 494 p.

[26] Singhal, S. C. Solid oxide fuel cells for stationary, mobile, and military applications. Solid State Ionics, 2002; 152, 405-410.

[27] Bove, R., & Ubertini, S. (Eds.). Modeling solid oxide fuel cells: methods, procedures and techniques. Springer Science & Business Media, 2008.

[28]. Badwal, S. P. S. Stability of solid oxide fuel cell components. Solid State Ionics, 2001; 143(1), 39-46.

[29] Dunyushkina, L. A. Solid oxide fuel cells with a thin film electrolyte: A review on manufacturing technologies and electrochemical characteristics. Electrochemical Materials and Technologies. 2022. Vol. 1.№ 1, 1(1).

[30] Lalanne, C. Synthèse et mise en forme de nouveaux matériaux de cathode pour piles ITSOFC: réalisation et tests de cellules (Doctoral dissertation, Université Sciences et Technologies-Bordeaux I), 2005.

[31] Laurencin, J. Fonctionnement sous Méthane d'une pile à combustible «SOFC»: optimisation des performances et de la durabilite (Doctoral dissertation, Institut National Polytechnique de Grenoble-INPG), 2008.

[32] Sharp, M. D. The Ba-Pb-O system and its potential as a solid oxide fuel cell (SOFC) cathode material (Doctoral dissertation, University of St Andrews), 2007.

[33] Ding, K., Zhu, M., Han, Z., Kochetov, V., Lu, L., & Chen, D. Momentum-species-heat-electrochemistry distribution characteristics within solid oxide fuel cell stack with complex inter-digital fuel channels. Ionics, 2020; 26, 4567-4578.

[34] Sanandaji, B. M., Vincent, T. L., Colclasure, A. M., & Kee, R. J. Modeling and control of tubular solid-oxide fuel cell systems: II. Nonlinear model reduction and model predictive control. Journal of Power Sources, 2011; 196(1), 208-217.

[35] Costamagna, P., Grosso, S., Travis, R., & Magistri, L. Integrated planar solid oxide fuel cell: Steady-state model of a bundle and validation through single tube experimental data. Energies, 2015; 8(11), 13231-13254.

[36] Ohadi, M., Choo, K., Dessiatoun, S., & Cetegen, E. Next generation microchannel heat exchangers (pp. 33-65). New York: Springer; 2013.

Chapter 2: Model Development

1   Introduction

A three dimensional model for a single hydrogen fed anode-supported solid oxide fuel cell is developed and implemented in the commercial software COMSOL Multiphysics (version 5.3a). In this chapter, we introduce a description of the mathematical model numerically simulated, involving the governing differential equations and chemical phenomenon which takes place simultaneously in different SOFC components.

The SOFC mathematical model is divided into a number of small sub-models in order to effectively create mathematical relations that explain phenomena occurring within each constituent.

Figure 2.1 shows the schematic of the simulated fuel cell unit, consisting of active cathode and anode layers (AFL/CFL), supporting anode layer (ASL), cathode diffusion layer (CDL), electrolyte and interconnectors, dividing the total cell into nine zones.

<div align="center">(a)   (b)</div>
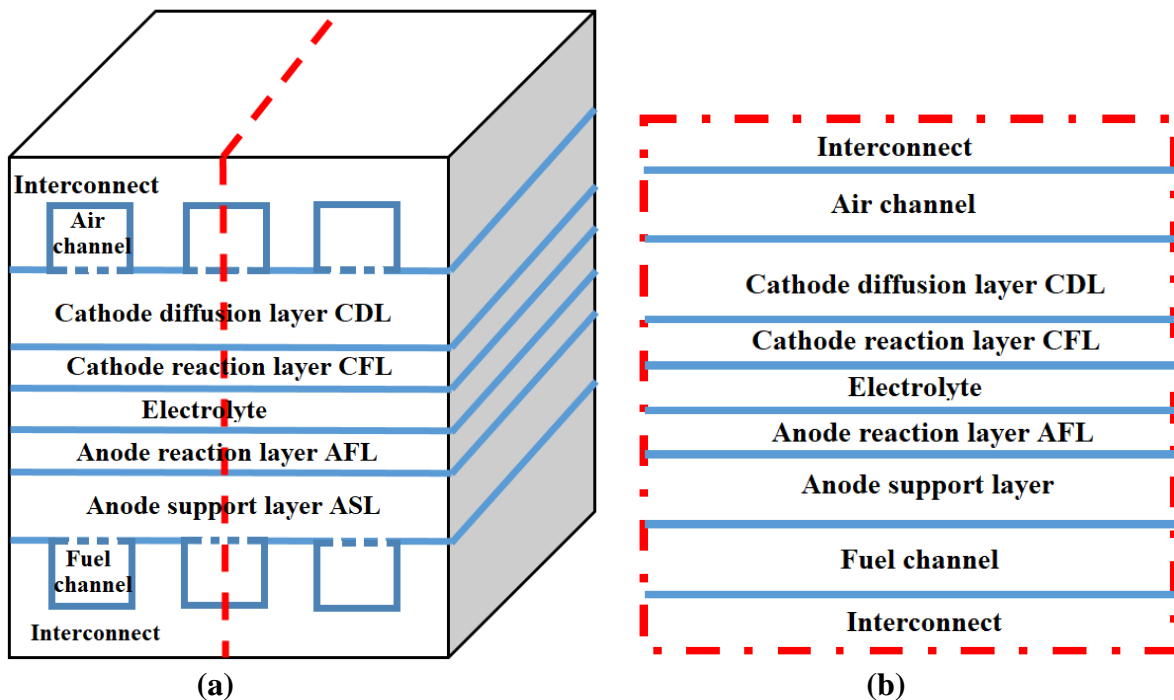
Figure 2. 1. 3D computational domain of SOFC, (b) plane at the mid-width location of the cell

The assumptions applied are the following: the SOFC operates at steady-state conditions, flow conditions are established laminar and incompressible in the channels, the involved gases in both channels are presumed to behave like ideal gases, the ionic and electronic conductors are considered to be isotropic and homogenous, gas leakage and heat transfer by radiation are neglected.

The equation for momentum, mass, electron, ion, and heat transport have been simultaneously solved, as described in the following section.

Table 2-1 provides an overview of the fundamental equations and physical phenomena that were used to develop the model for every sub-domain.

Table 2. 1. Overview of the fundamental characteristics of the SOFC model's submodels

Submodels	Physical phenomena	Fundamental Equations
Channel	Mass transport	Ideal gas
	Momentum transport	Darcy-Brinkman
	Species transport	Stefan-Maxwell
	Energy transport	Fourier
Electrode diffusion layer	Mass transport	Ideal gas
	Momentum transport	Darcy-Brinkman
	Species transport	Stefan-Maxwell
	Energy transport	Fourier
	Charge transport	Ohms
Electrode reaction layer	Mass transport	Ideal gas
	Momentum transport	Darcy-Brinkman
	Species transport	Stefan-Maxwell
	Energy transport	Fourier
	Electrochemical reaction	Nernst, Butler-Volmer
	Charge transport	Ohms
Electrolyte	Energy transport	Fourier
	Charge transport	Ohms
Interconnector	Energy transport	Fourier
	Charge transport	Ohms

2   Electrochemical model

Since the conversion of internal electrochemical energy is the fundamental principle of operation, an emphasis on the thermodynamic aspect is required. Each chemical reaction has a Gibbs free energy that varies based on the components' chemical activity, chemical bond energies, and operating parameters [1].

$$\Delta_r G = \Delta_f G^0 + RT \times \ln\left(\frac{a_{ox}}{a_{red}}\right) \tag{2.1}$$

$\Delta_f G^0$ is the conventional Gibbs energy computed at atmospheric pressure assuming the gas generation energy, R is the gas constant, T is the operating temperature, a_{ox} and a_{red} are respectively the oxidant and reducer activities.

Depending on the quantity of electrons exchanged, the reaction's electrical potential is proportionate to its free Gibbs energy. Through the development of this formulation, the Nernst relation is obtained, enabling the representation of the system's electromotive force or electrical potential as a function of the partial pressure, (i.e., gas concentration) [1]:

$$E_{rev} = -\frac{\Delta_r G}{nF} \tag{2.2}$$

$$E_{rev} = E^0 + \frac{RT}{nF} \times \ln\left(\frac{P_{H_2O}}{P_{H_2}P_{O_2}^{0.5}}\right) \tag{2.3}$$

Where E_{rev} is the reversible potential, E^0 is the standard reversible potential, and P_i is the partial pressure of the species i.

$$E^0 = 1.271 - 2.731\ 10^{-4}\ T \tag{2.4}$$

During operation, a variety of electrical, chemical, and diffusion activities take place inside the fuel cell.

Each of these affects the amount of electricity produced globally, which has an effect on cell voltage by generating irreversibility, and that in turn makes it decrease as current increases.

We introduce the concept of overpotential η to describe the potential losses in the fuel cell outside of equilibrium [1].

$$E(i) = E_{rev} - \eta_{act,a} - \eta_{act,c} - \eta_{ohm} - \eta_{conc,c} - \eta_{conc,c} \tag{2.5}$$

Where η_{act}, η_{ohm} , and $\eta_{conc,c}$ are the activation, ohmic and concentration polarization respectively.

Equation (2.5) can be represented on a graph called "polarisation curve". The polarisation curve supplies an illustration of the fuel cell performance; the cell potential is plotted as a function of the average current density. The polarisation curve differs depending on the conditions of operation (such as temperature), the reactants used, and their chemical properties. A typical curve is depicted in Figure 2.2. Herein, the three distinct regions are clearly visible, distinguished by the three distinct losses previously discussed.
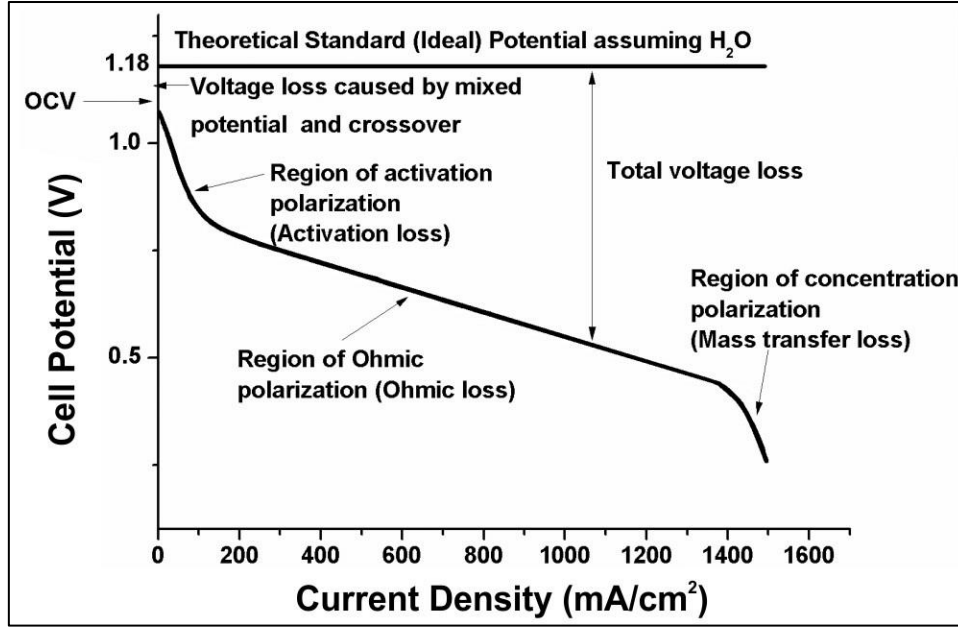
Figure 2. 2. Polarization curve for a typical fuel cell [2]

2.1 Activation polarization

The activation polarization occurs when the electrode's kinetics decrease and regulate the rate of an electrochemical reaction at the surface of the electrode, in other words, the activation polarization is directly correlated with the rate of the electrochemical reaction, it is defined as [3]:

$$\eta_{act,a} = \varphi_s - \varphi_l - E_{eq,a} \tag{2.6}$$

$$\eta_{act,c} = \varphi_s - \varphi_l - E_{eq,c} \tag{2.7}$$

Where φ_s and φ_l are the electronic and ionic phase potentials respectively, $E_{eq,a}$ and $E_{eq,c}$ are the equilibrium electrical potential difference in the electrodes.

At the electrode-electrolyte interfaces, the Butler-Volmer equation describes the relationship between the current density and the activation polarization of the reaction sites [4]:

$$i_a = A_{ve}\, i_{0,a} \left[\exp\left(\frac{n\alpha F \eta_{act,a}}{RT}\right) - \exp\left(\frac{n(1-\alpha)F\eta_{act,a}}{RT}\right) \right] \tag{2.8}$$

$$i_c = A_{ve}\, i_{0,c} \left[\exp\left(\frac{n\alpha F \eta_{act,c}}{RT}\right) - \exp\left(\frac{n(1-\alpha)F\eta_{act,c}}{RT}\right) \right] \tag{2.9}$$

Where i_0 is the exchange current density, F is the Faraday constant, α is the charge transfer coefficient, n is the number of electrons transferred per electrochemical reaction and A_{ve} is the electrochemical active area of the corresponding electrode.

The exchange current density, i_0, refers to the rate that reduced and oxidized species transfer electrons with the electrode, and defined as [3]:

$$i_{0,a} \;=\; \gamma_a \left(\frac{P_{H_2}}{P_{H_2,ref}}\right)^A \; \left(\frac{P_{H_2O}}{P_{H_2O,ref}}\right)^B \exp\!\left(\frac{-E_a}{RT}\right) \tag{2.10}$$

$$i_{0,c} \;=\; \gamma_c \left(\frac{P_{O_2}}{P_{O_2,ref}}\right)^C \; \exp\!\left(\frac{-E_c}{RT}\right) \tag{2.11}$$

Where γ_a and γ_c are the exponential factor for anode and cathode, E_a and E_c are the activation energy for anode and cathode, $P_{i,ref}$ and P_i are the reference partial pressures and partial pressure for species i.

2.2 Concentration polarization

A concentration polarization is produced at an electrode when there is a loss of potential because the system is unable to maintain the reactants at their initial concentration. The Concentration polarization may occur from the insufficient diffusion of gas throughout porous electrodes and the diffusion of products or reactants from the reaction site to the electrolyte or vice versa [5].

$$\eta_{conc,a} \;=\; \frac{R.T}{n_a.F} \;\; ln\left(\frac{P_{H_2O,TPB}\; .P_{H_2,b}}{P_{H_2,TPB}\; .P_{H_2O,b}}\right) \tag{2.12}$$

$$\eta_{conc,c} \;=\; \frac{R.T}{n_c.F} \;\; ln\left(\frac{P_{O_2,b}}{P_{O_2,TPB}}\right) \tag{2.13}$$

Where the index TPB refers to the three-phase boundary, and b to the electrode and gas channel boundary.

2.3 Ohmic polarisation

Ohmic losses can be attributed to the resistance that ions face while flowing through the electrolyte as well as the resistance that electrons face in the electrodes and electrical circuit. Ohm's law is obeyed by the electrodes and the electrolyte, we can express the ohmic polarisation by the following equation [5]:

$$\eta_{ohm} = R_{ohm} . i \tag{2.14}$$

$$R_{ohm} = \frac{\tau_a}{\sigma_a} + \frac{\tau_{el}}{\sigma_{el}} + \frac{\tau_c}{\sigma_c} \tag{2.15}$$

Where R_{ohm} the ohmic resistance, τ is the component thickness, σ_a , σ_c and σ_{el} are the conductivities for anode, cathode and electrolyte respectively and calculated as [5]:

$$\sigma_a = \frac{9.5\times10^7}{T} \exp\left(\frac{-1150}{T}\right) \tag{2.16}$$

$$\sigma_{el} = 3.34 \times 10^4 \exp\left(\frac{-10300}{T}\right) \tag{2.17}$$

$$\sigma_c = \frac{4.2\times10^7}{T} \exp\left(\frac{-1200}{T}\right) \tag{2.18}$$

Because of their microstructures and actual/functional material compositions, electrons and ions are in fact transported across longer distances in the electrodes. The structure-dependent tortuosities and volume fractions are used to account for this [3].

$$\sigma_{eff,s,a} = \sigma_a . \frac{V_{s,a}}{\tau_{s,a}} \tag{2.19}$$

$$\sigma_{eff,l,el} = \sigma_{el} . \frac{V_{l,el}}{\tau_{l,el}} \tag{2.20}$$

$$\sigma_{eff,s,c} = \sigma_c . \frac{V_{s,c}}{\tau_{s,c}} \tag{2.21}$$

Where V is the volume fraction for ion conductivity (l) and electron conductivity (s) of the solid phase, and τ is the tortuosity factor.

3   Electrode diffusion model

Mass conservation equation

By definition, the mass conservation equation, often known as the continuity equation, states that the rate of mass change in a unit volume must match the total number of species that enter or exit the volume during an amount of time.

When the steady state assumption is applied, mass conservation equation can be expressed as follows [5]:

$$\nabla.(\rho u) = 0 \tag{2.22}$$

Where u is the fluid velocity ρ is the fluid density of the species. Because of the high operating temperatures of SOFCs, the fluid density ρ is defined by the ideal gas law [5]:

$$\rho = \frac{p \sum x_i . M_i}{RT} \tag{2.23}$$

Where x_i is the gas mole fraction, M_i is the molecular mass of species i.

Momentum conservation equation

Momentum conservation equation can be expressed at the steady state condition as [6]:

$$\nabla.\left(\frac{\rho}{\varepsilon}\vec{u}\vec{u}\right) = \rho\vec{f} + \nabla.\vec{\tau} \tag{2.24}$$

Where ε denotes the porosity, $\vec{f}$ are the body forces including electromagnetic, gravity, and inertia forces, and $\nabla.\vec{\tau}$ is the shear stress tensor.

By adding a term to the Darcy equation that accounts for the viscous transport in the momentum balance, the Darcy-Brinkman equation is applied to define the momentum balance in the porous electrode diffusion layers.

The Darcy-Brinkman equation serves to define the momentum equilibrium in the porous electrode diffusion and support layers, Darcy-Brinkman equation is expressed as [6]:

$$\nabla.\left(\frac{\rho}{\varepsilon}\vec{u}\vec{u}\right) = -\vec{u}\frac{\mu}{K} + \rho\vec{f} + \nabla.\vec{\tau} \tag{2.25}$$

Where μ and K stand for the fluid viscosity and the permeability of the electrode support and diffusion layers.

In the SOFC, since they are both gases, fuel and oxidant are referred as Newtonian fluids, and in accordance with Newton's law of viscosity, the stress tensor may be presented [6]:

$$\vec{\tau} = \frac{\mu}{\varepsilon}[\nabla\vec{u} + (\nabla\vec{u})^T] - \left[p + \left(\mu u - \frac{2}{3\varepsilon}\mu\right)(\nabla.\vec{u})\right]\vec{I} \qquad (2.26)$$

Where, μu is the bulk velocity coefficient, and $\vec{I}$ is the identity matrix, it is well known that bulk viscosity is insignificant under the SOFC operating circumstances namely laminar flow and low flow rate.

The equation describing the conservation of momentum in a fluid moving through the electrode support and diffusion layers can be formulated as [7]:

$$\frac{1}{\varepsilon}\rho(\vec{u}.\nabla)\vec{u}\frac{1}{\varepsilon} = = -\vec{u}\frac{\mu}{K} + \rho\vec{f} + \nabla.\left(\frac{\mu}{\varepsilon}[\nabla\vec{u} + (\nabla\vec{u})^T] - \left[p + \left(\frac{2}{3\varepsilon}\mu\right)(\nabla.\vec{u})\right]\vec{I}\right) \qquad (2.27)$$

The velocity u stated in equations (2.24) to equation (2.27) is the averaged velocity; this enables the representation of the velocity field as a continuous entity spanning both the solid matrix and pores, facilitating the description of the flow using a uniform velocity profile.

The dynamic viscosities of the mixture and each contributing species in the gas phase are calculated using the following formula [5]:

$$\mu_i = \sum_{i=1}^{7} b_k \cdot \left(\frac{T}{1000}\right)^k \qquad (2.28)$$

$$\mu_g = \sum_i x_i.\mu_i \qquad (2.29)$$

b_k indicates the species dependent parameter and k denotes the number of species dependent parameters in the equation.

Species conservation equation

The species conservation equation represents the differential motion of each specific species in the fluid mixture [6].

$$\nabla.(\rho u\nabla\omega_i) + \nabla.j_i = R_i \qquad (2.30)$$

Where ω_i is the mass fraction, R_i is the mass source term, and j_i is the mass flux vector.

Given that the diffusion layer is a porous media, it becomes necessary to consider this porosity in the species balance. Therefore, equation (2-30) can be reformulated as follows:

$$\varepsilon \nabla . (\rho u \nabla \omega_i) + \nabla . j_i = R_i \qquad (2.31)$$

The species continuity equation, denoted as equation (2.31), comprises three terms. The initial term on the left signifies the convective fluxes, the subsequent term denotes the diffusive fluxes, and the final term corresponds to the flux resulting from chemical reactions. Considering the convective flux as negligible compared to the diffusive flux within the layer of electrodes, the species continuity equation is simplified to [6]:

$$\nabla . j_i = R_i \qquad (2.32)$$

The formulation of the Stefan-Maxwell model for a multicomponent system with n species is presented as [6, 8]:

$$c_g \nabla \omega_i = \sum_{j=1, j \neq i}^{n} \frac{x_j j_i - \omega_i j_j}{D_{ij}} \qquad (2.33)$$

Curtis and Bird [9] examined diffusive flux in multicomponent mixtures and suggested the mass flux vector as:

$$j_i = -D_i^T \nabla lnT - \rho_i \sum_{j=1}^{n} D_{ij} d_j \qquad (2.34)$$

Where D_i^T is the thermal diffusion coefficient, D_{ij} is the diffusion coefficient and d_j is the diffusional driving force of the species j described as:

$$d_j = \nabla x_j + \frac{1}{p} \left[(x_j - \omega_j) \nabla_p \right] \qquad (2.35)$$

The mole fraction x_j and the mass fraction ω_j are related as follows:

$$x_j = \frac{\omega_j}{M_j} M_n \qquad (2.36)$$

$$M_n = \sum_i \left(\frac{\omega_i}{M_i} \right)^{-1} \qquad (2.37)$$

In binary or multicomponent systems, the ordinary diffusion proceeds concurrently with the Knudsen diffusion.

When the frequency of collisions between the gas molecules and the pore wall rises, the term of Knudsen diffusion gets considerable; this occurs only when the pore diameters are less than the mean free route of the gas molecules. Therefore, with the inclusion of the Knudsen diffusion effect, Equation (2-33) transforms into [4]:

$$c_g \nabla \omega_i = \sum_{j=1, j \neq i}^{n} \frac{x_j j_i - \omega_i j_j}{D_{ij}} + \frac{j_i}{D_{Kn,ij}} \tag{2.38}$$

Where $D_{Kn,ij}$ is the Knudsen diffusion coefficient.

An effective diffusion coefficient can be obtained by combining and correcting both diffusion terms using certain geometric parameters that take into account the medium's porosity and tortuosity [6,10,11].

$$D_{ij}^{eff} = \frac{\varepsilon}{\tau} \cdot \left(\frac{D_{ij}.D_{k,ij}}{D_{ij} + D_{k,ij}} \right) \tag{2.39}$$

Where the porosity ε and the tortuosity τ of the porous medium are expressed as [6,12,13]:

$$\varepsilon = 1 - \frac{volume\ accupied\ by\ solid}{total\ volume} \tag{2.40}$$

$$\tau = 1 - \frac{actual\ path\ lenght}{point - to - point\ lenght} \tag{2.41}$$

The empirical correlation that Fuller et al. derived to model the diffusion coefficients is as follows [6,14]:

$$D_{ij} = \frac{0.00143.\ T^{1.75}}{p\ M_{ij}^{1/2}\ (v_i^{\frac{1}{3}} + v_j^{\frac{1}{3}})^2} \tag{2.42}$$

$$M_{ij} = \frac{2}{\frac{1}{M_i} + \frac{1}{M_j}} \tag{2.43}$$

v_i and v_j are the atomic diffusion volumes.

In the kinetic theory of gases, the Knudsen diffusion coefficients are identified as [6,14]:

$$D_{kn,ij} = \frac{2}{3}\ d_{pore} \sqrt{\frac{2RT}{\pi M_{ij}}} \tag{2.44}$$

Given the particle diameter (d_p), the pore diameter (d_{pore}) can be calculated as follows:

$$d_{pore} = \frac{2}{3}\frac{\varepsilon}{1-\varepsilon}d_p \tag{2.45}$$

Energy conservation equation

Regarding the species continuity relation, the energy conservation equation defines the thermal balance inside the porous electrodes as [6]:

$$\sum_{i=1}^{n} C_{pi}\rho\, u\, \nabla T \;+\; \nabla.\left(k_{eff}\nabla T\right) \;=\; Q_h \tag{2.46}$$

For each gas phase species and fluid mixture, the specific heat capacity C_{pi} is computed as follows [5, 14]:

$$C_{p,i} = \frac{\sum_{i=1}^{7} a_k \cdot \left(\frac{T}{1000}\right)^k}{M_j} \tag{2.47}$$

$$C_{p,g} = \sum_{i=1}^{n} \omega_i\,.\,C_{p,i} \tag{2.48}$$

where a_k is the species dependent parameter [5,14].

The thermal conductivity k for each species, as well as for the mixture, is described as:

$$k_i = 0.01.\sum_{i=1}^{7} c_k\cdot\left(\frac{T}{1000}\right)^k \tag{2.49}$$

$$k_g = \sum_{i=1}^{n} \omega_i.\,k_i \tag{2.50}$$

where c_k is the species dependent parameter [5,14].

k_{eff} is the effective thermal conductivity in the porous electrodes, k_{eff} can be stated as:

$$k_{eff} = \varepsilon\, k_g + (1-\varepsilon)k_s \tag{2.51}$$

k_g and k_s are the thermal conductivity of gas and solid in the porous electrodes, Q_h refers to the energy source term, which is the heat produced when an electrical current flows through a diffusion layer because of ohmic resistance. It is also known as joule heating [6]:

$$Q_{h,ohm} = \sum \frac{i_s^2}{\sigma_s} \tag{2.52}$$

Conservation of electronic charge

Electric charge is generated as electrons move within the solid phase of the electrode support and diffusion layer. The electric charge conservation is expressed as follows [6]:

$$\nabla . (i_e) = R_c \tag{2.53}$$

Where i_e electronic current density and R_c is the source term. However, given that the diffusion layer does not produce or consume electric charge, equation (2-53) yields

$$\nabla . (i_e) = 0 \tag{2.54}$$

By Ohm's law, the current density vector i_e is connected to the conductivity σ and electrical field V as follows:

$$i_e = \sigma_{eff,s,dl} V \tag{2.55}$$

The voltage V represents a negative gradient of the potential at a given point in the field:

$$V = -\nabla \varphi_s \tag{2.56}$$

So we obtain

$$\nabla . \left(-\sigma_{eff,s,dl} \nabla \varphi_s \right) = 0 \tag{2.57}$$

$\sigma_{eff,s,dl}$ is the effective electronic conductivity described as [6]:

$$\sigma_{eff,s,dl} = \frac{(1-\varepsilon)}{\tau} \sigma_{dl} \tag{2.58}$$

σ_{dl} denotes the electronic conductivity of the porous support and diffusion layers.

4 Electrode reaction model

The areas where the electrochemical reaction takes place, known as electrode reaction layers, are relatively narrow and measure around 20μm.

They are regarded as blended electrodes since they consist of three phases: phase that conducts electrons, phase that conducts ions and pores that allow the reactant gases to permeate [6, 15]. Apart from facilitating electrochemical reactions, they also play a crucial role in transporting reactant gases and their resulting products to and from the electrolyte towards the support and diffusion layers.

Electrochemical reactions, energy transfer, ion and electron transport, and species transport to and from the electrolyte are the processes that require to be modeled within the reaction layers. With the exception of the source term, the governing equations for the processes in the reaction layer are identical to those that have already been evolved for the diffusion layers.

These phenomena in the various sub-models are covered in additional details in the section that follows.

Momentum conservation equation

The equation of momentum in the reaction layer is acquired from the previously determined equations for the support and diffusion layers (equation (2.27)) and be stated as:

$$\frac{1}{\varepsilon_{rl}} \rho(\vec{u}.\nabla)\vec{u} \frac{1}{\varepsilon_{rl}} = = -\vec{u}\frac{\mu}{K_{rl}} + \rho\vec{f} + \nabla.\left(\frac{\mu}{\varepsilon_{rl}}[\nabla\vec{u} + (\nabla\vec{u})^T] - \left[p + \left(\frac{2}{3\varepsilon_{rl}}\mu\right)(\nabla.\vec{u})\right]\vec{I}\right) \quad (2.59)$$

Where ε_{rl} and K_{rl} are the porosity and the permeability of the reaction layers

Species conservation equation

Similar to that identified in the diffusion layer model, the conservation equation controlling the transfer of species in the electrode reaction layers is as follows [6]:

$$\nabla.j_i = R_{ec} \quad (2.60)$$

The rate at which species are consumed or produced as a result of electrochemical reactions is explained by the species source term R_{ec}.

The rate of an electrochemical reaction is related to the volumetric current density by Faraday's law, which states

$$i_v = -nF R_{ec} \quad (2.61)$$

F is the faraday constant, n is the number of electrons transferred.

Assuming that the charge transfer current density is described by Butler-Volmer charge transfer kinetics:

$$i_v = A_{ve} i_0 \left[\exp\left(\frac{n\alpha F\eta_{act}}{RT}\right) - \exp\left(\frac{n(1-\alpha)F\eta_{act}}{RT}\right)\right] \quad (2.62)$$

Where α is the transfer coefficient, A_{ve} is the reactive surface area per unit volume.

The source term of the species resulting from the electrochemical reaction can be represented as

$$R_{ec} = \frac{v_i i_v}{nF} \tag{2.63}$$

Where v_i is the stoichiometric coefficient of the species i in the reaction.

Conservation of electronic charge

Equation (2.54), which is already obtained for the diffusion layer, can be modified to account for the conservation of electronic charge in the electrode reaction layer [6]:

For the anode reaction layer: $\qquad\qquad \nabla.(i_e) = i_{v,a}$ $\qquad\qquad$ (2.64)

For the cathode reaction layer: $\qquad\qquad \nabla.(i_e) = -i_{v,c}$ $\qquad\qquad$ (2.65)

The current density i_e can be represented in terms of the electrical potential applying the Ohm's law relation, making the equations mentioned above:

For the anode reaction layer: $\qquad\qquad \nabla.\left(-\sigma_{eff,s,rl}\,\nabla\varphi_s\right) = i_{v,a}$ $\qquad\qquad$ (2.66)

For the cathode reaction layer: $\qquad\qquad \nabla.\left(-\sigma_{eff,s,rl}\,\nabla\varphi_s\right) = -i_{v,c}$ $\qquad\qquad$ (2.67)

In the reaction layer, $\sigma_{eff,s,rl}$ represents the effective electronic conductivity and it is stated as follows:

$$\sigma_{eff,s,rl} = V_s \frac{(1-\varepsilon)}{\tau}\sigma_{s,rl} \tag{2.68}$$

Where V_s and $\sigma_{s,rl}$ are the volume fraction and the electronic conductivity of the electronic conducting particle respectively.

Conservation of ionic charge

In the reaction layers, the ionic charge can be represented by the following equations, which are analogous to the modeling equations created for electronic charge [6]:

For the anode reaction layer: $\qquad\qquad \nabla.(i_i) = i_{v,a}$ $\qquad\qquad$ (2.69)

For the cathode reaction layer: $\qquad\qquad \nabla.(i_i) = -i_{v,c}$ $\qquad\qquad$ (2.70)

Likewise, the preceding equations become:

For the anode reaction layer:
$$\nabla \cdot \left(-\sigma_{eff,i,rl} \nabla \varphi_i\right) = i_{v,a} \tag{2.71}$$

For the cathode reaction layer.
$$\nabla \cdot \left(-\sigma_{eff,i,rl} \nabla \varphi_i\right) = -i_{v,c} \tag{2.72}$$

In the reaction layer, $\sigma_{eff,i,rl}$ represents the effective ionic conductivity and it is stated as follows:

$$\sigma_{eff,i,rl} = V_{el} \frac{(1-\varepsilon)}{\tau} \sigma_{l,rl} \tag{2.73}$$

Where $\sigma_{l,rl}$ is the electronic conductivity of the ionic conducting particle.

Energy conservation equation

With the eφception of the source term, the electrode reaction layer's energy conservation principle is similar to that previously established in the diffusion layer (equation (2.46)) and is written below presuming local thermal equilibrium exists between the fluid and the porous matrix as [6]

$$\sum_{i=1}^{n} C_{pi} \rho\, u\, \nabla T \ + \ \nabla \cdot \left(k_{eff,rl} \nabla T\right) - \sum_{i=1}^{n} h_i r_i = \ Q_h \tag{2.74}$$

where $k_{eff,rl}$ is the layer's effective thermal conductivity, which is expressed as [16]

$$k_{eff,rl} = \ \varepsilon\, k_g + (1-\varepsilon)[V_s\, k_{el} + (1-V_s)k_{io}] \tag{2.75}$$

Where k_g is the thermal conductivity of gas, V_s is the volume fraction, k_{el} and k_{io} and are the thermal conductivities of the electronic and ionic conducting particles respectively.

$$Q_h = \ Q_{ohm} + \ Q_{(act+conc)} + \ Q_e \tag{2.76}$$

Q_{ohm} indicates the heat generation due to the electronic and ionic ohmic polarization [5,17]:

$$Q_{h,ohm} = \sum \frac{i_s^2}{\sigma_s} + \sum \frac{i_l^2}{\sigma_l} \tag{2.77}$$

where σ_l and σ_s are the ionic/electronic conductivity respectively, the joule heating is produced by ionic and electronic currents flowing through the reaction layer.

Q_e depicts the reversible heat generated owing to the electrochemical reaction [5]:

$$Q_e = -\Delta S_e \frac{T.i_{v,e}}{n.F}$$ (2.78)

ΔS_e is the entropy change for reactions

$Q_{(act+conc)}$ is the irreversible heat generated owing to the electrochemical reactions [3]:

$$Q_{(act+conc)} = i_v \left(\eta_{act} + \eta_{conc} \right)$$ (2.79)

$$Q_h = i_v. \left(-\frac{T \Delta S_e}{n.F} + \eta_{act} + \eta_{conc} \right) + \sum \frac{i^2}{\sigma}$$ (2.80)

5   Electrolyte model

The electrolyte phase is a fully dense solid through which oxide ions (O^{2-}) migrate from the cathodic reaction layer to the anodic reaction layer. This layer models the oxide ion transfer mechanism, which applies charge and energy transfer simultaneously.

Conservation of ionic charge

In the electrolyte layer, the conservation of ionic charge is represented as [6]:

$$\nabla. (i_i) = 0$$ (2.81)

Ohm's law characterizes the current density (i_i) as

$$i_i = \nabla. \left(-\sigma_{i,ele} \nabla\varphi_i \right)$$ (2.82)

Where $\sigma_{i,ele}$ is the ion conductivity of electrolyte, and $\nabla\varphi_i$ is the ionic potential of the electrolyte.

Energy conservation equation

Since there is purely conduction responsible for heat transport in the electrolyte, the layer's energy conservation equation can be written as:

$$\sum_{i=1}^{n} C_{pi}\rho \, u \, \nabla T + \nabla. (k_e \nabla T) = Q_e$$ (2.83)

where the joule heating effect resulting from the resistance of ionic currents passing through the electrolyte is the heat source term and is given by

$$Q_e = \sigma_{i,el} \nabla^2 \varphi_i \tag{2.84}$$

6 Channel model

The flow of reactants and products through the SOFC channels is described by the channel sub model. It is necessary to model the following events in the channels: the movement of species into and out of the electrode diffusion layer; also, the transfer of energy resulting from heat convection and species diffusion:

Mass conservation equation

In the flow channels, the mass conservation equation is written as

$$\nabla.(\rho u) = 0 \tag{2.85}$$

R_i is the mass source.

Momentum conservation equation

For the gaseous substances passing through the channel, the momentum conservation equation can be written as

$$\nabla.(\rho \vec{u}\vec{u}) = -\vec{u}\mu + \rho\vec{f} + \nabla.\left(\mu[\nabla\vec{u} + (\nabla\vec{u})^T] - \left[p + \left(\frac{2}{3}\mu\right)(\nabla.\vec{u})\right]\vec{I}\right) \tag{2.86}$$

Species conservation equation

In the flow channels, species conservation is given by

$$\nabla.(\rho u \nabla \omega_i) + \nabla.j_i = R_i \tag{2.87}$$

Energy conservation equation

The energy conservation in the flow channels is provided by

$$\sum_{i=1}^{n} C_{pi}\rho\, u\, \nabla T + \nabla.\left(k_g \nabla T\right) = Q_e \tag{2.88}$$

Since the reaction sites occur in the electrodes, there is no heat generation within the flow channels, hence the heat sources may be ignored.

7 Interconnect model

The solid layer interconnector, also known as a current collector or bipolar plate, is positioned between individual cells in a stack with the aim of connecting the cells in series to aggregate the electricity generated. Although electrons travel via the interconnectors instead of ions, the events that occur there are comparable to those in the electrolyte. As a result, this model takes into account energy conservation, which explains the joule heating effect brought on by resistance to electron flow, as well as charge conservation, which accounts for charge transfer.

Conservation of electronic charge

In the interconnect layer, the conservation of electronic charge is expressed as

$$\nabla \cdot (i_s) = 0 \tag{2.89}$$

Ohm's law characterizes the current density (i_s) as

$$i_s = \nabla \cdot \left(-\sigma_{s,int} \, \nabla \varphi_e\right) \tag{2.90}$$

$\sigma_{s,int}$ is the electronic conductivity and $\nabla \varnothing_e$ is the electronic potential of the interconnect layer.

Energy conservation equation

Heat transfer by convection and conduction occurs in the interconnect due to the contact with fluids and electrodes. Consequently, the energy conservation equation in the interconnector is as follows:

$$\sum_{i=1}^{n} C_{pi} \rho \, u \, \nabla T \, + \, \nabla \cdot (k_e \nabla T) \, = \, Q_e \tag{2.91}$$

Q_e is the joule heating caused by the resistance of electronic currents passing through the connector, and it is determined by

$$Q_e = \sigma_{s,int} \, \nabla^2 \varphi_e \tag{2.92}$$

8 Boundary and interfacial conditions

In order to provide reliable results from the model calculations, the boundary conditions must be defined.

Flow in gas channels and electrodes

The gas inlet velocities are regarded as laminar flow profiles, the velocity of the air at the cathode is much higher compared to the velocity of the fuel (hydrogen), this is due to the fact that the oxidation of hydrogen is fast compared with the reduction of oxygen.

In the current simulation, the air and hydrogen inlet velocities are 3 m/s and 0.5 m/s.

$$U = U_{in} \tag{2.93}$$

The outlet boundary condition is set to the atmospheric pressure, with no viscous stress.

$$p = p_0 \tag{2.94}$$

At the walls, a no slip boundary condition is assumed.

$$U = 0 \tag{2.95}$$

Mass Transfer in the channels and electrodes

Both the fluids at inlet are regarded as humidified hydrogen mixture (90% hydrogen and 10% water) at the anode and air inlet consisting of oxygen and nitrogen flows through the air channel.

$$\omega_{H_2} \, at \, inlet = \, \omega_{H_2,in} \tag{2.96}$$

$$\omega_{O_2} \, at \, inlet = \, \omega_{O_2,in} \tag{2.97}$$

The outlets are considered as convective fluxes.

At the interface between the reaction layer and the diffusion layer, continuous flux species is assumed.

$$(n.j)| \, dl = \, (n.j)| \, rl \tag{2.98}$$

No flux set at the walls of the channels and at the interface electrolyte / electrode reaction layers.

$$(n.j)|_{\partial\Omega_{wall}} = 0 \tag{2.99}$$

$$(n.j) = 0 \tag{2.100}$$

Thermal boundary conditions

At the flow channel inlet, the fuel temperature is taken as 1000 K

$$T = T_0 \tag{2.101}$$

The side walls are considered to be adiabatic since it is predicted that there are parallel channels with periodic conditions

Whereas convection predominates in gas channels, conduction predominates in solid materials.

At the interfaces between the channels flow and the interconnector, the heat flux is defined as:

$$n.Q = h\left(T_{in} - T_{gas}\right) \tag{2.102}$$

While, the heat flux is continuous across the interface electrode diffusion layer-electrode reaction layer, and the interface electrode reaction layer- electrolyte, these are expressed mathematically as

$$(n.Q)|\, dl = (n.Q)|rl \tag{2.103}$$

$$(n.Q)|\, dl = (n.Q)|\, int \tag{2.104}$$

Charge transport boundary condition

In fuel cell, the anode and cathode current collectors allow electrons to flow through to the external electric circuit. At the anode side, the electrode voltage is set as 0V (ground boundary), whereas at the cathode side, the electrode voltage is adapted as the cell voltage (in this study, Vcell=0.7 V). The following are the boundary conditions for the electric field:

(anode) $$\varphi_{elec} = 0 \tag{2.105}$$

(cathode) $$\varphi_{elec} = Vcell \tag{2.106}$$

There are no current collectors that allow ions to transfer in the ionic field.

The internal boundaries of the diffusion layer and reaction layer, as well as the diffusion layer and interconnector, show a continuous flow for the electric potential inside their respective boundary conditions, while an insulated boundary condition is maintained for the ionic potential across these interfaces

$$(n.i_s)|\, dl = (n.i_s)|rl \tag{2.107}$$

$$(n.i_s)|\, dl = (n.i_s)|int \tag{2.108}$$

$$(n.i_i)|\ dl\ =\ 0 \tag{2.109}$$

At the junction of the reaction and diffusion layers, the electronic current density is insulated at this boundary, and the ionic current density is considered continuous:

$$(n.i_e)|\ rl\ =\ 0 \tag{2.110}$$

$$(n.i_i)|\ rl\ =\ (n.i_i)|ele \tag{2.111}$$

The external boundaries of components surfaces of SOFC are insulated.

9   Numerical solution

The formulation of the governing and constitutive equations in fuel cell modeling necessitates certain mathematical tools in addition to an in-depth knowledge of the chemical and physical processes. It is quite challenging to find analytically precise solutions to these equations due to their considerable nonlinearity.

This chapter defines the finite element method (FEM), a computational methodology that subdivides the physical area into tinier finite element dimensions named finite elements. It is used to acquire the solutions of the governing equations established in our study.

Every element is given a variety of characteristic equations, which are resolved concurrently to predict the behavior of the cells.

The following steps are involved to resolve a problem using finite elements:

1- Dividing the specified domain into an ensemble of finite elements

2- Formulation of element equations for every element within the mesh.

3- Combining elemental equations to generate the overall equations for the entire problem

4- imposing the problem's boundary conditions

5- Solving the assembly equations

6- Post-processing of the solutions

10 COMSOL Multiphysics to develop and solve the SOFC model

The finite element approach was utilized to discretize the governing equations and the boundary conditions in this model. The commercial software program COMSOL Multiphysics (version 5.3a), was employed to solve the problem for a tree-dimensional SOFC system including a non-linear set of algebraic and differential equations. The constitutive relations and governing equations of the model were resolved under stationary conditions.

The following explains the primary steps involved in building the model:

Creating the SOFC Geometry

Three-dimensional schematic of planar SOFC was formed. The created geometry is divided into sub-domains, each of that represents a different SOFC component and attributes the governing equations that depict the domain's physical behavior.

Specifying the governing equations

It is possible to load user-defined equations and relations into COMSOL as dependent operator expressions for variables or as scalar operator expressions for parameters.

Specifying the boundary conditions

The model specifies the boundary conditions and initial values for each factor.

Constructing the mesh

In order to precisely solve the problem, the mesh allows the model geometry to be discretized into smaller bits known as mesh elements. In this study, the grid independence was achieved at 192800 meshing elements and the solution tolerance is defined to 0.001 for each segregated group. The mesh configuration is shown in Figure 2.3.
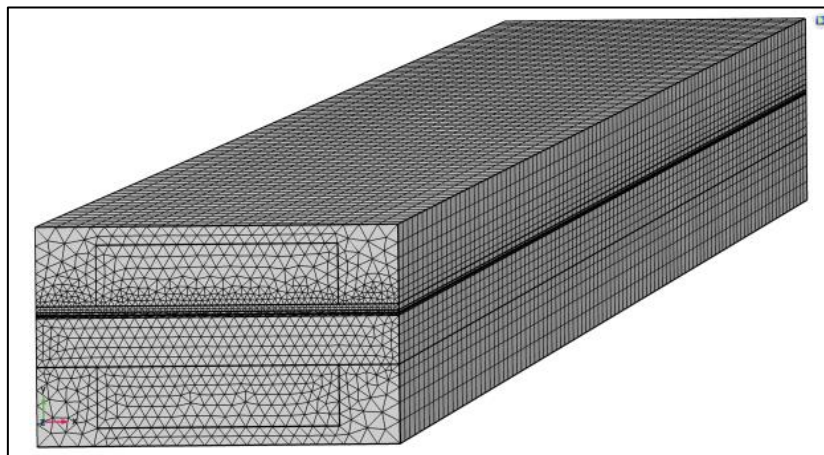
Figure 2. 3. Mesh illustration

A 2D surface mesh at the inlet of the SOFC is generated and further sweeps along the gas channel direction to reach 3D. Three different meshes are used to investigate the impact of mesh density on the performance of the SOFC model, e.g., 121464, 192800, et 262208. The H_2 mole concentration distribution along the centerline of the anode is plotted against different cell numbers in Figure 2.4.

The H_2 mole concentration decreases from the fuel inlet to the outlet, which indicates consumption. The inlet mole concentration is about 14.5 mol/m^3 which is almost the same for

all meshes. The mole concentration is about 6.43 mol/m^3 for mesh numbers of 121464 at the outlet. When increasing the mesh to 192800 and 262208, the outlet mole fraction reaches the same value, e.g., 6.06 mol/m^3.

 This means that the mesh is accurate enough to evaluate the performance of SOFC and thus a mesh with the number of 192800 cells is used in the parameter studies performed in this paper.
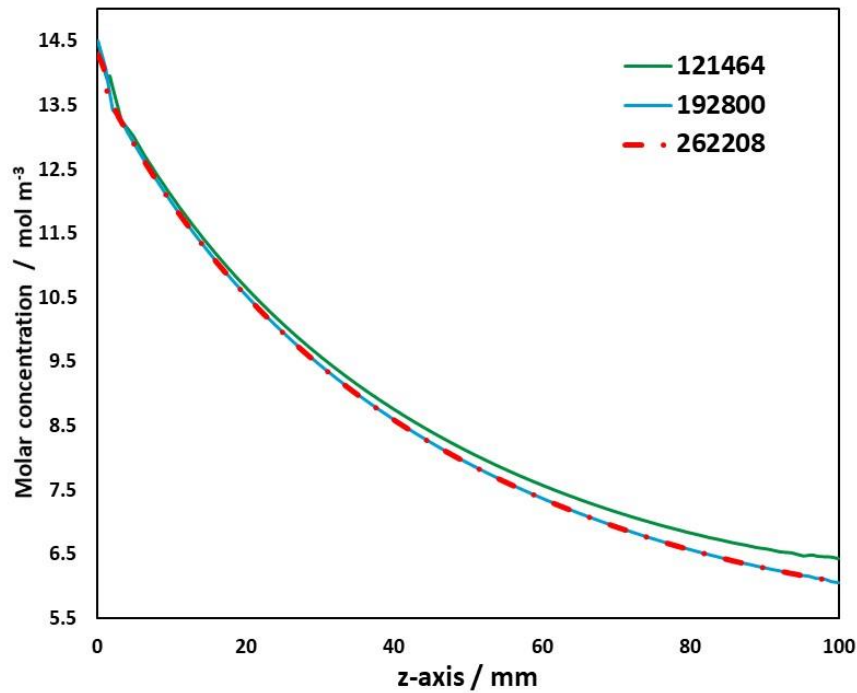
Figure 2. 4. Mesh independency investigation

Creating study to solve the model

Depending on how the problem behaves, users of the COMSOL software can choose from a variety of study kinds. The most popular types of studies are the "time dependent study," which is utilized for transient simulations, and the "stationary study," which is used for steady state scenarios. A stationary study got selected for this SOFC model.

Creating results

Using programs like Excel, Origin, and Hysys, the simulated model file's data were utilized for the post processing phases.

Depending on the model's complexity, the simulation requires one to six hours to reach the solution.

11 Conclusion

This chapter presents the governing equations that are used to predict the chemical and physical processes in the SOFC. In order to make simulations easier, these equations involve the conservation of mass, momentum, species, energy, electronic and ionic charge.

The overall SOFC model comprised different components: flow channels for fluid and air, electrode diffusion layer, electrode support layer, electrode reaction layer, electrolyte and interconnector.

In addition, the thermophysical parameters and boundary conditions of the model are displayed.

References

[1] Tchakalov, R. Engineering and optimization of electrode/electrolyte interfaces to increase solid oxide fuel cell (SOFC) performances (Doctoral dissertation, Université Paris sciences et lettres), 2021.

[2] Mohammed, H., Al-Othman, A., Nancarrow, P., Tawalbeh, M., & Assad, M. E. H. (2019). Direct hydrocarbon fuel cells: A promising technology for improving energy efficiency. Energy, 2019 ; 172, 207-219.

[3] Zhang, X., Espinoza, M., Li, T., & Andersson, M. (2021). Parametric study for electrode microstructure influence on SOFC performance. International Journal of Hydrogen Energy, 2021 ; 46(75), 37440-37459.

[4] Camprubı, M. G. Multiphysics models for the simulation of solid oxide fuel cells (Doctoral dissertation, Universidad de Zaragoza), 2011.

[5] Andersson, M. Sofc modeling considering mass and heat transfer, fluid flow with internal reforming reactions;2009.

[6] Ighodaro, O. O. Modelling and simulation of intermediate temperature solid oxide fuel cells and their integration in hybrid gas turbine plants (Doctoral dissertation, Newcastle University), 2016

[7] Modeling with electrochemistry. COMSOL multyphisics version 55, batteries and fuel cells module users guide, chapter 2: modeling with electrochemistry, Stockholm, Sweden. 2019.

[8] Suwanwarangkul, R., Croiset, E., Fowler, M. W., Douglas, P. L., Entchev, E., & Douglas, M. A. Performance comparison of Fick's, dusty-gas and Stefan–Maxwell models to predict the concentration overpotential of a SOFC anode. Journal of Power Sources, 2003; 122(1), 9-18.

[9] Curtiss, C. F., & Bird, R. B. (1999). Multicomponent diffusion. Industrial & Engineering Chemistry Research,1999; 38(7), 2515-2522.

[10] Campanari, S., & Iora, P. (2004). Definition and sensitivity analysis of a finite volume SOFC model for a tubular cell geometry. Journal of Power Sources, 2004 ; 132(1-2), 113-126.

[11] Iwata, M., et al., Performance analysis of planar-type unit SOFC considering current and temperature distributions. Solid State Ionics, 2000. 132(3–4): p. 297-308.

[12] Ngo, N.D. and K.K. Tamma, Microscale permeability predictions of porous fibrous media. International Journal of Heat and Mass Transfer, 2001. 44(16): p. 3135-3145.

[13] Litster, S. and N. Djilali, Two-phase transport in porous gas diffusion electrode, in Transport phenomena in fuel cells, B. Sunden and M. Faghri, Editors. 2005, WIT press: Southampton. p. 175-213.

[14] Todd, B. and J.B. Young, Thermodynamic and transport properties of gases for use in solid oxide fuel cell modelling. Journal of Power Sources, 2002. 110(1): p. 186-200.

[15]. Farhad, S. and F. Hamdullahpur, Micro-modeling of porous composite anodes for solid oxide fuel cells. Aiche Journal, 2012. 58(6): p. 1893-1906.

[16] Hussain, M.M., X. Li, and I. Dincer, Mathematical modeling of planar solid oxide fuel cells. Journal of Power Sources, 2006. 161(2): p. 1012-1022

[17] Hajimolana, S. A., Hussain, M. A., Daud, W. A. W., Soroush, M., & Shamiri, A. (2011). Mathematical modeling of solid oxide fuel cells: A review. Renewable and sustainable energy reviews, 2011; 15(4), 1893-1917.

Chapter 3: Numerical study of electrode permeability influence on planar SOFC performance

1   Introduction

In this chapter, we introduce a three-dimensional numerical model designed to investigate how various thermophysical and morphological parameters affect the performance of a Solid Oxide Fuel Cell (SOFC). We specifically examine how changes in electrode permeability impact fuel distribution, ionic and electric current density, pressure, and diffusion flux. Through a detailed parametric study of the ionic and electronic phase volume fraction within the electrodes, we find that current density increases with decreasing permeability up to a certain point, but then decreases with excessively low permeability. Our analysis reveals significant effects of pressure and species diffusion on cell performance as permeability varies. Notably, altering permeability in the electrode's active layer significantly influences current density, closely related to the ionic phase volume fraction. This study enhances our understanding of the interplay between SOFC performance and microstructure, offering valuable insights for optimizing electrode permeability design.

2   Theoretical Approach

2.1   Numerical Model

2.1.1   Geometry

The three-dimensional numerical model of a hydrogen-fueled SOFC unit has been developed. Figure 3.1 shows the schematic of the simulated fuel cell unit, consisting of active cathode and anode layers (AFL/CFL), supporting anode layer (ASL), cathode diffusion layer (CDL), electrolyte and interconnectors, dividing the total cell into seven zones. The material is Ni for ASL, Ni-8YSZ for AFL, dense 8YSZ for electrolyte, LSM for CDL, and LSM-8YSZ composite for CFL [1]. The model has been developed and implemented in the commercial software COMSOL Multiphysics (version 5.3). The geometry parameters are shown in Table 3.1.
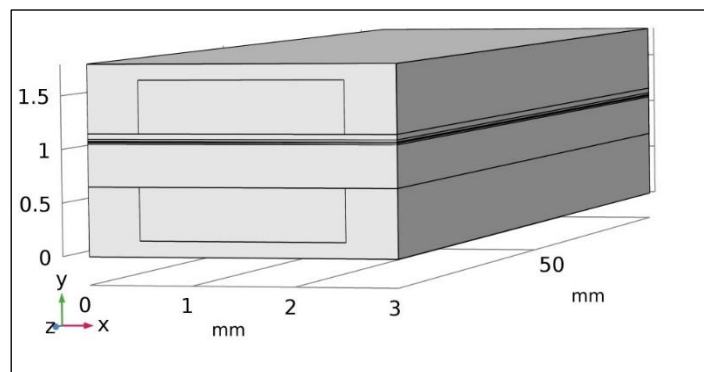

Figure 3. 1. Schematic of the single-channel SOFC model

Tableau 3. 1. Geometry size of the single cell SOFC [2, 3]

	Height- y [10^{-6}] / m	Depth-x [10^{-3}] / m
Gas channel	500	2
Interconnects ribs		0.5
Interconnects	650	3
Anode support layer	400	
Anode active layer	15	
Electrolyte	10	
Cathode active layer	20	
Cathode diffusion layer	50	

The assumptions applied are the following: the SOFC operates at steady-state conditions, flow conditions are established laminar and incompressible in the channels, the involved gases in both channels are assumed to behave as ideal gases, the ionic and electronic conductors are considered to be isotropic and homogenous, gas leakage and radiation heat transfers are neglected.

The equation for momentum, mass, electron, ion, and heat transport have been simultaneously solved, as described in the following section.

2.1.2 Governing Equations

Two basic reactions occurring in anode and cathode are considered, as the cell has been simulated in the operation with humidified hydrogen at the anode and air at the cathode.

At the cathode, oxygen is reduced to ionic form by electrons as follows:

$$\frac{1}{2}O_2 + 2e^- \Leftrightarrow O^{2-} \tag{3.1}$$

At the anode, hydrogen is adsorbed on the Ni surface at the TPB; the oxygen ion, passing through the electrolyte, reacts with hydrogen at the anode active layer (AFL).

The reaction results in two electrons and steam.

$$H_2 + O^{2-} \Leftrightarrow H_2O + 2e^- \tag{3.2}$$
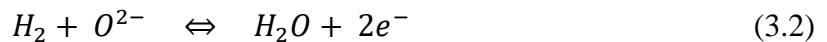
And the overall reaction is given by:

$$H_2 + \frac{1}{2}O_2 \Leftrightarrow H_2O \tag{3.3}$$

Ion and electron transport are considered in order to solve charge conservation equation. Ohm's law is employed for charge balances.

Ionic and Electronic transport

The operating cell voltage is the potential difference between the cathode and the anode current collectors. The governing equations for the ion and electron transport are defined as [3]:

$$\begin{cases} \nabla . i_l = i_v \\ \\ i_l = -\sigma_{eff,l} \nabla \varphi_l \end{cases} \tag{3.4}$$

$$\begin{cases} \nabla . i_s = i_v \\ \\ i_s = -\sigma_{eff,s} \nabla \varphi_s \end{cases} \tag{3.5}$$

where φ_l and φ_s are the ionic and the electronic potential respectively, i_v is the volumetric current density obtained from the Butler-Volmer equation, i_l and i_s are the charge fluxes for ions and electrons and $\sigma_{eff,l}$ and $\sigma_{eff,s}$ are the effective ion and electron conductivities.

Electrochemical model

Due to various polarizations and internal resistance, the working voltage (E) drops compared to the open circuit voltage, and it is expressed as [4]:

$$V = E^{ocv} - \eta_{act} - \eta_{ohm} - \eta_{conc} \tag{3.6}$$

Where E^{ocv} means the open circuit voltage, the activation polarizations η_{act} reflecting the loss caused by the electrochemical reactions at the electrodes are defined as:

$$\eta_{act,a} = \varphi_s - \varphi_l - E_{eq,a} \tag{3.7}$$

$$\eta_{act,c} = \varphi_s - \varphi_l - E_{eq,c} \tag{3.8}$$

Ohmic loss (η_{ohm}) occurs because of the resistance to the flow of ions in the electrolyte and the electrical resistance of materials to the flow of electrons:

$$\eta_{ohm} = i . R_{tot} \tag{3.9}$$

Here R_{tot} is the total internal resistance in the cell. The concentration polarization η_{conc} are calculated by [5]:

$$\eta_{conc,a} = \frac{R.T}{n_a.F} \ln \left(\frac{P_{H_2O,TPB} . P_{H_2,b}}{P_{H_2,TPB} . P_{H_2O,b}} \right) \tag{3.10}$$

$$\eta_{conc,c} = \frac{R.T}{n_c.F} \ln \left(\frac{P_{O_2,b}}{P_{O_2,TPB}} \right) \tag{3.11}$$

Where the index TPB stands for the three-phase boundary, and b for the boundary between the gas channel and the electrode. When an hydrogen-water steam mixture is used as fuel, then the equilibrium potential for cathode and anode is calculated by Nernst equation [1]:

$$E_{eq,H_2} \ = \ \frac{R.T}{2.F} \ ln \ \frac{P_{H_2}}{P_{H_2O}} \tag{3.12}$$

$$E_{eq,O_2} \ = \ E_{H_2/O_2}^0 \ + \ \frac{R.T}{4.F} \ ln \ (\frac{P_{O_2}}{P_{O_2,ref}})^{\frac{1}{2}} \tag{3.13}$$

Where the reversible voltage E_{H_2/O_2}^0 is defined as [1]:

$$E_{H_2/O_2}^0 = 1.253 - 2.4516 \ .10^{-4} \times T \tag{3.14}$$

The current density (i_v) can be obtained through the Butler-Volmer equation:

$$i_v \ = \ Ave \ .i_0 \ [\exp\left(\frac{n\alpha F\eta_{act}}{RT}\right) - \exp\left(\frac{n(1-\alpha)F\eta_{act}}{RT}\right) \tag{3.15}$$

Where i_0 is the exchange current density, F is the Faraday constant, α is the charge transfer coefficient, n is the number of electrons transferred per electrochemical reaction and *Ave* is the electrochemical active area of corresponding electrode.

The exchange current density, i_0 , refers to the rate that reduced and oxidized species transfer electrons with the electrode, and defined as [1]:

$$i_{0,a} \ = \ \gamma_a \ (\frac{P_{H_2}}{P_{H_2,ref}})^A \ (\frac{P_{H2O}}{P_{H_2O,ref}})^B \ \exp(\frac{-E_a}{RT}) \tag{3.16}$$

$$i_{0,c} \ = \ \gamma_c \ (\frac{P_{O_2}}{P_{O_2,ref}})^C \ \exp(\frac{-E_c}{RT}) \tag{3.17}$$

Where γ_a and γ_c are the exponential factor for anode and cathode, E_a and E_c are the activation energy for anode and cathode, $p_{i,ref}$ and p_i are the reference partial pressures and partial pressure for species i. A=0.41, B=0.4 and C= 0.3 are concentration-dependent exponential coefficients.

Momentum transfer
The gases flow in the air and fuel channels equation are solved using the Navier-Stokes equation [1]:

$$\rho(u.\nabla)u = \ \nabla \ [-pI + \ \mu(\nabla u + (\nabla u)^T) \ -\frac{2}{3} \ \mu \ (\nabla.u)I)] \tag{3.18}$$

Where u is the velocity vector, ρ is the density, p is the pressure, I is the unit matrix and μ is the dynamic viscosity. The continuity equation is as follows:

$$\nabla.(\rho u) = 0 \tag{3.19}$$

For the governing equation of momentum conservation in porous electrodes, the continuity equation and the Brinkman equations are used:

$$\nabla.(\rho u) = Q_m \tag{3.20}$$

$$\frac{1}{\varepsilon}\rho(u.\nabla)u\frac{1}{\varepsilon} = \nabla\left[-pI + \mu(\nabla u + (\nabla u)^T) - \frac{2}{3}\mu(\nabla.u)I\right] - \left(\mu K^{-1} + \frac{Q_m}{\varepsilon^2}\right)u \tag{3.21}$$

Where ε is the porosity, k represents the permeability, and Q_m is the mass source, which is applied in the active layer of electrode:

$$Q_m = \sum_i \frac{v_i\, i_v}{n_e F}\, M_i \tag{3.22}$$

Where v_i is the stoichiometric coefficient for species i, i_v is the volumetric current density for the electrochemical reaction, n_e is the number of participating electrons in the electrochemical reaction.

Mass transfer

Considering a reacting flow involving a mixture, for the species i, the mass transport through gas diffusion and reactive layers in a fuel cell is given by references [1,3-9]:

$$\rho(u.\nabla)\omega_i = -\nabla.j_i + R_i \tag{3.23}$$

Where ω_i is the mass fraction, R_i is the mass source term, and j_i is the mass flux vector:

$$j_i = -\rho\,\omega_i \sum_j D_{ij}^{eff} d_j \tag{3.24}$$

In equation (25) D_{ij}^{eff} represents the effective diffusion coefficient of species i and d_j is the diffusional driving force of the species j.

$$D_{ij}^{eff} = \frac{\varepsilon}{\tau}\cdot\left(\frac{D_{ij}.D_{k,ij}}{D_{ij}+D_{k,ij}}\right) \tag{3.25}$$

$$D_{k,ij} = \frac{2}{3}\,r_e\sqrt{\frac{8.R.T}{\pi.M_{ij}}} \tag{3.26}$$

$$M_{ij} = \frac{2}{\frac{1}{M_i}+\frac{1}{M_j}} \tag{3.27}$$

$$D_{ij} = \frac{0.00143.\,T^{1.75}}{p\,M_{ij}^{1/2}\,(v_i^{\frac{1}{3}}+v_i^{\frac{1}{3}})^2} \tag{3.28}$$

$$d_j = \nabla x_j + \frac{1}{p}\left[(x_j - \omega_j)\nabla_p\right] \tag{3.29}$$

Where $D_{k,ij}$ is the Knudsen diffusion coefficient, D_{ij} is the binary diffusivity coefficient and r_e is the average pore radius, and x_j is the mole fraction of species j.

Heat transport

SOFC have the most elevated working temperature, as high as 1,000 K, among of all types of fuel cells. In this study, the local thermal equilibrium is used, therefore the temperature T is assumed to be locally the same for both fluid and solid phase.

The governing equation for energy distribution is [1,3-9]:

$$\rho\, C_p u.\nabla T + \nabla.\left(k_{eff}\nabla T\right) = Q_h \tag{3.30}$$

The effective thermal conductivity in the porous electrodes k_{eff} can be expressed as:

$$k_{eff} = \varepsilon\, k_g + (1 - \varepsilon)k_s \tag{3.31}$$

Where k_s and k_g are the thermal conductivity of solid and gas.

The heat sources because of the activation, the ohmic and the concentration polarization, and the charge of entropy in electrochemical reaction are calculated as:

$$Q_h = i.\left(-\frac{T\,\Delta S_r}{n_e.F} + \eta_{act} + \eta_{conc}\right) + \Sigma\frac{i^2}{\sigma} \tag{3.32}$$

Where ΔS_r is the entropy change for reactions (1) and (2). σ denotes the conductivity for specific material:

$$(\text{anode}) \quad \sigma_{Ni} = \frac{9.5\times10^7}{T}\, \exp\left(\frac{-1150}{T}\right)\ [10] \tag{3.33}$$

$$(\text{cathode}) \quad \sigma_{YSZ} = \frac{4.2\times10^7}{T}\, \exp\left(\frac{-1200}{T}\right)\ [10] \tag{3.34}$$

$$(\text{electrolyte}) \quad \sigma_{LSM} = 3.34 \times 10^4\, \exp\left(\frac{-10300}{T}\right)\ [10] \tag{3.35}$$

The conductivity will affect the electronic and ionic transport path due to the composition and microstructure of porous electrodes. Therefore, the effective conductivity is corrected as:

$$\sigma_{eff,a,s} = \sigma_{Ni}.\frac{V_{Ni,a}}{\tau_{s,a}} \tag{3.36}$$

$$\sigma_{eff,el,l} = \sigma_{YSZ}.\frac{V_{YSZ,el}}{\tau_{l,el}} \tag{3.37}$$

$$\sigma_{eff,c,s} = \sigma_{LSM}.\frac{V_{LSM,c}}{\tau_{s,c}} \tag{3.38}$$

Where V is the volume fraction for ion conductivity and electron conductivity of the solid phase, and τ is the tortuosity factor.

2.1.3 Solution method

The governing equations with the appropriate boundary conditions are numerically solved in Comsol Multiphysics 5.3, using a stationary segregated solver with direct (MUMPS) linear solver system. The system of equations is segregated in 5 steps: 1- velocity distribution and pressure field for anode and cathode, 2- temperature distribution, 3- ion and electron distribution, 4- Mass fraction distribution on the air side (O_2 / N_2), 5- Mass fraction distribution on the fuel side (H_2 / H_2O).

The physical parameters used in the model are listed in Table 3.2 and Table 3.3.

The grid independence was achieved at 192,800 meshing elements and the solution tolerance is defined to 0.001 for each segregated group.

Tableau 3. 2. Material properties [1,5]

Parameter	Value	Units
Anode thermal conductivity	11	W m^{-1} K^{-1}
Cathode thermal conductivity	6	W m^{-1} K^{-1}
Interconnect thermal conductivity	44.5	W m^{-1} K^{-1}
Electrolyte thermal conductivity	2.7	W m^{-1} K^{-1}
Anode specific heat	450	J kg^{-1} K^{-1}
Cathode specific heat	430	J kg^{-1} K^{-1}
Interconnect specific heat	475	J kg^{-1} K^{-1}
Electrolyte heat	470	J kg^{-1} K^{-1}
AFL/ CFL density	3,310	kg m^{-3}
ASL density	3,030	kg m^{-3}
CDL density	3,300	kg m^{-3}
Interconnect density	7,850	kg m^{-3}
Electrolyte density	5,160	kg m^{-3}

Tableau 3. 3. Microstructure parameters [1]

Layer	ASL	AFL	CDL	CFL
Porosity	0.44	0.3	0.44	0.3
Electronic phase volume fraction	0.56	0.28 (0.2:0.025:0.35)	0.56	0.28 (0.2:0.025:0.35)
Ionic phase volume fraction	-	0.42 (0.35:0.025:0.5)	-	0.42 (0.35:0.025:0.5)
tortuosity	10	10	10	10
Permeability /m²	1.73x 10^{-11}	1.73x 10^{-11}	1.73x 10^{-11}	1.73x 10^{-11}
Activation energy / KJ mol^{-1}	-	62	130	-
Exponential factor / A m^{-2}	-	3,500	3.3x 10^5	-
Specefic surface area / 1 m^{-1}	-	1.03x10^5	1.03x10^6	-
Electron number	-	2	4	-

2.1.4 Case study

The study has been developed assuming a standard case with permeability of $k=1.73\text{x }10^{-11}$ m² in the electrode layers.

Different control cases have been simulated in which the permeability is changed in the AFL (anode active layer), CFL (cathode active layer), ASL (anode support layer), and CDL (cathode diffusion layer). For each control case, parametric sweep cases are examined to determine the effect of microstructure parameters on the performance of the SOFC.

To visualize the impact of different permeabilities on the distribution fields of fuels and current density at the interface anode-electrolyte, 5 controlled cases are used. Notice that the permeabilities are changed, and in each case they have the same value in all domains of the porous medium as described in Table 3.4.

Based on the 5 cases, two parametric sweep groups are implemented. The active layer of electrodes in each case is kept constant and only the support layer and diffusion layer are varied gradually. The first parametric sweep is for the electronic phase volume reaction of AFL (V_{Ni}) and CFL (V_{LSM}), and the second parametric sweep is for the ionic volume fraction of AFL and CFL (V_{YSZ}) as described in Table 3.3 (sweep range in parenthesis) and Table 3.5.

Tableau 3. 4. Control cases for different permeabilities

Control cases	Value of permeability "k " / m² in the porous media (AFL, CFL, ASL, CDL)
Case 1	$1.73\text{x }10^{-9}$
Case 2	$1.73\text{x }10^{-10}$
Case 3	$1.73\text{x }10^{-11}$
Case 4	$1.73\text{x }10^{-12}$
Case 5	$1.73\text{x }10^{-13}$

Tableau 3. 5. Parametric sweep for different permeabilities

Control cases	"k " / m² at AFL , CFL	"k " / m² at ASL, CDL
Case 1	$1.73\text{x }10^{-9}$	$(1.73\text{x}10^{-9}; 1.73\text{x}10^{-13})$
Case 2	$1.73\text{x }10^{-10}$	$(1.73\text{x}10^{-9}; 1.73\text{x}10^{-13})$
Case 3	$1.73\text{x }10^{-11}$	$(1.73\text{x}10^{-9}; 1.73\text{x}10^{-13})$
Case 4	$1.73\text{x }10^{-12}$	$(1.73\text{x}10^{-9}; 1.73\text{x}10^{-13})$
Case 5	$1.73\text{x }10^{-13}$	$(1.73\text{x}10^{-9}; 1.73\text{x}10^{-13})$

2.1.5 Boundary conditions

The gas inlet velocities are regarded as laminar flow profiles, humidified hydrogen mixture inlet (90% hydrogen and 10% water) at the anode and air inlet consisting of oxygen and nitrogen flows through the air channel.

The boundary conditions at the outlets are defined as convective flux, where the pressures are sat as atmospheric pressure (1 atm). No-slip condition is applied at the walls.

The inlet gas temperature is delineated by the operating temperature (1,000 K) and the definition of the outlets is a convective flux. Symmetry is characterized at the bottom and the top of the cell walls. Regarding the electrical potential boundary condition, the cell potential on the surface of interconnect in the cathode side is fixed as the cell operating voltage (0.7 V), while the cell potential on the anode side is set to zero.

More detailed operating conditions are summarized in Table 3.6.

Tableau 3. 6. Operating conditions [1]

Inlet temperature / K	1,000
Operating pressure / atm	1
Operating voltage / V	0.7
Fuel velocity inlet / m s^{-1}	0.5
Air velocity inlet / m s^{-1}	3
Fuel inlet composition x_{H_2} , x_{H_2O}	0.9 ; 0.1
Air inlet composition x_{O_2} , x_{N_2}	0.21 ; 0.79

3 Results and Discussion

3.1 Model Validation

In order to show the model in this study can handle the cell performance of a SOFC, the present model is developed for the same experimental conditions reported by Fu et al. [11]. The validation model simplifies the SOFC stack customized by Ningbo SOFCMAN Company (China), into a single model for performance investigation.

For the experiments, the fuel and air inlet flow rates are 16 NmL min^{-1} cm^{-2} and 80 NmL min^{-1} cm^{-2} respectively at 800 °C for the SOFC stacks with conventional straight channel interconnectors (SCIs). The model performs at atmospheric pressure and ignores the thermal radiation.

Figure 3.2 shows the cell voltage versus current density curve acquired from the numerical modeling, compared with that obtained from experimental data. This validation result indicates a good agreement between the simulation and experimental results, the maximum error is less than 5%
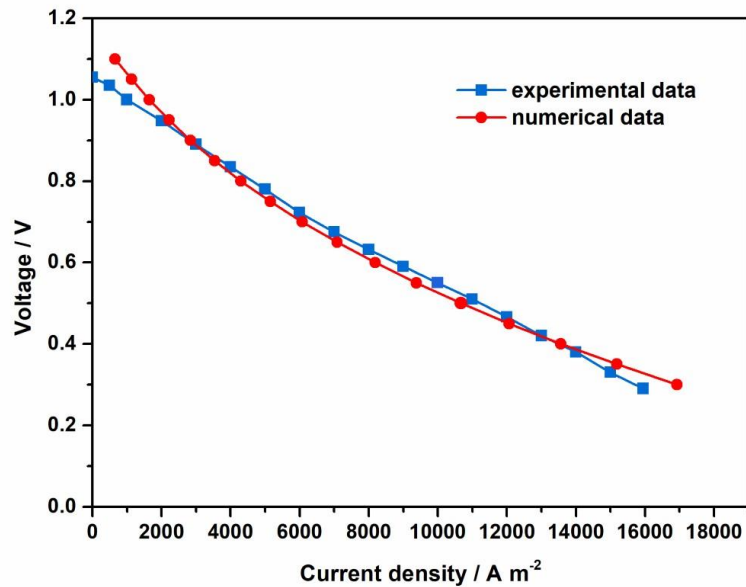

Figure 3. 2. Comparison of Numerical and experimental polarization curves for the SOFC

3.2 Species Transport

Figure 3.3a presents the 3D variation of mass fraction of hydrogen along the anode flow channel as well as in the anode itself for the standard case. The mass fraction of hydrogen gradually reduces from the initial set value of 0.9 to about 0.2 at the outlet, as moving along the main flow direction, due to the diffusion process through the porous electrode and its oxidation at the anode electrolyte interface.

The hydrogen mass fraction decreases from the channel towards the active anode layers in vertical direction, and decreases also with important variation in the x direction under the interconnect ribs. This is due to the mass flow resistance of the porous anode structure where the electrochemical reactions take place.
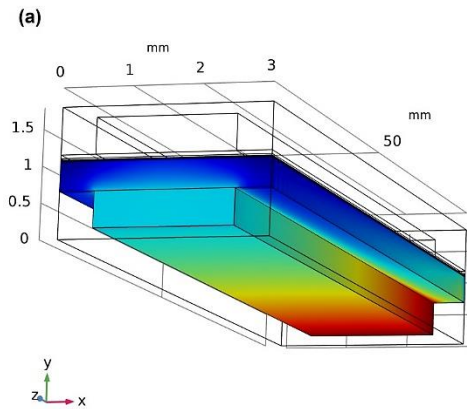
Figure 3. 3.a : Hydrogen mass fraction distribution for 0.7 V cell voltage
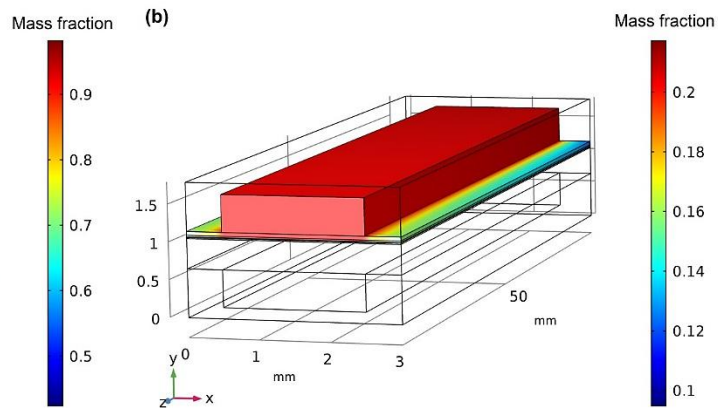
Figure 3.3-b: Oxygen mass fraction distribution for 0.7 V cell voltage

The distribution of oxygen mass fraction within the cathode side is presented in Figure 3.3b for the standard case. In the air flow direction, the mass fraction of oxygen is reduced due to the diffusion of oxygen through the porous electrode and its reduction in the electrochemical reaction at the cathode electrolyte interface from its initial value 0.21 to 0.18.

Furthermore, very low oxygen mass fraction can be observed in the x direction under the interconnect ribs, which signifies that oxygen is importantly consumed in this zone. In addition, it faces diffusion problems because of the ribs.

Figure 3.4 presents the hydrogen mass fraction distribution of the x-y plane (2D) along the interface between anode and electrolyte (IAE) for different permeabilities. It should be noted that the color scale in this figure is maintained similar for convenient comparison.

Generally, the hydrogen distribution profiles are similar in all cases. It can be seen that the highest mass is observed at the fuel inlet, and it reduces along the fuel channel direction especially under the ribs of interconnects.

In case of the highest permeability (case 1: k= 1.76x10^{-9} m²), molecules of hydrogen are more distributed at the anode diffusion layer, compared to the other cases (2,3,4 and 5). This case shows also larger distribution of hydrogen at x=0. This result owing to the fact that a high permeability allows molecules easily pass through porous media, that being so the diffusion of species increases when the electrode permeability decreases.

In addition, the highest value of mass fraction is marked at the first case (0.863) and diminishes with the lowering of permeability as shown in the following cases which ranges between 0.828 (case 2) and 0.822 (case 5). This figure reveals that reducing the permeability in both support and active layers has an impact on the distribution of fuel at the IAE.
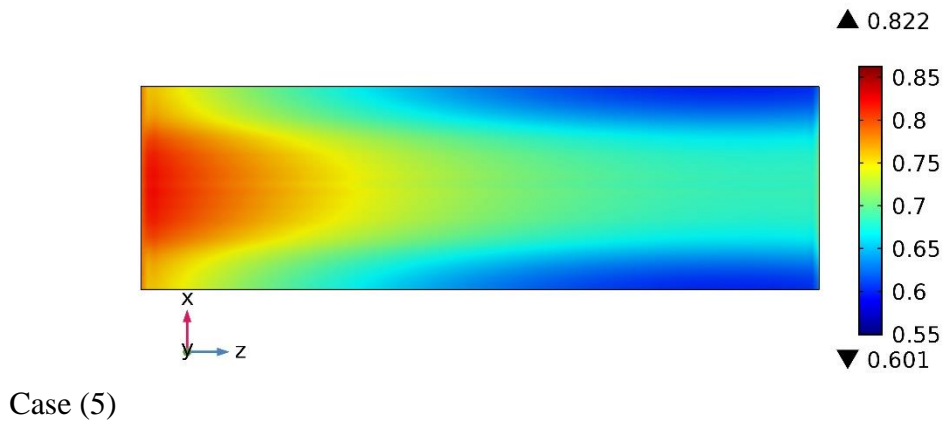
Case (1)

Case (2)

Case (3)

Case (4)

Case (5)
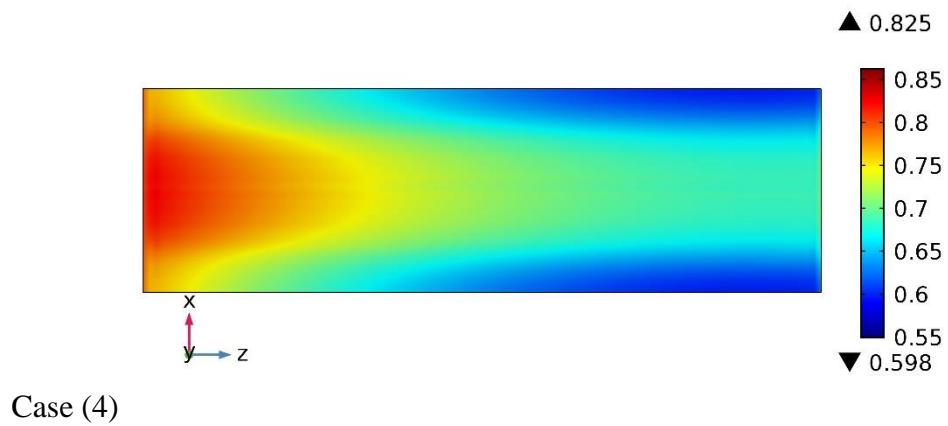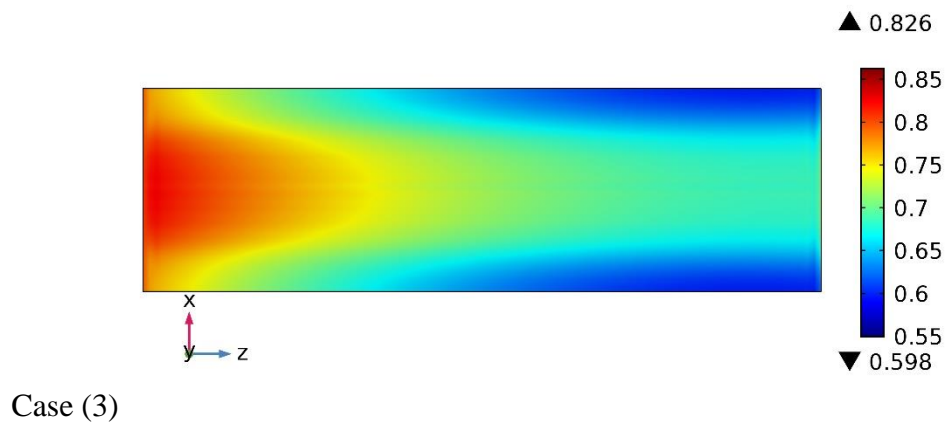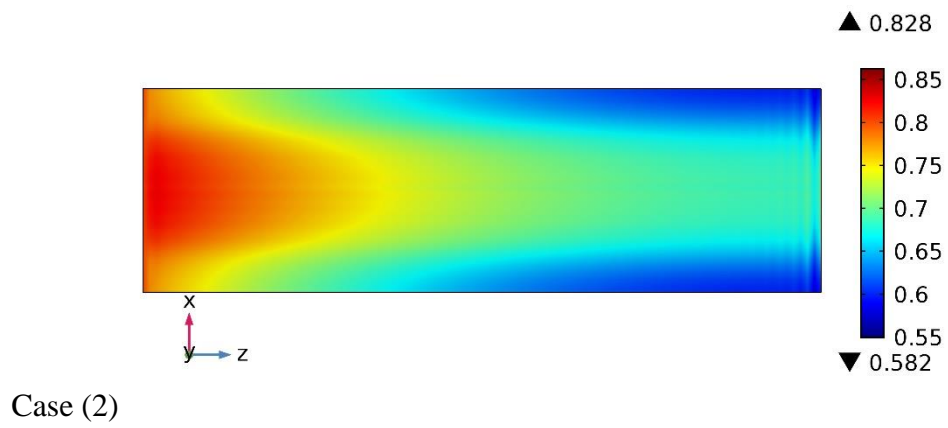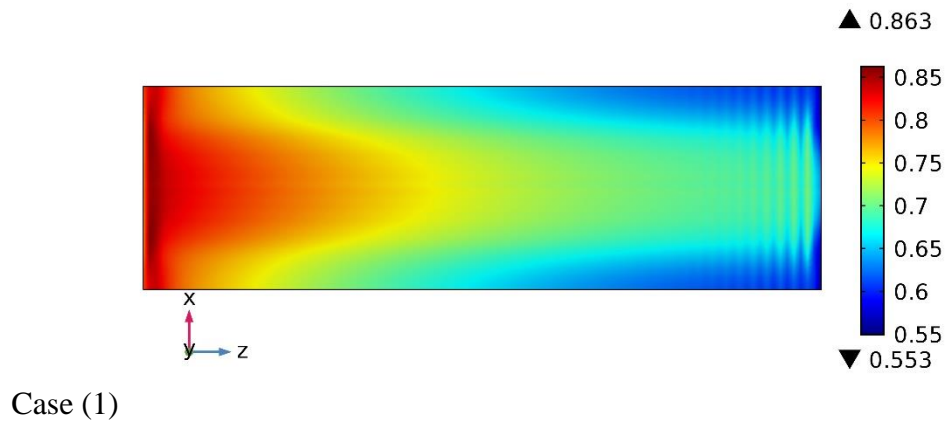
Figure 3. 4. Hydrogen mass fraction distribution at the IAE (case 1,2,3,4,5)

3.3 Current Distribution

The electronic current distribution which is an assimilation at the IAE, is depicted in Figure 3.5 for the 5 cases. Note that the color scale is maintained similar. As observed, the electronic current density appears higher at the anode inlet where the concentration of fuel is maximum, but decreases noticeably in the main flow direction as oxygen and hydrogen are consumed and the steam is produced towards the outlet (z direction).

In the direction normal to the main flow direction (x direction), the highest electrode current density is close to the channel/interconnect interfaces. In this zone, the concentration of oxygen is high and the electron transfer distance is short. Besides, the fuel concentration reduced along the fuel flow direction, and attained the minimal mole fraction at the outlet which evolved the lowest current densities.

Although the mass fraction of hydrogen rises with the increase of permeability in porous medium, the higher value of electronic current density noticed is for case 4 ($k = 1.76 \times 10^{-12}$ m²) which ranges between 412 A m^{-2} and 2,004 A m^{-2}, while the other cases present lower values of electronic current density, for example, it ranges between 365 A m^{-2} and 1,985 A m^{-2} (1st case), 399 A m^{-2} and 1,986 A m^{-2} (5th case).

In this study, the current density is obtained using the Butler-Volmer equation [6] and the exchange current density [1,12], which are function of partial pressure of gases and temperature. By assuming the gases are ideal, their activities in electrodes depend to their partial pressures, which are derived from the exchange current density. The variation of electronic current density discussed above, could be explicated by the local values of partial pressures of hydrogen and water at the anode active layer.

69

In Figure 3.6a, an increase of the diffusion flux at the interface anode electrolyte can be observed from 2.807×10^{-5} kg m^{-2} s^{-1} for case 5 to 2.843×10^{-5} kg m^{-2} s^{-1} for case 4, then, a more uniform distribution is perceived until $k= 1.76 \times 10^{-10}$ m² and it increases again crucially for $k=1.76 \times 10^{-9}$ m² to 2.919×10^{-5} kg m^{-2} s^{-1}).

By reducing permeabilities, the diffusion of species is reduced because the fuel gas permeation to the porous layer is dropped. In addition, the pressure at the active layer (AF) is enhanced especially with small permeabilities, it evolves slightly from 1.019×10^{5} Pa for $k=1.76 \times 10^{-9}$ m² to 1.023×10^{5} Pa for $k=1.76 \times 10^{-12}$ m² and marked an important rise for $k=1.76 \times 10^{-13}$ m² with pressure equal to 1.040×10^{5} Pa. This evolution is due to the compactness and difficult permeation of fuel at the porous media.

On the other hand, the increase of pressure leads to heighten both average ionic and electronic current density (Figure 3.6b), the ionic current density reaches a value equal to 586.66 A m^{-2} for $k=1.76 \times 10^{-12}$ m² and the electronic current density affects 1135.8 A m^{-2} for the same case. It is worth mentioning, that it performs better than the standard case ($k= 1.76 \times 10^{-11}$ m²).

It's known that the cell performance raises when the pressure raises, this is due to the increased reactant concentration at the reaction layer due to the ease with which the fuel and oxidant diffuses [13,14]. However, the average current density drops for $k=1.76 \times 10^{-13}$ m² owing to the low diffusion over the active layer of electrodes.

In fact, higher permeability can enhance gas diffusion, which ensures a sufficient supply of reactants and removal of products, reducing concentration polarization and improving electrochemical performance. However, it can also lead to a more porous structure, potentially lowering the electronic and ionic conductivities if the connectivity of conductive pathways is compromised. Conversely, lower permeability may improve structural integrity and connectivity, enhancing conductivity, but can hinder gas transport, reducing overall cell performance. Balancing permeability and conductivity is crucial for optimal electrode design [15-22].

Case (1)

Case (2)

Case (3)

Case (4)
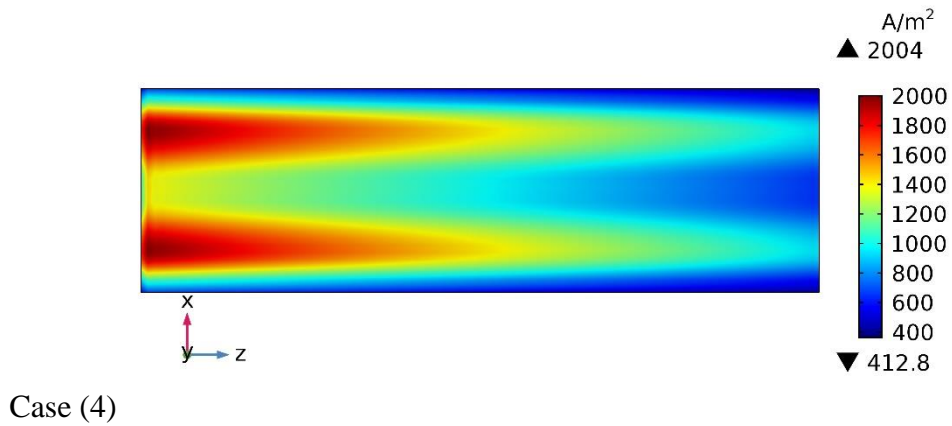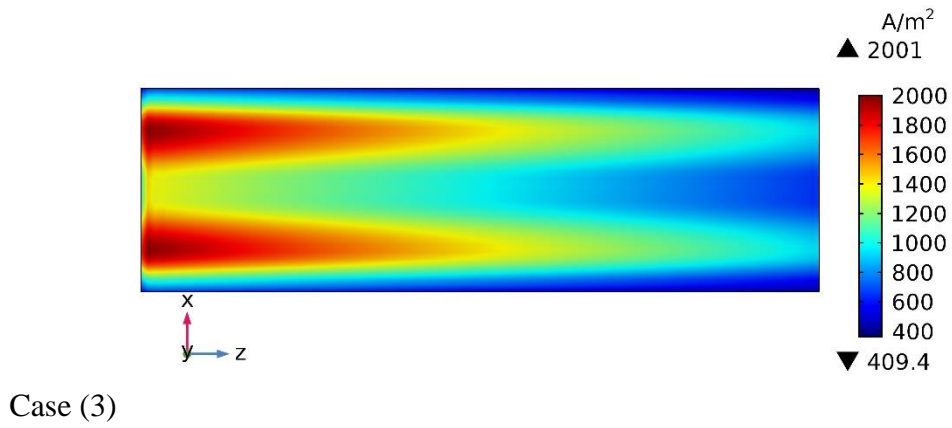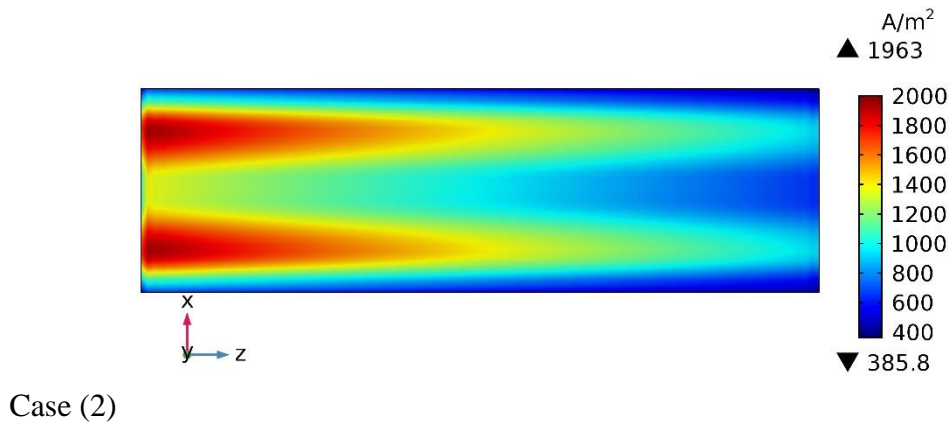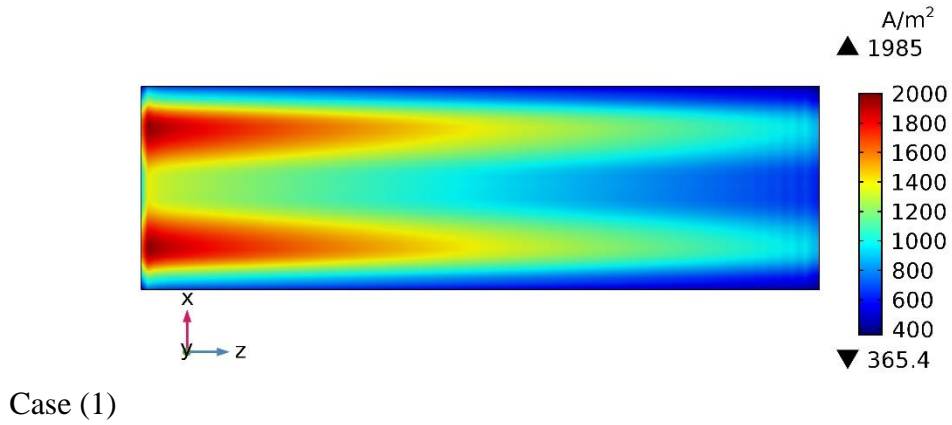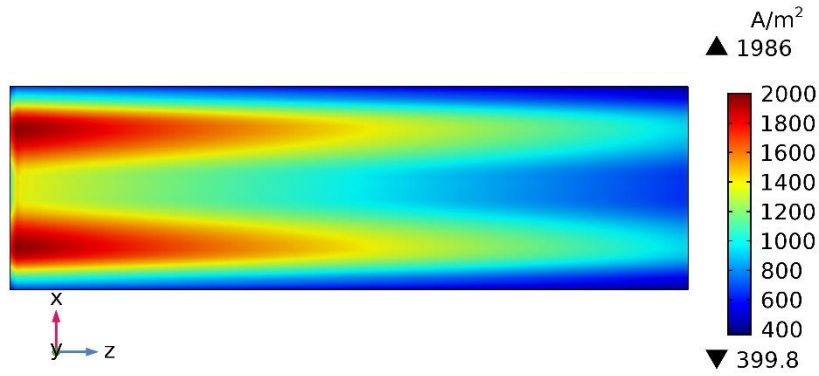
Case (5)

Figure 3. 5. Electronic current density distribution (A/m²) at the IAE (case 1,2,3,4,5)
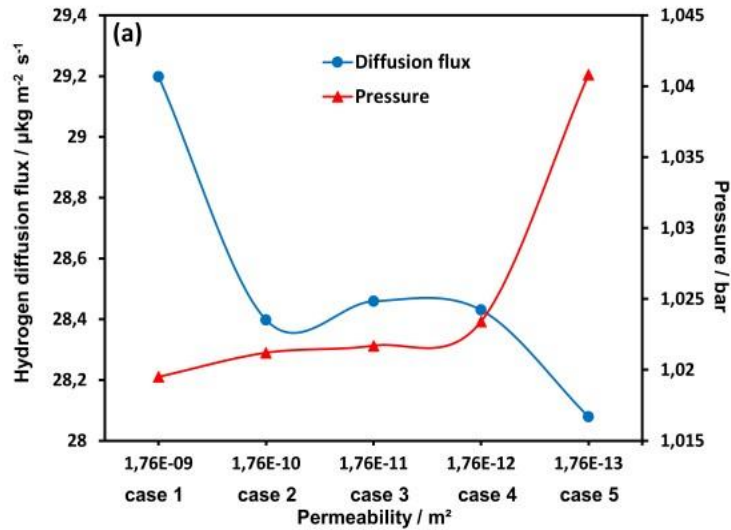

Figure 3. 6.a: Evolution of pressure and diffusion flux of hydrogen with different permeabilities
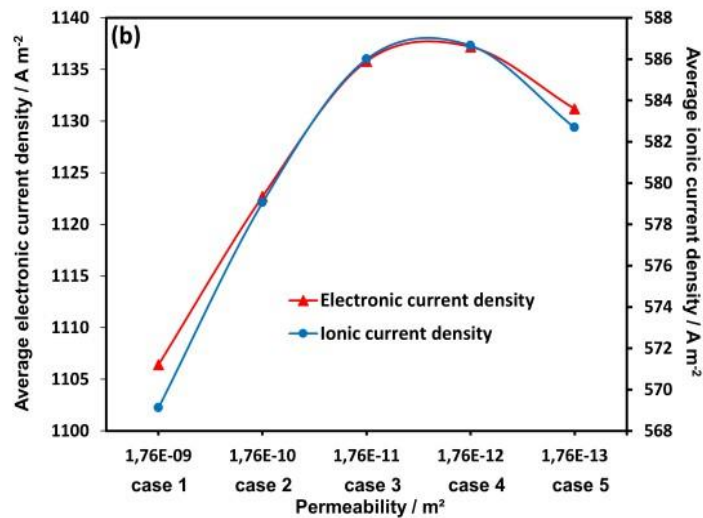

Figure 3.6-b: Evolution of average current density with different permeabilities

3.4 Parametric Sweep Analysis

The parametric sweeps are executed in order to investigate the current density response profile as a function of the permeability of the active layers of electrodes - AFL and CFL - which are composed of ionic, electronic, and porous phase.

The first group (group a) of the parametric sweep represents the electronic phase volume fraction (FVE) - Figures 3.7a and Figure 3.8a - and the second group (group b) represents the ionic phase volume fraction (FVI) - Figures 3.7b and Figure 3.8b. Both FVE and FVI are varied from 0.2 to 0.35. For the group a and group b, the local current density profile results were obtained by changing the permeability of the active layer from case 1 to case 5 (see Tables 3.3 and 3.5 for the conditions), and moreover, gradually varying the permeability of support layer (SL) and diffusion layer (DL) for each case at the same time (Figure 3.7). It should be noted that group (a) and group (b) are the exact opposite of each other.

For the FVE, the simulation results reveal that the local current density at IAE increases with the decreasing permeability, attaining the higher values for $k= 1.76 \times 10^{-12}$ m².

The current density profiles remain almost constant with the increase of the volume fraction of electronic phase for high permeabilities, while the profiles show an increase for low permeabilities ($k= 1.76 \times 10^{-12}$ m² and $k= 1.76 \times 10^{-13}$ m²).

For the FVI, the figures show that the maximum current densities are achieved at a range between $k= 1.76 \times 10^{-11}$ m² and $k= 1.76 \times 10^{-12}$ m², and drop again with $k= 1.76 \times 10^{-13}$ m². Moreover, raising the volume fraction of ionic phase from 0.2 to 0.35, leads to an increase of the current density in all cases.

According to these results, the permeability at the electrode diffusion layer has an important impact on the SOFC operation. The current density achieves the higher values for the case 4 (7713.8 A m^{-2} for FVE=0.35, and 7611.6 A m^{-2} for FVI= 0.35), with $k= 1.76 \times 10^{-12}$ m² at the diffusion layers (ASL and CDL), although the permeability is large at the active layer. Almost similar results are presented in the other cases with some difference in current density values.

Using large permeability ($k= 1.76 \times 10^{-9}$ m²) in the diffusion layer, the current density falls significantly in all cases. Likewise, it is relatively low also with $k= 1.76 \times 10^{-10}$ m².

Therefore, an high permeability of the diffusion layer negatively affects the performance of SOFC. As explained in the previous section, the current density improves with the lowering of permeability, up to a defined value, and then it drops with very small permeability due to the impact of diffusion of species and pressure in the porous media.

Based upon the results of the simulation shown in Figure 3.7, the most relevant results are selected and shown in Figure 3.8a and Figure 3.8b, in order to compare profiles of different permeabilities in the active layer.

These figures indicate always that the best performance is obtained when k= 1.76x10^{-12} m², and achieve better results than the standard case (k= 1.76x10^{-11} m²).

In Figure 3.8, all cases present an increase of local current density with the increase of volume fraction of both electronic and ionic phases. Note that Ni fraction and LSM fraction are the volume fractions of the electronic phases in anode and cathode, respectively, while YSZ fraction is the volume fraction of the ionic phase of electrodes. In the literature, the cell performance enhances when the Ni fraction, YSZ fraction and LSM fraction are close or equal to the 50% of the solid fraction of the electrode [23,24]. Therefore, the higher current density obtained in the simulation with the increasing volume fractions of electronic and ionic phases up to 0.35 (i.e. 50% of the solid phase of the electrode) is reasonable and in agreement with the literature.

In the case 8a, the magnitude of the increase of the current density for a permeability which ranges between k= 1.76x10^{-9} m² and k= 1.76x10^{-12} m² is very low. The results show that the current density reaches its saturation and remains stable with different permeabilities with the increase of the FVE and it seems constant for k= 1.76x10^{-13} m². However, varying permeability in the active volume of the electrode has a greater effect on the current density as a function of volume fraction of ionic phase.

In this study, taking into account that tortuosity and porosity are constant, and according to Carman Kozney's law, the size of the particles (Ni, LSM, and YSZ) vary proportionally to the permeability [22,25]:

$$k = \frac{d^2 \, \varepsilon^3}{72 \, \tau^2 \, (1 - \varepsilon)^2}$$

Where d is the particle diameter, ε is the porosity, and τ is the tortuosity

Previous studies [26-29] revealed that as particle size is reduced, the number of particles populating the porous media increases, which explains the rise of TPB global density (active sites).

Larger particle sizes designate that the contact area particle-particle is also large. As particle size diminishes, the contact surface area diminishes as well, however is counterbalanced by an increment in the number of particles in contact, as evidenced by the nonlinear increment in TPB density. It can be inferred that the uniform distribution of conducting phase, which reduced the cell's ohmic polarization loss, is the source of the elevated electrical conductivity as well [15].

According to the results, there was an increase in current density which reaches a local maximum followed by a reduction in performance as permeability and particle size further reduces. It is demonstrated that the ensuing decline in performance at lower electron particle sizes is caused by the lowering in the normalized effective transport in the ion phase [27,30].

The improvement of transport within the ionic phase and using smaller permeability, resulting in smaller ion particles, could lead to better performance within SOFC.

In addition, and as described earlier, decreasing permeability leads to improve the occupancy of species in the porous media due to the increment of pressure and the enlarge of the reaction sites, moreover, it improves the presence of YSZ fraction of ionic phase, so that, molecules of hydrogen H_2 and O_2 ionize more to ions H^+ and O^{2-} respectively at the active layer: as a consequence, the current density enhanced.
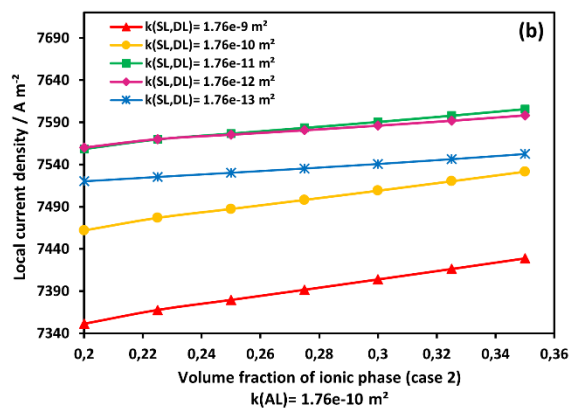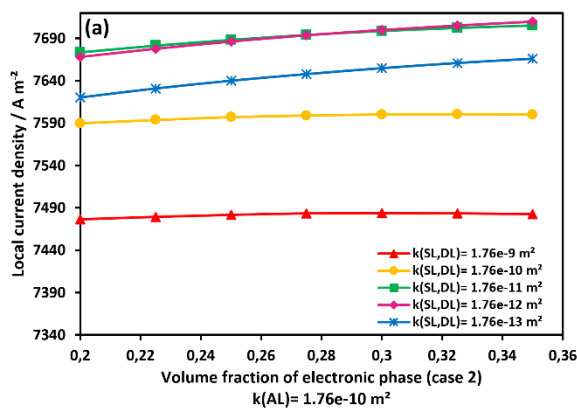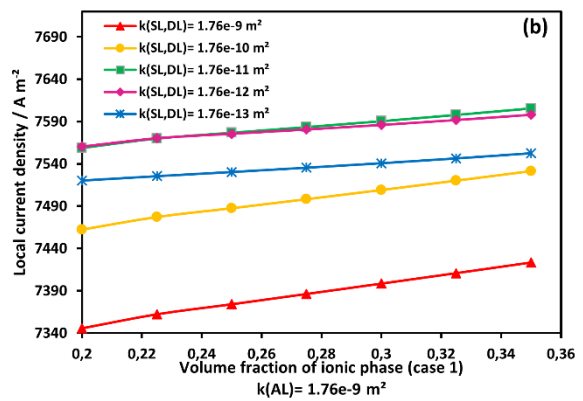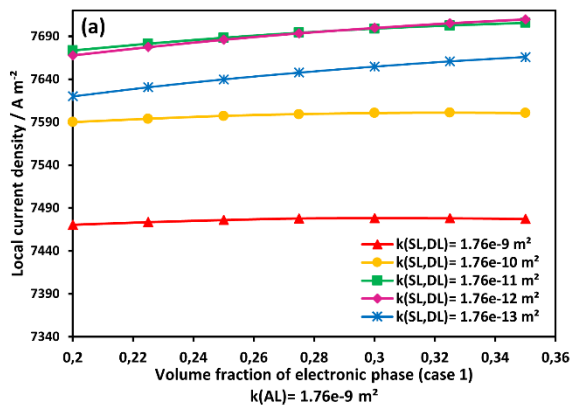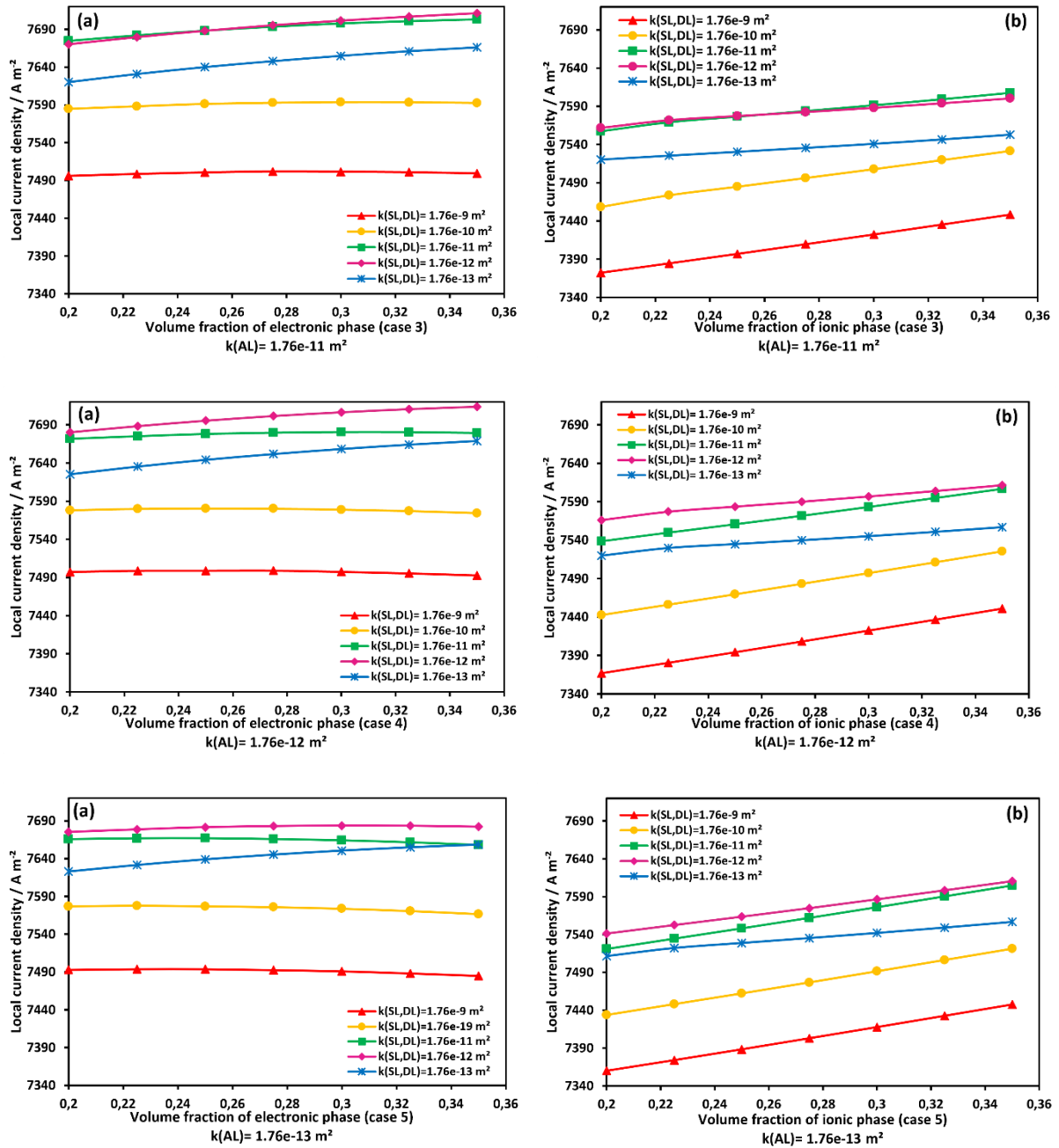
Figure 3. 7. Local current density as function of volume fraction of (a) electronic and (b) ionic phase for different permeabilities (case 1,2,3,4 and 5).
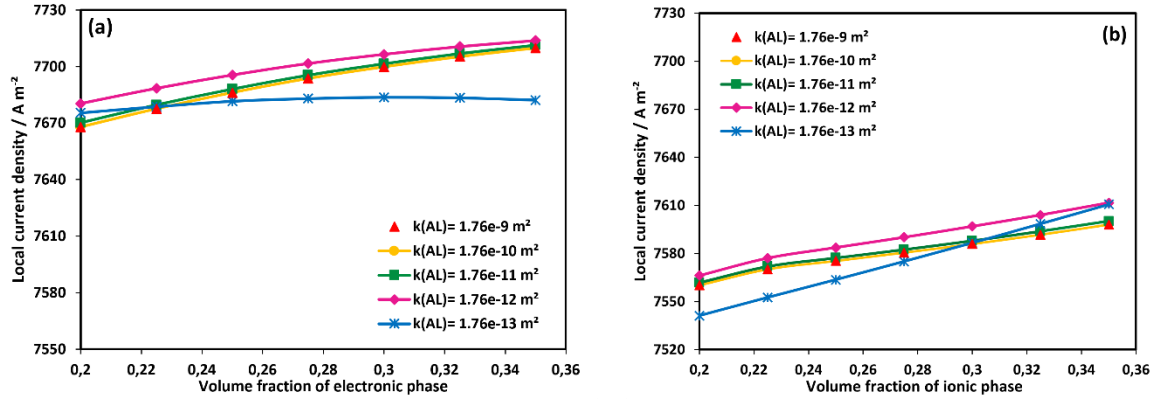
Figure 3. 8. Local current density in function of (a) electronic and (b) ionic phase for different permeabilities.

4 Conclusion

A three-dimensional model of an hydrogen fueled single SOFC has been developed implementing the conservation equations of mass, species, momentum, energy, and charge (electrons and ions). The simulation involved fuel and air flow channels, electrode support, diffusion and active layers, electrolytes and interconnects.

The model has been validated over experimental data and has been employed to study the impact on SOFC performance of permeability and volume fractions of ionic and electronic conductors in the electrodes.

The most important results and conclusions can be summarized as follows:

(i)   The lowering of permeability in the porous media until a defined value (k= 1.76x10^{-12} m² for this study) deals to balance the diffusion of species and the rise of the pressure, inducing the improvement of current density.

(ii)   The increase of electronic and ionic phase volume fraction in the active layer, support layer and diffusion layer leads to an increase of the current density.

(iii)   Varying the permeability in the support layer and diffusion layer has a greater impact than its variation in the active layer on the SOFC operation.

(iv)   The impact on the current density of the change in permeability is more relevant as a function of volume fraction of ionic phase, as the ionic phase shows an higher influence than the electronic phase.

(v)   The design of high-performance SOFC electrodes requires the use of size-dependent volume fractions, as the particle size reduces the permeability decreases and the reaction sites increase attaining the optimal microstructure conception.

References

[1] Zhang X, Espinoza M, Li T, Andersson M. Parametric study for electrode microstructure influence on SOFC performance. Int. J. Hydrogen Energy 2021, 46: 37440-37459.

[2] Zhang X, Parbey J, Yu G, Li T, Andersson M. Thermal stress analysis of solid oxide fuel cells with chromium poisoning cathodes. J. Electrochem. Soc. 2018;165: F1224-F1231.

[3] Modeling with electrochemistry. COMSOL multiphysics version 5.5, batteries and fuel cells module users guide, chapter 2: modeling with electrochemistry, Stockholm, Sweden. 2019.

[4] Patcharavorachot Y, Arpornwichanop A, Chuachuensuk A. Electrochemical study of a planar solid oxide fuel cell: role of support structures. J Power Sources 2008; 177: 254-261.

[5] Andersson M, SOFC Modeling Considering Mass and Heat Transfer, Fluid Flow with Internal Reforming Reactions, Licentiate Thesis, Lund University, Sweden, 2009

[6] Ferrero D, Lanzini A, Santarelli M. Solid Oxide Fuel Cells Modeling. In: Boaro M, Salvatore, A. (eds) Advances in Medium and High Temperature Solid Oxide Fuel Cell Technology. CISM International Centre for Mechanical Sciences, vol 574. Springer, Cham. 2017; 574: 291–342

[7] Andersson M, Yuan J, Sundén B. SOFC modeling considering electrochemical reactions at the active three phase boundaries. Int J Heat Mass Transf. 2012; 55: 773-788.

[8] Shi J, Xue X. CFD analysis of a novel symmetrical planar SOFC design with micro-flow channels. J Chem Eng. 2010; 163: 119-125.

[9] Akkaya AV. Electrochemical model for performance analysis of a tubular SOFC. Int J Energy Res. 2007; 31: 79-98

[10] Andersson M, Yuan J, Sunden B. SOFC modeling considering hydrogen and carbon monoxide as electrochemical reactants. J Power Sources 2013; 232: 42-54

[11] Fu Q, Li Q, Wei W, Liu F, Xu X, Liu Z. Performance enhancement of a beam and slot interconnector for anode-supported SOFC stack. Energy Convers. Manage 2021; 241:114277

[12] Takino K, Tachikawa Y, Mori K, Lyth SM, Shiratori Y, Taniguchi S, Sasaki K. Simulation of SOFC performance using a modified exchange current density for pre-reformed methane-based fuels. Int. J. Hydrogen Energy 2020; 45: 6912-6925.

[13] Ighodaro OO, Scott K, Xing L. An Isothermal Study of the Electrochemical Performance of Intermediate Temperature Solid Oxide Fuel Cells. *J. Power Energy Eng*. 2017; 5: 97-122.

[14] Ighodaro OO. Modelling and Simulation of Intermediate Temperature Solid Oxide Fuel Cells and their Integration in Hybrid Gas Turbine Plants. Thesis, School of Chemical Engineering and Advanced Materials. Newcastle University, Royaume-Uni, 2016

[15] Lee J-H, Heoa J-W, Leea D-S, Kima J, Kima G-H, Leea H-W, Songa HS, Moon J-H. The impact of anode microstructure on the power generating characteristics of SOFC. Solid State Ionics 2003; 158: 225-232.

[16] Chellehbari YM, Adavi K, Amin K, Zendehboudi S. A numerical simulation to effectively assess impacts of flow channels characteristics on solid oxide fuel cell performance. Energy Convers. Manage. 2021; 244: 114280.

[17] Kaya MF, Demir N, Genç G, Yapici H. Numerically Modeling of Anode Supported Tubular SOFC. International Conference and Exhibition on Mechanical & Aerospace Engineering, United States of America. 2013; 1-8.

[18] Akhtar N, Decent SP, Kendall K. A parametric analysis of a micro-tubular, single-chamber solid oxide fuel cell (MT-SC-SOFC). Int. J. Hydrogen Energy 2011; 765-772.

[19] Moon H, Kim SD, Park EW, Hyun SH, Kim HS. Characteristics of SOFC single cells with anode active layer via tape casting and co-firing. International Journal of Hydrogen Energy 2008; 33(11), 2826-2833.

[20] Yuan J, Rokni M, Sundén B. Three-dimensional computational analysis of gas and heat transport phenomena in ducts relevant for anode-supported solid oxide fuel cells. International Journal of Heat and Mass Transfer 2003; 46(5), 809-821.

[21] Yuan J, Huang Y, Sundén B, Wang WG. Analysis of parameter effects on chemical reaction coupled transport phenomena in SOFC anodes. Heat and Mass Transfer 2009; 45, 471-484.

[22] Shi J, Xue X. CFD analysis of a symmetrical planar SOFC with heterogeneous electrode properties. Electrochimica Acta 2010; 55(18), 5263-5273.

[23] Hussain MM, Li X, Dincer I. Mathematical modeling of planar solid oxide fuel cells. Journal of Power Sources 2006. 161(2): p. 1012-1022.

[24] Costamagna P, Costa P, Antonucci V. Micro-modelling of solid oxide fuel cell electrodes. Electrochimica Acta 1998; 43(3-4), 375-394.

[25] Lala AMS. Modifications to the Kozeny–Carman model to enhance petrophysical relationships. Exploration Geophysics 2018, 49(4), 553-558.

[26] Timurkutluk B, Ciflik Y, Altan T, Genc O. Synthetical designing of solid oxide fuel cell electrodes: Effect of particle size and volume fraction. International Journal of Hydrogen Energy 2022; 47(73), 31446-31458.

[27] Kenney B, Valdmanis M, Baker C, Pharoah JG, Karan K. Computation of TPB length, surface area and pore size from numerical reconstruction of composite solid oxide fuel cell electrodes. Journal of Power Sources 2009; 189(2), 1051-1059.

[28] Timurkutluk B, Ciflik Y, Sonugur G, Altan T, Genc O. Quantitative estimation of triple phase boundaries in solid oxide fuel cell electrodes via artificial neural network. Fuel 2024; 357, 129687.

[29] Abbaspour A, Luo JL, Nandakumar K. Three-dimensional random resistor-network model for solid oxide fuel cell composite electrodes. Electrochimica Acta 2016; 55(12), 3944

[30] Gawel DAW. The development of a coupled physics and kinetics model to computationally predict the powder to power performance of solid oxide fuel cell anode microstructur Queen's University (Canada), 2013.

Chapter 4: Numerical study on performance enhancement of a solid oxide fuel cell using gas flow field with obstacles and metal foam

1 Introduction

This chapter explores the effect of gas flow field design on the performance of solid oxide fuel cells (SOFCs). We develop a three-dimensional numerical model to simulate the use of metal foam as a flow distributor and the impact of obstacles within the gas flow channels. Calibrated with experimental data, the model is used to analyze four different configurations combining metal foam and obstacles, comparing them to a conventional straight channel design. Our findings reveal that modifying the flow field positively affects the distribution of species along the cell's active layers. Although pressure drops are influenced, the improved distribution of reactant gases across the active electrode reduces mass transport losses and enhances current density. Simulations at a cell voltage of 0.7 V show that using metal foam as a flow distributor increases the maximum current density by 26% compared to the straight channel design. Moreover, integrating metal foam with obstacles yields the highest performance, achieving a 34% increase in maximum current density.

2 Numerical model

In this chapter, the numerical model has been developed using the same governing equations, boundary conditions and assumptions described in the chapter 3 [1-10].

The geometry parameters are shown in Table 3.1 and the physical parameters are listed in Table 3.2 and Table 3.3.

The physical properties of the metal foam used in this model are presented in Table 4.1.

Tableau 4. 1. Physical properties [11]

Parameter	Value	Units
Metal foam thermal conductivity	90	W m^{-1} K^{-1}
Metal foam specific heat	440	J kg^{-1} K^{-1}
Permeability	1x 10^{-9}	m²
Tortuosity	2.3	-
Porosity	0.9	-

Case study

In the present study, the impacts of incorporating obstacles within flow channels and using metal foam instead of straight flow channels on the efficiency of fuel cell are discussed. Four different cases are explored, as indicated in Figure 4.1.

Case A: a SOFC unit with two conventional straight channels, as depicted in Figure 4.1a.

Case B: Five rectangular obstacles positioned 20 mm apart from one another in the flow channels (Figure 4.1b).

Case C: Utilization of a nickel metallic foam with 90% porosity as flow distributor in the SOFC unit (Figure 4.1c).

Case D: Implementation of both 5 obstacles and use of a nickel metallic foam as a flow distributor simultaneously (Figure 4.1d).

All the operating conditions and geometric parameters of the SOFC remain consistent in the four models (Figure 4.1).

(a): Case A   (b): Case B

(c): Case C   (d): Case D
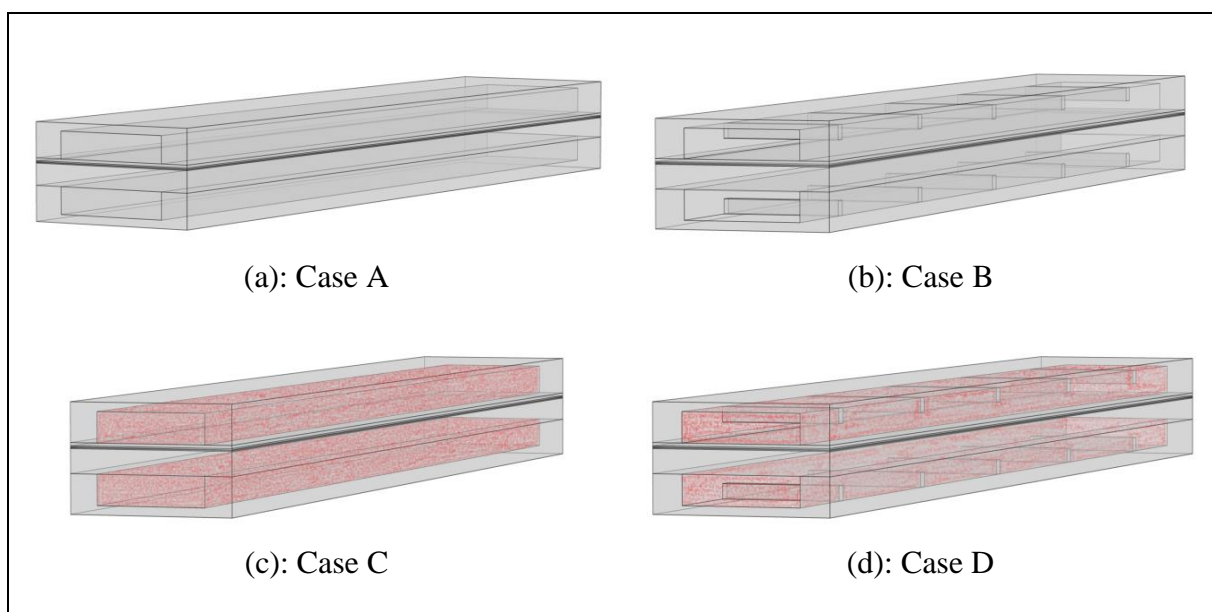
Figure 4. 1. Schematic of the SOFC for the 4 different flow field cases.

3 Results

3.1 Model validation

In order to demonstrate that the model applied in this study can realistically simulate the performance of SOFC, the current model is developed under the same experimental conditions as those provided by Fu et al. [12].

For the experiments, the fuel and the air inlet flow rates are 16 Nml/(min.cm²) and 80 Nml/(min.cm²) respectively at 800°C for the SOFC stacks with traditional straight channel interconnectors (SCIs).

The cell voltage versus current density curve generated through numerical modeling is displayed in Figure 4.2 alongside the curve derived from the experimental data. The maximum

error in this validation result is less than 5%, indicating significant agreement between the experimental and simulation data.
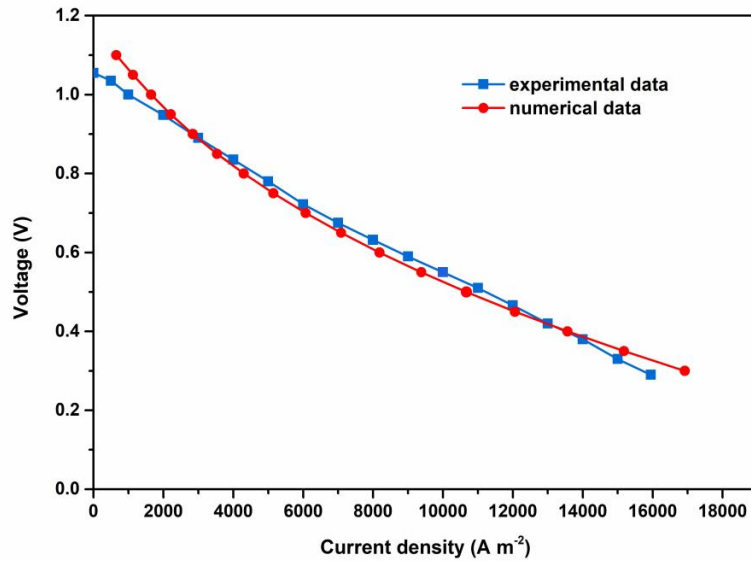
Figure 4. 2. Comparison of Numerical and experimental polarization curves for the SOFC (Ref. [12])
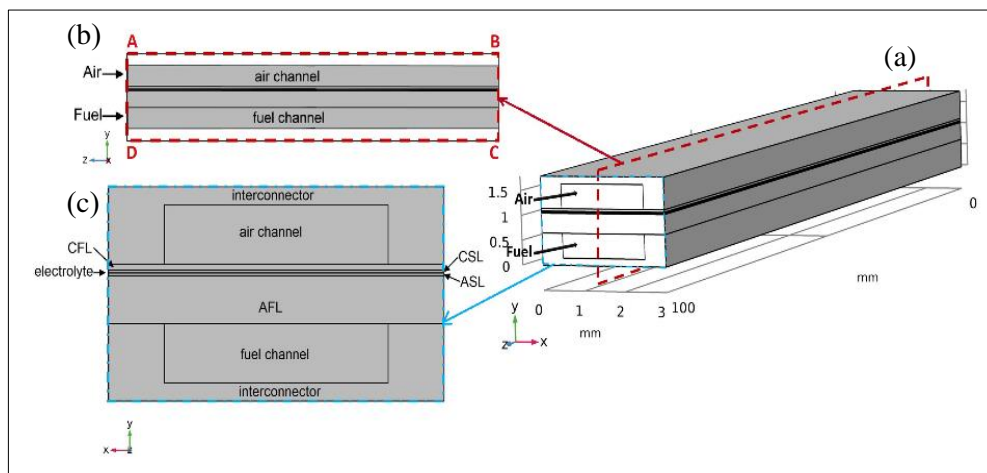
Figure 4. 3. (a) 3D computational domain of SOFC, (b) plane ABCD at the mid-width location of the cell, (c) two-dimensional front view

3.2 Velocity distribution

Figure 4.4 displays the velocity field in the anode side and the cathode side for the four cases. The velocity in the air channel is higher than in the fuel channel in order to manage and deliver sufficient oxygen. As can be seen, the velocity is higher along the core zone of channels. Once fuel and air encounter the cell wall, the gases lose momentum, and the speed decreases. The velocity within the electrodes is also very low due to the small permeation employed in the simulation (k=1.73e-11 m²).

Figure 4.4 shows the difference in velocities distributions at the medium surface of the gas channel (z=50.5mm). Comparing with the base case (case A), the application of obstacles in the case B causes an increase in velocities under the blocks.

In addition, the metal foam used as a flow distributor (case C), creates a more uniform distribution of the velocity fields in the channel of the cell, the anodic and cathodic regions having almost the same velocity field values.

In case D, the placement of obstacles in the presence of a metal foam, induces the same velocity flow distribution as in case B, but with greater values.
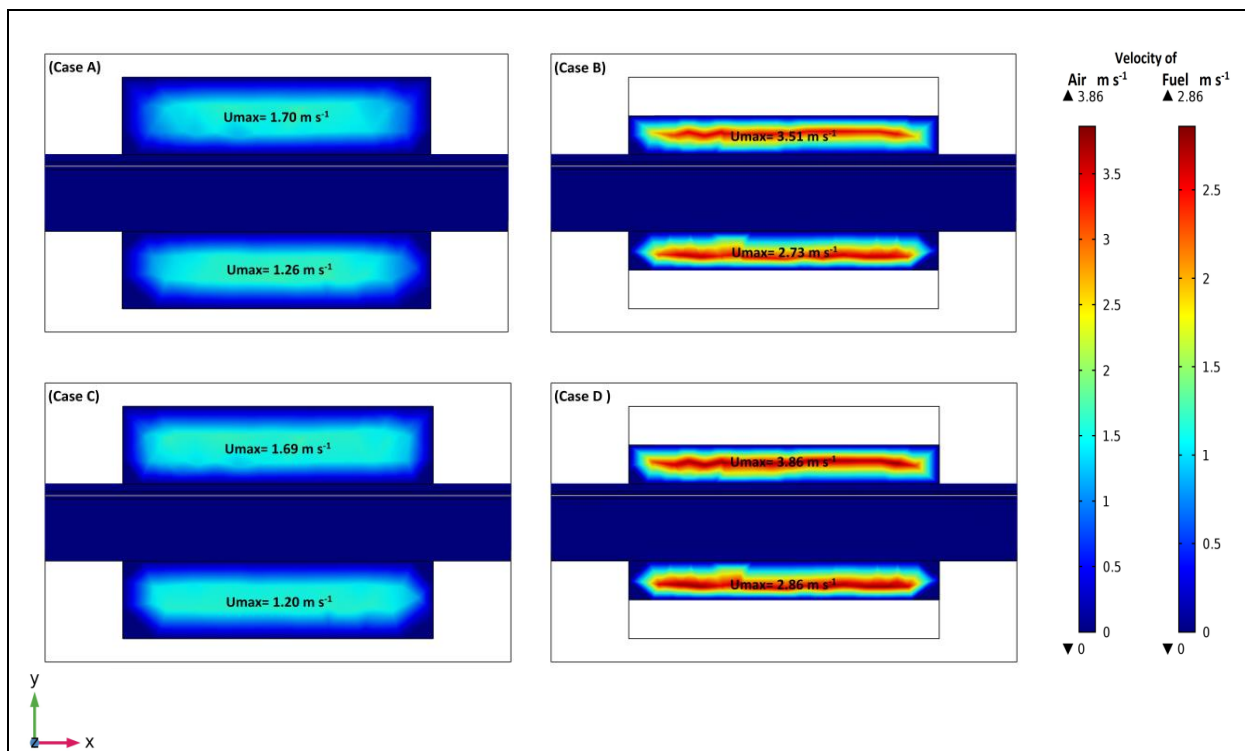
Figure 4. 4. Velocity distributions in the anode side and cathode side (z= 50.5 mm)

Figure 4.5 illustrates a cross-sectional view of the velocity field at the half width section of the fuel cell (the half width section is defined as plane ABCD in Figure 4.5b (for x=1.5mm)). The upmost electrode flow velocity in a straight channel is lower than 2 m/s for the base case (Figure 4.5 (case A)), whereas, it attains 4.38 m/s at the cathode channel and 3.33 m/s at the anode channel, by placing obstacles in the flow channels.

It can be easily observed that the velocity is much higher in regions over the obstacles, forcing the reactant gases to flow into the electrodes: as a consequence, the mass flow rate of hydrogen and oxygen in the diffusion, support and active layers is enhanced (case B).

In addition to fostering a more uniform velocity distribution in the flow field as mentioned above, using a metal foam results in a smoother flow transport and an increase in velocity from 1.98 m/s to 2.59 m/s in the cathode flow channel, which significantly reinforces the mass transfer of gases throughout the electrode diffusion layers (case C).

The adoption of both metal foam and obstacles within the channels (case D) improves the uniformity of flow distribution and significantly boosts the fluid velocity, particularly in the regions between the electrodes and the obstacles, where the reactant species saturation is evident.

At high velocities, the flow changes from the Darcy regime to the Forchheimer regime due to the significant inertial effect [13,14,15]. The maximum flow field velocity in the anode side reaches 3.59 m/s (Figure 4.5 (case D)), besides, it attains 5.76 m/s in the cathode channel, which is almost 3 times as high as the conventional channel. Consequently, a significant increase in the diffusion of oxygen and hydrogen into the porous electrodes is facilitated.
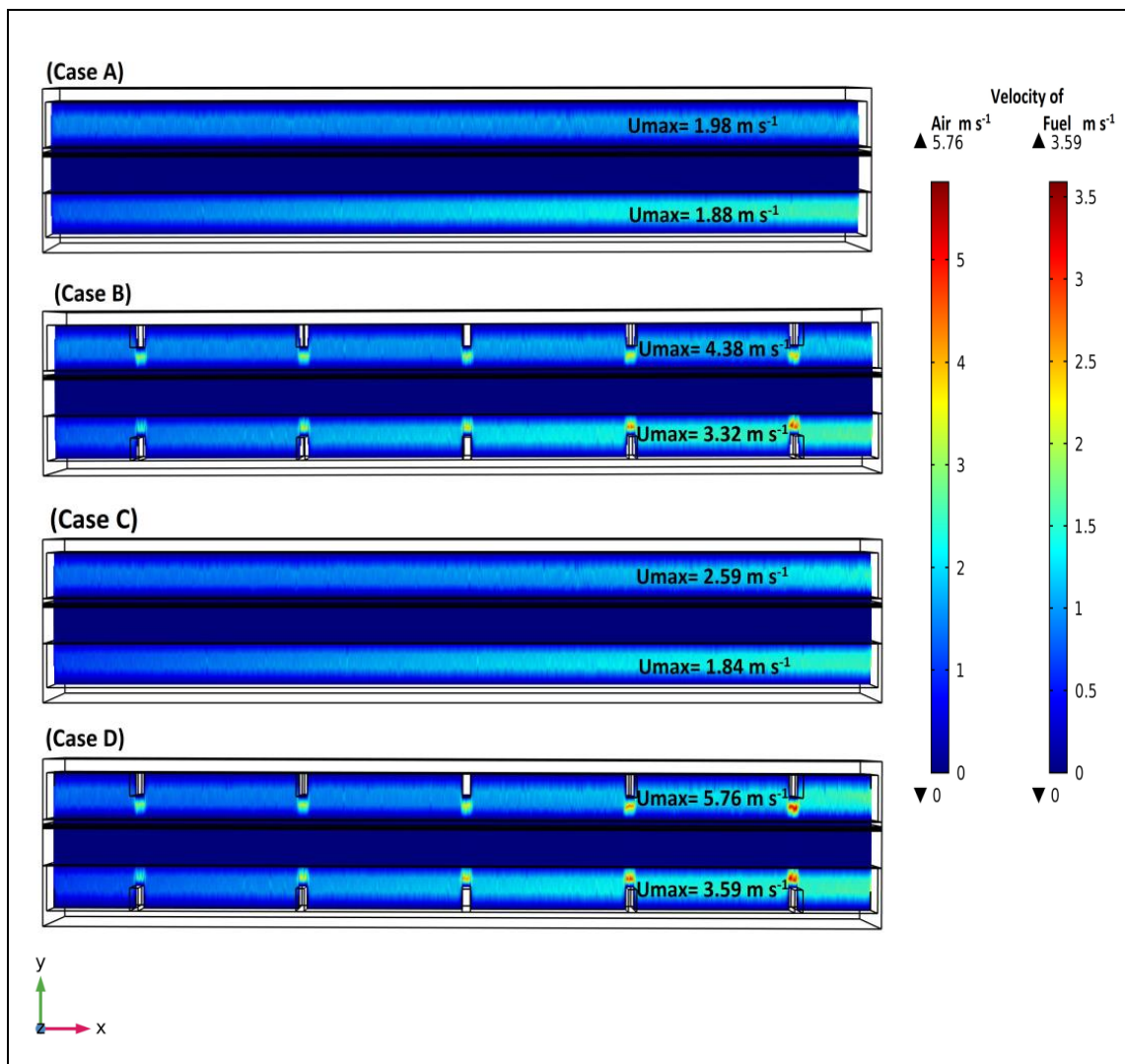

Figure 4. 5. Cross section of velocity distribution at the middle of SOFC (x=1.5mm)

3.3 Pressure drop

Figures 4.6a and 4.6b present the pressure drop along the centerline of the surface between channels and electrodes for all the cases (A, B, C and D).

At the entrance of the SOFC, the pressure drop is quite elevated in response to the high velocity of the flows. The flow is propelled forward by the driving force of the pressure drop, which diminishes to a minimum value at the outlet.

As expected, the pressure drop in case D at the interface between the channels and electrodes is considerably higher compared to the other cases, both at the anode side (Figure 4.6a) and the cathode side (Figure 4.6b). Using a metal foam as a flow distributor alongside the placement of 5 obstacles results in a larger pressure drop compared with the base case A. Additionally, it is evident that the pressure drop increases locally where the obstacles are arranged, compelling the fluid to move towards the porous media.

Similarly, case B indicates a rise of pressure drop compared with base case A. Although the presence of obstacles in the channel enhances the mass transfer in active layers, their impact is much lower compared with the case C.

When metal foam is employed as a flow distributor in the channel flow (case C), the pressure drop is relatively high, compared with case A and case B. In this case, the pressure drop at the entrance of the channel is increased by 4 % in the anode side and by 62 % in the cathode side due to a frictional force between the flow and solid areas of the porous electrodes.

In general, it is also observed that the pressure drop in the cathode (Figure 4.6b) is greater than the pressure drop in the anode (Figure 4.6a), reaching about 2 times higher in case C and D. This occurs because the mass flow rate on the anode side is lower than that on cathode side.
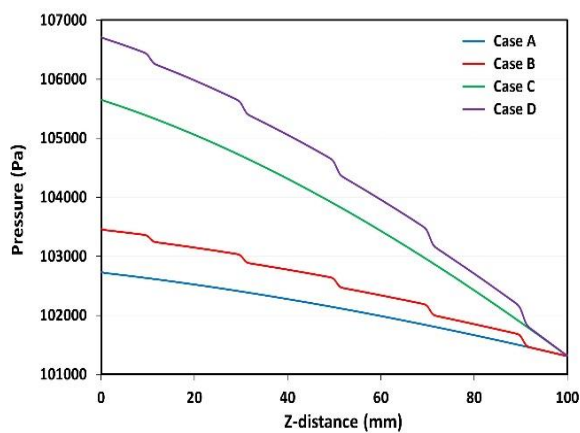

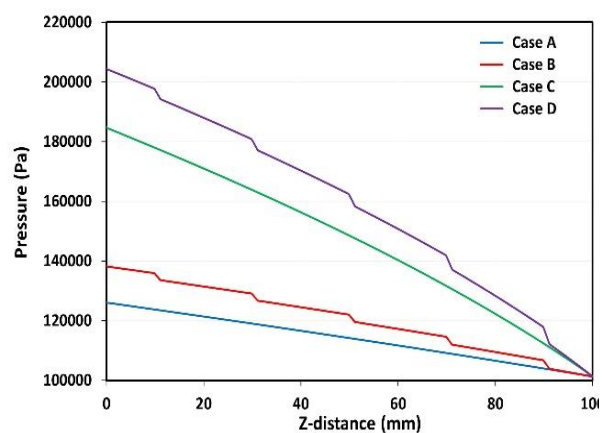**Figure 4. 6.a : Pressure drop at the surface between channel and anode (x = 1.5 mm, y=1.05 mm)**

Figure 4. 6.b: Pressure drop at the surface between channel and cathode (x = 1.5 mm, y=1.145 mm)

3.4   Species transport

In order to perceive the hydrogen penetration flow within SOFC, Figure 4.7 represents the profile of total quantity of fluid transported by convection and diffusion along the cell at the channel-anode support layer interface.

As can be seen, the use of a metal foam enhances convection and diffusion fluxes, facilitating infiltration into the anode. The total flux reaches about $3x10^{-5}$ kg /m².s in case C, which is higher than the base case flux ($2x10^{-5}$ kg /m².s) while following a similar trend along the cell.

The presence of blocks (case B) induces pronounced peaks in hydrogen flux above them. The total flux in this case reaches $9x10^{-5}$ kg /m².s, whereas, it exceeds $10x10^{-5}$ kg /m².s in case D.
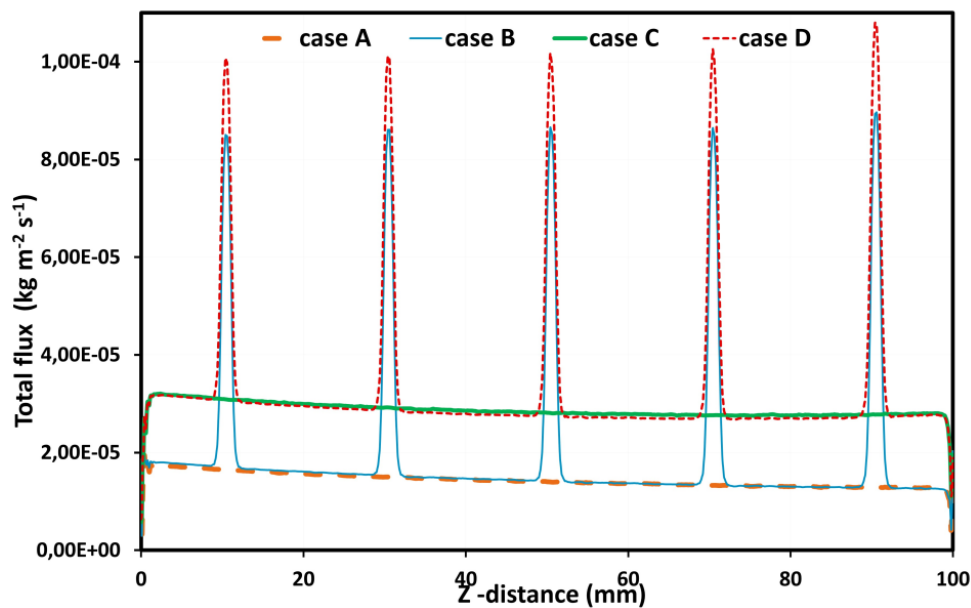
Figure 4. 7. Total flux of hydrogen at the interface channel flow- anode support layers (x=1.5mm, y=0.65mm)

Figures 4.8 and 4.9 present the hydrogen and water mass fraction distribution respectively of the x-z plane (2D) along the interface between anode and electrolyte (IAE) for different cases. It is worth noting that the color scale in these figures is maintained similar for convenient comparison.

In Figure 4.8, It is obvious that the highest mass fraction is observed at the fuel inlet, and it reduces along the fuel channel direction, especially under the ribs of interconnects due to hydrogen consumption through electrochemical reaction.

In general, the mass fraction distribution of hydrogen in the cases B, C and D decreases compared with case A. It is evident that the use of a metal foam leads to a relatively higher consumption of hydrogen due to the uniform distribution and the elevated pressure drop, allowing the reactant gas to be introduced into the entire anode (cases C and D).

Moreover, adding the obstacles could significantly increase the mass transfer throughout the catalyst layer, leading to an enhancement and enlargement of the mass fraction of hydrogen on the local surface where the obstacles are arranged (cases B and D).
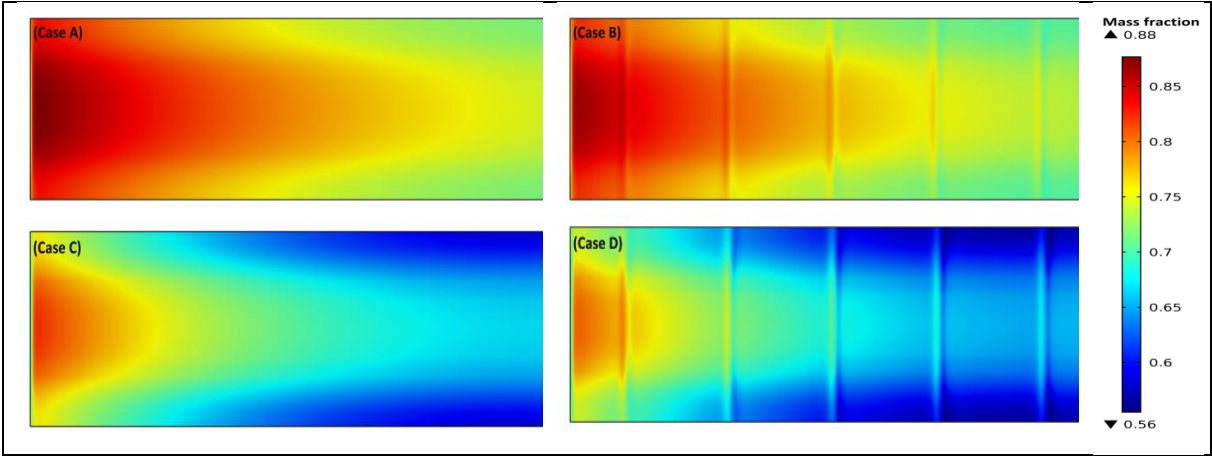
Figure 4. 8. Distribution of hydrogen mass fraction at the IAE (y = 1.065 mm)

Figure 4.9 shows an enhanced water stream generation at the surface where the electrochemical reactions occur when metal foam and obstacles are present.

The case D presents the highest water production rate compared to the base case A. The mass fraction is minimal at the inlet then it increases along the main flow direction, particularly under ribs where the electrochemical reactions predominantly take place.

The efficiency of the reaction is enhanced due to the sufficient penetration of reactive molecules into the porous electrode and their access to the reaction zone. As a result, more oxygen and hydrogen are consumed and consequently more water is produced.

The emergence of the peaks observed above the obstacles is a result of the large amount of water produced in this area. As a consequence, an improvement in current density output occurs.
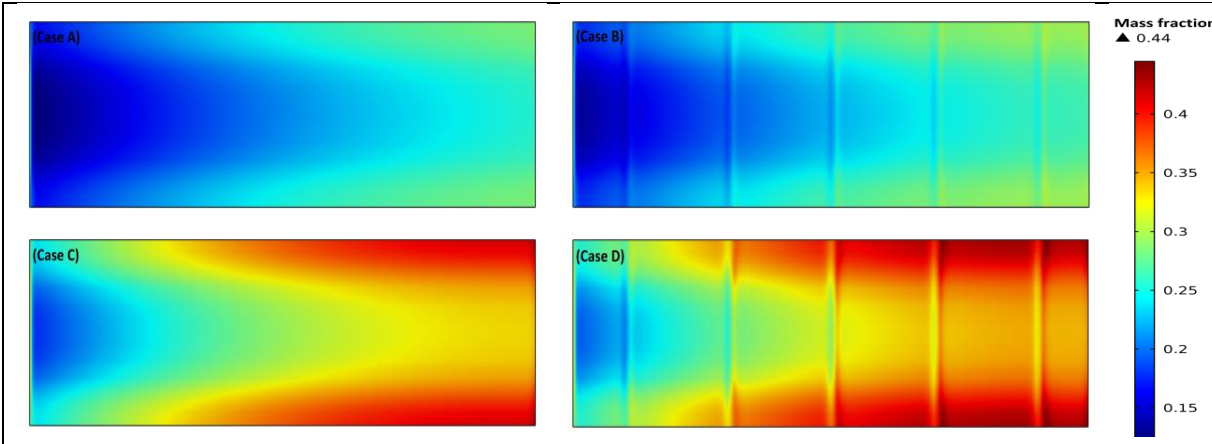
Figure 4. 9. Distribution of water mass fraction at the IAE (y = 1.065 mm)

3.5 Current distribution

The distribution of current density at the IAE interface on the anode side is represented in Figure 4.10 for the four cases; note that the color scale is maintained similar for comparison.

Generally, the current distribution profiles are approximately similar in all the cases.

As illustrated, at the anode inlet where the concentration of fuel is most intense, the electronic current density seems higher, but reduces noticeably in the main flow direction as oxygen and hydrogen are consumed and the steam water and electrons are generated towards the outlet (z direction).

In the direction normal to the main flow direction (x direction), the highest electrode current density is close to the channel/interconnect ribs interfaces. The concentration of oxygen in this region is high and the electron transfer distance is short.

Moreover, the fuel concentration diminishes along the fuel flow direction, and reaches the minimal mole fraction at the outlet which induces the lowest current densities.

As depicted in this Figure, in case B the current density profile experiences five peaks and its maximum value I_{max} increases by 6.4 %, owing to the enhanced pressure drop and reactant concentration over the obstacles, compared to the base configuration (case A).

However, the current density distribution is considerably more intense and uniform a using metal foam (case C) due to the significant reactants transfer volume, and I_{max} boosts by 26.4 %. As expected, the higher efficiency is noticed in case D, in which the maximum current density increases to 2040.9 A/m² compared to 1524.5 A/m² of the base channel, achieving an improvement of 33.9%.
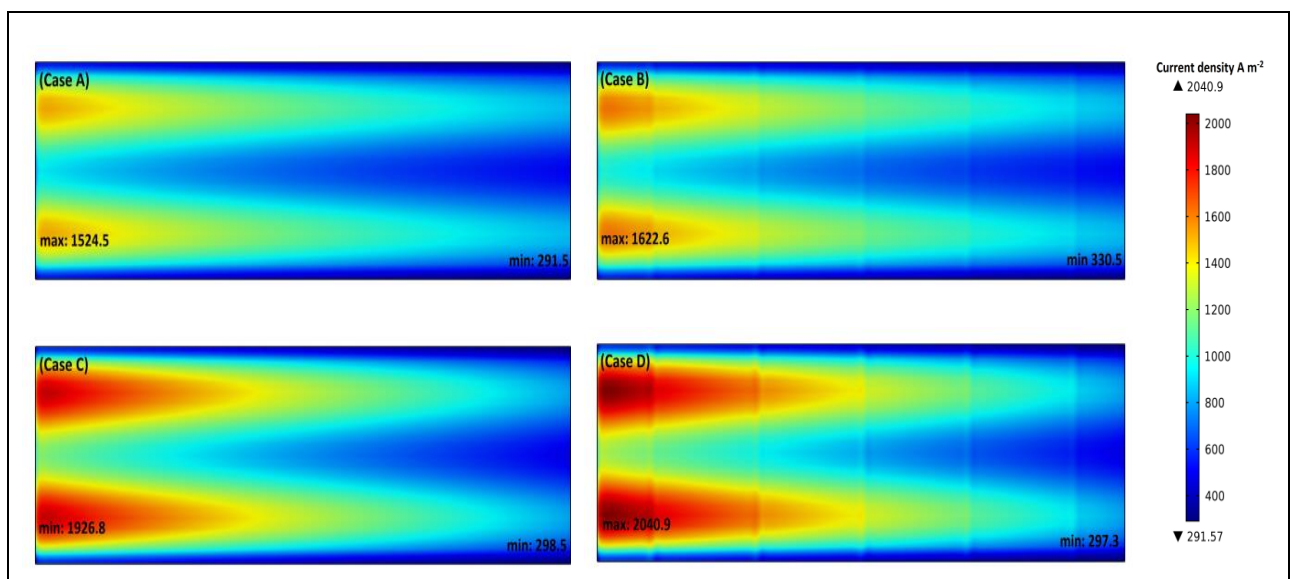
Figure 4. 10. Distribution of current density at the IAE (y = 1.065 mm)

Figure 4.11 displays the local current density at the middle plane of the electrolyte: as can be seen, the current density profiles follow a similar trend as pressure drop profiles.

For instance, in the cases without obstacles profiles exhibit a smooth trend, while in the other cases, they display peaks because of the higher reactant concentration in the areas directly over the obstructions. At the output of the channel, the current density decreases due to the reduced reactants concentration.
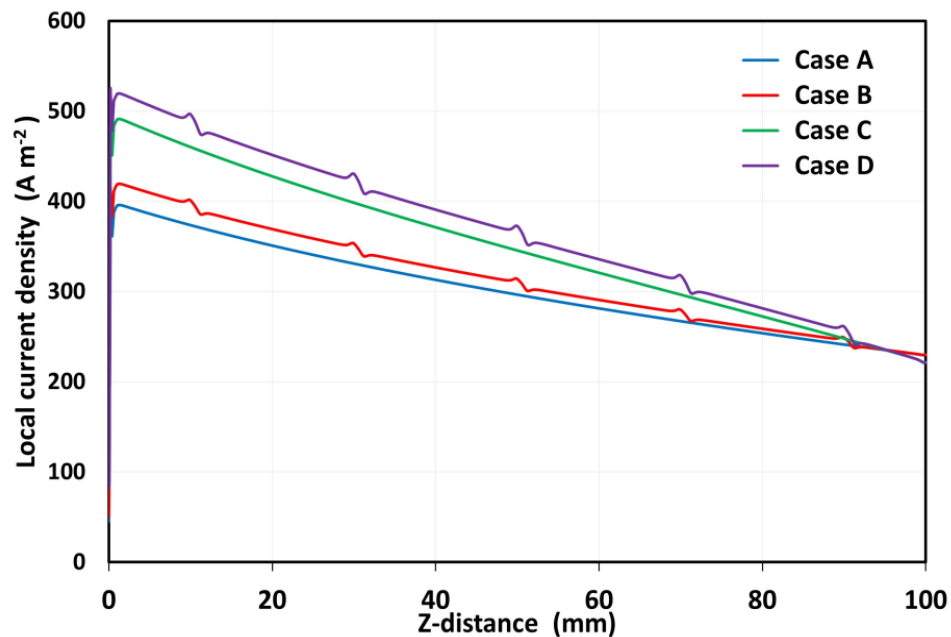
Figure 4. 11.Local current density at the middle plane of the electrolyte
(x = 1.5 mm, y = 1.07 mm)

In this study, The Butler-Volmer equation [16] and the exchange current density [17,18], which are functions of partial pressure of gases, are used to determine the current density. By assuming the gases as ideal, their activities in electrodes depend on their partial pressures, which are affecting the exchange current density and consequently the cell current density.

3.6   Electrical performance

As plotted in Figure 4.12, the polarization curves reveal that Case D presents superior performance compared with other cases. In general, in the low current density range (0–5000 A m^{-2}), there is a negligible difference between the four types of channels, then the selected zone in the figure demonstrates the disparity of polarization at V = 0.7 V; beyond this point, the obstacles and metal foam contribute to the slightly better performance, because mass transport losses predominate in the region with high current density.
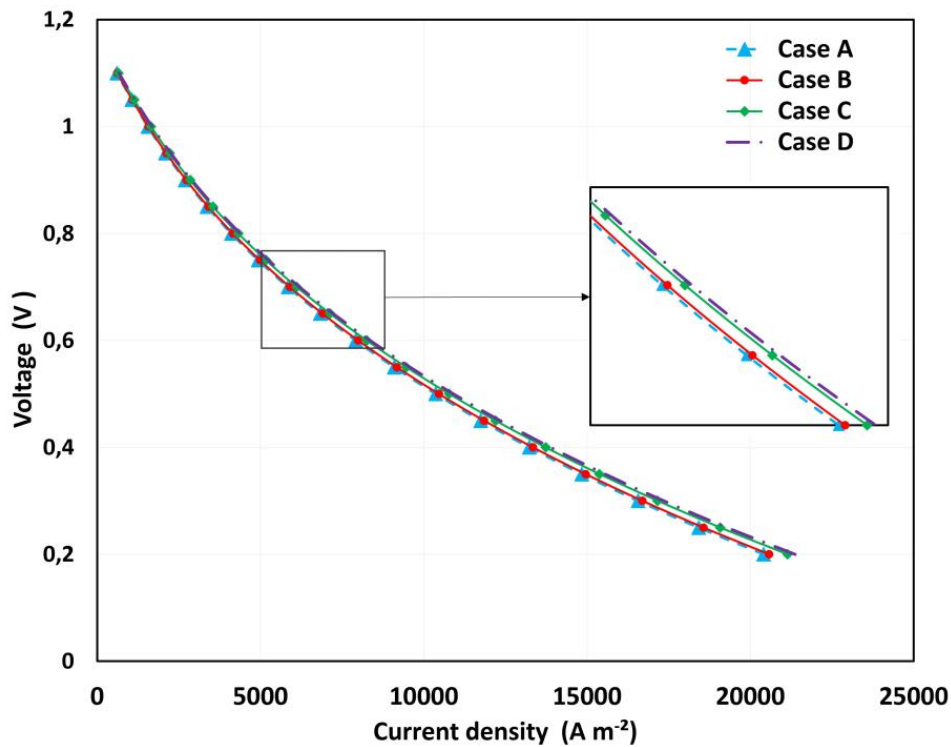
Figure 4. 12. Polarization curves for different cases.

3.7 Results comparison with prior research

From the wide literature, it has been proved that the flow field design has an important impact on the overall behavior of fuel cells. Numerous studies are being conducted to address the main problems, such as the mass transfer issues and the irregular distribution of reactants. In this regard, the flow field design is highly affecting the distribution and the transfer of species in the diffusion and catalyst layers of the electrodes, and consequently the performance of the fuel cell. Therefore, several design modifications are being developed, such as placing different shapes of obstacles throughout the channel and using metal foam as a flow distributor on the serpentine, parallel, or single flow field.

Table 4.2 provides an overview of various flow field designs and fuel cell operating parameters that have been examined experimentally and numerically, together with the main results obtained.

Tableau 4. 2. Comparative overview of previous studies

Authors	Type of fuel cell	Type of flow channel	Operating conditions	Type of study	Remarks
Heihdary. H et al. [19]	PEMFC	- Parallel flow field with partial/ full blockage (1 to 5 blocks)	1 bar/ 353.15 K	Numerical	- Net power is enhanced up to 30% with more blocks number (5) and 100% blockage in the cathode
Kuo. J .K et al. [20]	PEMFC	- Wavy channel	1 bar/ 323-333-343 K	Numerical	- The wave form channel generates better catalytic transfer, convective heat transfer and power density
Tiss. F et al. [21]	PEMFC	- Single channel with 4 partial blocks	1 bar/ 300 K	Experimental and numerical	- Titl angle of partial blocks has an impact on the cell performance, it improves in the presence of blocks
Wan. Z et al. [13]	PEMFC	- M-flow channel	101.3 kPa/ 343 K	Numerical	- M-flow channel produces 21.3% power density better than the wave flow channel
Chellehbari Y.M et al. [22]	SOFC	- Conventional channel with (3-7) rectangle, trapezoidal and triangular obstacles	1 bar/ 1073.15 K	Numerical	- Overpotential decreases as the number of obstacles increases. - Fuel Cell power enhances using obstacles and reaches 35% with 7 triangular obstacles.
Bilgili. M et al. [23]	PEMFC	- Single channel - 49 cases (porous/ baffled channel)	202.65 kPa/ 328.15 K	Numerical	- Different cases affect water saturation and temperature. - Baffled flow field without biporous layers is the best performing case.
Dehsara. M at al. [24]	PEMFC	- Flat channel bed - semicircular channel bed - wavy channel bed	1 bar/ 353 K	Numerical	- channel indentation improves the cell performance up to 22%.
Cai. G et al. [25]	PEMFC	- Bio- inspired wavy channel	101.3 kPa/ 343.15 K	Numerical	- Power density was improved by 22% due to reduced resistance to reactant flow.
Ghanbarian. A et al. [26]	PEMFC	-Parallel flow field with trapezoidal, semi-circular and square dents.	100 kPa/ 333 K	Numerical	- Trapezoidal dent displays the best performance.
Perng. S et al. [27]	HT-PEMFC	- Bipolar-plate channel with	1 bar/ 453 K	Experimental and numerical	-Five bottomed-baffle channel has the best

		bottomed baffles (1-7)			impedance and 8% of power improvement.
Tseng. C.J et al. [28]	PEMFC	- Flow channel plate and metal foam as flow distributor	1 bar/ 303.15-353.15K	Experimental	-Metal foam has a light weight and a unique mass transport property (reactant gases move with less flow resistance).
Afshari. E et al. [29]	PEMFC	- flow channel plate and metal foam as flow distributor	151.987 kPa/ 303.15 K (dry side) 353.15 K (wet side)	Numerical	- Membrane humidifier containing metal foam has higher efficiency.
Vazifeshenas. Y et al. [30]	PEMFC	- Serpentine, parallel and multichannel flow field with metal foam	1 bar/ 283 K	Numerical	- Raising metal foam porosity reduces pressure drop and the transfer of heat.
Park.J.E et al. [31]	PEMFC	- Serpentine flow field -Foam flow field (with metal foam)	1 bar/ 243.15 K	Experimental	- Foam flow field enhances electrochemical reaction of the catalyst layer and increases cell performance.
Hossain.M.S et al. [32]	PEMFC	- Parallel channel cathode flow field with metal foam.	0.5 bar (inlet)/ ~ 313.15K	Experimental	-Metal foam enhances temperature distribution and diffusion of gas to electrodes. - Water removal is observed.
Kumar. A et al. [33] [34] [35]	PEMFC	- Channel flow field with metal foam.	101.3 kPa 353 K	Numerical	-Average current density increases as permeability of metal foam decreases. - Metal foam ensures more uniform distribution of current density and better performance. - Permeability of the metal foam has a considerable impact on fuel cell efficiency.
Afshari. E et al. [36]	PEMFC	- Parallel flow field with partial restricted cathode channel and metal foam as channel.	101.3 kPa/ 353 K	Numerical	- Oxygen concentration and Current density were raised by the inclusion of baffle plate and metal foam
Toghyani. S et al. [37]	PEMFC	- Serpentine and parallel flow field with metal foam as flow distributor.	1.5 bar/ 353 K	Numerical	- A proper metal foam permeability should be chosen for optimum pressure.

Tsai. B.T et al. [38]	PEMFC	-Bipolar plate with metal foam as flow distributor.	1 bar/ 323.15 K	Experimental	-Metal foam improves the uniformity of gas reactant distribution in the catalyst layer.
Gondolini. A et al. [39]	MS-SOFC	-	~ 373.15 K	Experimental	- Use NiCrAl metal foam as metal support for SOFC application
Zeilke.P et al. [40]	SOC SOEC SOFC	-	973.15 K	Experimental	- Using CuMn foam as a cathode contact material increase the level of serial resistance during constant operation of the fuel cell.
Iwai. H et al. [41]	SOFC	- Single plate	882.15 K	Numerical	- Porous material as flow distributor ensures current collected and more uniform distribution flow.
Zhan. R et al. [11]	SOFC	- Straight channel and metal foam as cathode flow distributor.	1 bar/ 1073 K	Numerical	- metal foam as a cathode flow field distributor lead to an enhancement of the output power by 13.74% compared with conventional channel oxygen concentration, electron transport and temperature of SOFC are uniformly distributed.
Present work	SOFC	- Single channel flow field with 5 obstacles and metal foam as flow distributor.	1 bar/ 1000K	Numerical	- Placing obstacles induces velocity and pressure drop increment, and enhances mass transfer to active layers, the maximum current density increases by 6.4%. - Using a metal foam as a flow distributor provokes a uniform distribution of reactant gases, the maximum current density rises by 26%. - Adopting both metal foam and obstacles inside the channels, the SOFC achieves the best performance with a 34% improvement in the maximum current density due to uniform distribution of fuels and electrical conductivity.

4 Discussion

A comprehensive comparison of four different types of channels is performed based on the distribution of velocity field, mass fraction of reactants, pressure drop and current density of the SOFC operating at the same operating conditions.

Generally, the performance of the cell improves as more reactant gases (hydrogen and oxygen) are consumed, meaning that in areas where reactants are accessible, a higher local current density can be achieved due to increased electrochemical reactions occurring, especially in the anode reaction layer.

Placing obstacles at regular intervals in the electrode channels restrains the flow area and leads to boost the pressure of gases mainly in regions over the obstacles; consequently, the flow field is accelerated and forced to deviate the direction towards the porous electrodes, allowing higher rate and deeper penetration of species up to the reaction layers, this resulting in an increase in the level of available fuel and oxidant and in an enhancement of electrochemical reactions. Although the positive effect of using obstacles, the current density is locally improved outstandingly mostly in the regions above these obstructions (Figure 4.11 case B).

In present chapter, a metal foam that offers very unique mass transfer features is used as flow distributor as an alternative to conventional channels. The high porosity of the metal foam (≈90%) and the spatial random pore structure allows convective gas flow throughout it with low flow resistance and more uniform distribution [28].

Nevertheless, the presence of rib features and the narrow channel where the foam is placed induces an increase in the pressure drop. This aspect is crucial to assess as it determines whether the flow can provide a sufficient driving force to transport any possible condensate produced through the fluid flow structure [22].

In this porous media, the high pressure drop is attributed to the form drag, occurring due to a pressure difference across a boundary, as well as control over frictional drag in the metal foam [15,42]. So that, it presents a suitable design for enhancing mass transfer to the catalyst layer and providing better uniformity in the concentration distribution of reactant species, leading to a much higher performance of current density.

Therefore, the adoption of both metal foam and obstacles inside the channels achieves the best performance of the SOFC by maximizing the species transport towards the reaction layers and optimizing the electrochemical reaction conditions.

According to Figure 4.10 (case D), it is clear that it has the highest current density value compared with other cases. Metal foam and obstacles, which are merged and considered as a

new flow channel, lead to deliver the highest amount of fluid flow inside the electrode (Figure 4.7) and cover a wider region, due to the reduced thickness and the flow redistribution through the height of cell. In other words, this configuration induces a volume flow decrease and internal pressure increase that results in turn in a higher cell potential own to the Nernst equation. Actually, the polarization curve that illustrates the performance of the SOFC varies depending on the design of the channel flow field. The internal flow modification has a significant effect on the polarization curves principally at low operating voltages given that mass transport losses are most prevalent in the area with high current density.

5   Conclusion

In the present study, metal foam and flow channel indentation are proposed to replace the conventional straight channels for the SOFCs. A three-dimensional model of a hydrogen-fueled single SOFC has been developed to compare four different cases: the basic SOFC with simple parallel flow channels (case A), with obstacles in the flow channels (case B), with metal foam as a flow distributor (case C), and with metal foam and obstacles simultaneously (case D). Conservation equations of mass, species, momentum, energy and charge (electrons and ions) were used. The simulation involved fuel and air flow channels, electrode support, diffusion and active layers, electrolytes, and interconnects.

The model was validated over experimental data from the literature and employed to investigate the impacts of velocity, pressure and fuel mass fraction on the SOFC performance in the different cases.

The key results and conclusions can be summarized as follows:

(i)   Placing obstacles in the flow channels (case B) led to an increase in velocity and pressure drop, mainly in regions over the obstacles. This forced the reactants to flow into the electrodes, thereby enhancing and enlarging the mass fraction of reactants on the local surface where the obstacles are arranged, consequently boosting the current density.

(ii)   Compared to cases A and B, using metal foam as a flow distributor (case C) significantly improved the performance of the SOFC. Reactant gases were more uniformly distributed and transferred in the gas active layer, resulting in increased consumption of hydrogen and production of water. The maximum current density increased by 26.4% in this case.

(iii)   Adopting both metal foam and obstacles inside the channels resulted in the best performance for the SOFC, with a 34% improvement in the maximum current density. The new

flow channel design ensured uniform distribution of fuel and electrical conductivity, with a remarkable enhancement observed above the obstacles due to the combined effects of pressure drop and mass transfer in porous media.

References

[1] Zhang, X., Espinoza, M., Li, T., Andersson, M. Parametric study for electrode microstructure influence on SOFC performance. Int. J. Hydrogen Energy. 2021, 46: 37440-37459.

[2] Zhang, X., Parbey, J., Yu, G., Li, T., Andersson, M. Thermal stress analysis of solid oxide fuel cells with chromium poisoning cathodes. J Electrochem Soc 2018;165: F1224-F1231

[3] Modeling with electrochemistry. COMSOL multiphysics version 5.5, batteries and fuel cells module users guide, chapter 2: modeling with electrochemistry, Stockholm, Sweden. 2019

[4] Patcharavorachot, Y., Arpornwichanop, A., Chuachuensuk, A. Electrochemical study of a planar solid oxide fuel cell: role of support structures. J Power Sources. 2008; 177: 254-261.

[5] Andersson, M. SOFC Modeling Considering Mass and Heat Transfer, Fluid Flow with Internal Reforming Reactions, Licentiate Thesis, Lund University, Sweden, 2009

[6] Ferrero, D., Lanzini, A., Santarelli, M. Solid Oxide Fuel Cells Modeling. In: Boaro, M., Salvatore, A. (eds) Advances in Medium and High Temperature Solid Oxide Fuel Cell Technology. CISM International Centre for Mechanical Sciences, vol 574. Springer, Cham. 2017; 574: 291–342

[7] Andersson, M., Yuan, J., Sundén, B. SOFC modeling considering electrochemical reactions at the active three phase boundaries. Int J Heat Mass Transf. 2012; 55: 773-788.

[8] Shi, J., Xue, X. CFD analysis of a novel symmetrical planar SOFC design with micro-flow channels. J Chem Eng. 2010; 163: 119-125.

[9] Akkaya, A. V. Electrochemical model for performance analysis of a tubular SOFC. Int J Energy Res 2007; 31: 79-98

[10] Andersson, M, Yuan, J., Sunden, B. SOFC modeling considering hydrogen and carbon monoxide as electrochemical reactants. J Power Sources 2013; 232: 42-54

[11] Zhan, R., Wang, Y., Ni, M., Zhang, G., Du, Q., & Jiao, K. Three-dimensional simulation of solid oxide fuel cell with metal foam as cathode flow distributor. 2020. Int J Hydrogen Energy, 45(11), 6897-6911.

[12] Fu, Q., Li, Z., Wei, W., Liu, F., Xu, X., Liu, Z. Performance of a beam and slot interconnector for anode-supported SOFC stack. Energy Convers Manag 2021; 241:114277

[13] Wan, Z., Quan, W., Yang, C., Yan, H., Chen, X., Huang, T., & Chan, S. Optimal design of a novel M-like channel in bipolar plates of proton exchange membrane fuel cell based on minimum entropy generation. Energy conversion and management, 2020; 205, 112386.

[14] Lv, C., Li, W., Du, J., Liang, J., Yang, H., Zhu, Y., & Ma, B. Experimental investigation of permeability and Darcy-Forchheimer flow transition in metal foam with high pore density. Experimental Thermal and Fluid Science, 2024; 154, 111149.

[15] Du Plessis, P., Montillet, A., Comiti, J., & Legrand, J. Pressure drop prediction for flow through high porosity metallic foams. Chemical Engineering Science,1994; 49(21), 3545-3553.

[16] Danilov, V. A., Tade, M. O. A CFD-based model of a planar SOFC for anode flow field design. Int J Hydrogen Energy 2009;34(21):8998e9006

[17] Moreno-Blanco, J., Elizalde-Blancas, F., Riesco-Avila, J. M., Belman-Flores, J. M., & Gallegos-Muñoz, A. (2019). On the effect of gas channels-electrode interface area on SOFCs performance. Int J Hydrogen Energy, 2019; 44(1), 446-456.

[18] Manglik, R. M., & Magar, Y. N. Heat and mass transfer in planar anode-supported solid oxide fuel cells: effects of interconnect fuel/oxidant channel flow cross section. J. Thermal Sci. Eng. Appl. ,2015; 7(4), 041003.

[19] Heidary, H., Kermani, M. J, Dabir, B. Influences of bipolar plate channel blockages on PEM fuel cell performances. Energy Convers. Manage. 2016; 124:51–60

[20] Kuo, J. K., Yen, T. H., Chen, C. K. Three-dimensional numerical analysis of PEM fuel cells with straight and wave-like gas flow fields channels. J. Power Sources 2008;177 (1):96–103.

[21] Tiss, F., Chouikh, R., Guizani, A. A numerical investigation of reactant transport in a PEM fuel cell with partially blocked gas channels. Energy Convers. Manage. 2014; 80:32–8.

[22] Chellehbari, Y. M., Adavi, K., Amin, J. S., & Zendehboudi, S. A numerical simulation to effectively assess impacts of flow channels characteristics on solid oxide fuel cell performance. Energy Convers. Manage. 2021,244, 114280.

[23] Bilgili, M., Bosomoiu, M., & Tsotridis, G. Gas flow field with obstacles for PEM fuel cells at different operating conditions. Int J Hydrogen Energy, 2015, 40(5), 2303-2311.

[24] Dehsara, M., & Kermani, M. J. Proton exchange membrane fuel cells performance enhancement using bipolar channel indentation. J. Mech. Sci. Technol 28 (1) (2014) 365~376

[25] Cai, G., Liang, Y., Liu, Z., & Liu, W. Design and optimization of bio-inspired wave-like channel for a PEM fuel cell applying genetic algorithm. Energy,2020; 192, 116670.

[26] Ghanbarian, A., Kermani, M. J. Enhancement of PEM fuel cell performance by flow channel indentation. Energy Convers. Manage. 110 (2016) 356–366

[27] Perng, S. W., Wu, H. W., Chen, Y. B., & Zeng, Y. K. Performance enhancement of a high temperature proton exchange membrane fuel cell by bottomed-baffles in bipolar-plate channels. Applied Energy, 2019. 255, 113815.

[28] Tseng, C. J., Tsai, B. T., Liu, Z. S., Cheng, T. C., Chang, W. C., & Lo, S. K. A PEM fuel cell with metal foam as flow distributor. Energy Convers. Manage, 2012. 62, 14-21.

[29] Afshari, E., & Houreh, N. B. Performance analysis of a membrane humidifier containing porous metal foam as flow distributor in a PEM fuel cell system. Energy Convers. Manage.,2014. 88, 612-621.

[30] Vazifeshenas, Y., Sedighi, K., & Shakeri, M. Heat transfer in PEM cooling flow field with high porosity metal foam insert. Applied Thermal Engineering, 2019. 147, 81-89.

[31] Park, J. E., Hwang, W., Lim, M. S., Kim, S., Ahn, C. Y., Kim, O. H., ... & Sung, Y. E. Achieving breakthrough performance caused by optimized metal foam flow field in fuel cells. Int J Hydrogen Energy, 2019. 44(39), 22074-22084.

[32] Hossain, M. S., & Shabani, B. Reticulated porous and parallel channel cathode flow fields in real scale polymer electrolyte membrane fuel cells: A comparative experimental study. Int J Hydrogen Energy, 2019. 44(47), 25905-25917.

[33] Kumar, A., Reddy, R. G. Modeling of polymer electrolyte membrane fuel cell with metal foam in the flow-field of the bipolar/end plates. J Power Sources 2003 ;114(1) : 54e62.

[34] Kumar, A., Reddy RG. Materials and design development for bipolar/end plates in fuel cells. J Power Sources 2004;129(1):62e7.

[35] Kumar A, Reddy, R. G. Polymer electrolyte membrane fuel cell with metal foam in the gas flow-field of bipolar/end plates. J New Mater Electrochem Syst 2003;6(4):231e6

[36] Afshari, E., Mosharaf-Dehkordi, M., Rajabian, H. An investigation of the PEM fuel cells performance with partially restricted cathode flow channels and metal foam as a flow distributor. Energy 2017;118: 705e15.

[37] Toghyani, S., Afshari, E., & Baniasadi, E. Metal foams as flow distributors in comparison with serpentine and parallel flow fields in proton exchange membrane electrolyzer cells. Electrochimica acta, 2018; 290, 506-519.

[38] Tsai, B. T., Tseng, C. J., Liu, Z. S., Wang, C. H., Lee, C. I., Yang, C. C., & Lo, S. K . Effects of flow field design on the performance of a PEM fuel cell with metal foam as the flow distributor. Int J Hydrogen Energy 2012;37(17):13060e6.

[39] Gondolini, A., Mercadelli, E., Sangiorgi, A., & Sanson, A. Integration of Ni-GDC layer on a NiCrAl metal foam for SOFC application. J. Eur. Ceram. 2017 37(3), 1023-1030.

[40] Zielke, P., Wulff, A. C., Sun, X., Jensen, S. H., Kiebach, R., Frandsen, H. L., & Hagen, A. Investigation of a spinelforming Cu-Mn foam as an oxygen electrode contact material in a solid oxide cell single repeating unit. Fuel Cells 2017;17(5)

[41] Iwai, H., Yamamoto, Y., Saito, M., & Yoshida, H. Numerical simulation of intermediate-temperature direct-internal-reforming planar solid oxide fuel cell. Energy 2011;36(4):2225e34.

[11] Zhan, R., Wang, Y., Ni, M., Zhang, G., Du, Q., & Jiao, K. Three-dimensional simulation of solid oxide fuel cell with metal foam as cathode flow distributor. 2020. Int J Hydrogen Energy, 45(11), 6897-6911.

[42] Dukhan, N. Correlations for the pressure drop for flow through metal foam. Experiments in fluids,2006; 41, 665-672.

General conclusions

Solid oxide fuel cells are in commercialization and innovation process. It is necessary to further minimize the manufacturing cost, which can be accomplished through proven reliability and enhanced performance. This thesis aims to improve the performance of a numerical model of SOFC by providing a deeper comprehension of its physical, chemical, and electrochemical mechanisms.

This was achieved by creating a three-dimensional model of a single cell anode supported SOFC using COMSOL Multiphysics. Conservation equations of mass, species, momentum, energy and charge (electrons and ions) are solved simultaneously, by applying computational fluid dynamics (CFD) methods with the finite element model. The simulation involved fuel and air flow channels, electrode support layers, diffusion and active layers, electrolytes and interconnects. The model has been validated over experimental data from the literature, it is suited for conducting many parametric studies at different design and operating conditions.

The first section of the findings detailed in this thesis suggests a potential modification to the geometry to enhance the exploitation of the fuel. Metal foam and flow channel indentation are suggested to replace the traditional straight channels at the SOFC. A 3D SOFC has been developed to compare four distinct cases: the standard SOFC with straight parallel flow channels, the SOFC with five obstacles in the flow channels, the SOFC with metal foam performing as a flow distributor, and the SOFC with both obstacles and metal foam simultaneously installed in order to study their impacts of velocity, pressure and fuel mass fraction on the SOFC performance. The main results obtained are as follows:

* By adding obstacles to the flow channels, the reactants were forced to flow into the electrodes, increasing the mass fraction of reactants in the area where the obstacles are placed and enhancing the current density. The obstacles caused a velocity and pressure drop, which boosted mainly in the regions over them.

* Applying metal foam as a flow distributor results in a 24% increase in current density, the reactant gases are transferred and dispersed more uniformly in the gas active layer, enhancing the amount of water produced and hydrogen consumed.

* Adopting both metal foam and obstacles inside the channels, the SOFC attains optimal performance with a 34% increase in current density. Given the combined effects of mass transfer and pressure drop in porous media and blocked gas channels, the new flow channel

design guarantees uniform distribution of fuels and electrical conductivity with a remarkable movement above the obstacles.

In the second section, and based on the micro-modelling consideration, the model has been employed to study the impact on SOFC performance of the micro-structural properties such as the permeability and volume fractions of ionic and electronic conductors in the electrodes. It is found that:

* Reducing permeability in porous media until a certain point balances species diffusion and increases the pressure, thus improves the current density. The operation of the SOFC is more affected by changes in permeability in the support and diffusion layers than in the active layer.

* The current density increases as the electronic and ionic phase volume fractions in the active, support, and diffusion layers rise.

* Given that the ionic phase has a greater influence than the electronic phase, the effect of the change in permeability on the current density is more significant as a function of the ionic phase's volume fraction.

Future work

Based on the findings of this study and in order to enhance the model's reliability, future research should consider conducting a more thorough parametric investigation to identify more optimal designs. Several suggestions for further investigation are proposed:

* Steady state models for hybrid, non-isothermal, and isothermal models ought to be expanded to dynamic simulations. Therefore, time-dependent behaviors of the cells, including startup and control processes, can be predicted.

* The present single cell model can be expanded to a multiscale model of a SOFC stack.

* One benefit of solid-oxide fuel cells is that they may be fed carbon-based fuels, including hydrocarbons such as methane, carbon monoxide and carbon dioxide, further research on more sophisticated fuel mixtures, like biogas and natural gas, as well as hydrocarbons with longer coal chains, would be fascinating.

* Internal reforming can be integrated in the cell stacks due to the high operating temperature, and certain hydrocarbons can be directly consumed as fuel. This will impact the SOFCs' features, particularly in the temperature fields.

* A modification in the design can be beneficial improve the system's efficiency.